A Single-Element Fiber Transducer for All-Optical Ultrasound and Photoacoustic Sensing

A Thesis
SUBMITTED TO THE FACULTY OF THE UNIVERSITY OF MINNESOTA BY

Supriya V. Thathachary

IN PARTIAL FULFILLMENT OF THE REQUIREMENTS FOR THE DEGREE
OF DOCTOR OF PHILOSOPHY

Adviser: Shai Ashkenazi

December 2019

Acknowledgments

This thesis would not have been possible without the advice, help and support of several people. My heartfelt gratitude goes to all of them. I am truly privileged to have had Dr. Shai Ashkenazi as my thesis adviser. He has been extremely supportive and patient at every stage in this journey, encouraging me to learn and grow in every way without once letting me feel pressured by his expectations. He provided me with the right balance of freedom and insight, and I have learned many lessons from him that I will gratefully retain throughout life. His scientific curiosity, kindness, and humor are truly inspirational. I cherish the time spent under his advisement, and in the company of both him and his wife Dr. Rina Ashkenazi, whose kind advice and cheerful encouragement have also always lifted my spirits.

I also thank Dr. Taner Akkin, Dr. James Leger, Dr. Emad Ebbini, Dr. Robert Wilson and Dr. Alex Opitz for their time reviewing my work, and their insightful questions and suggestions. I also thank Dr. Nicholas Burke, Dr. Patrick Nachman and Dr. Michael Mauer for providing clinical insights to drive this project in the right direction.

My labmates through the years have been extremely supportive. I thank Mohammed Amin Tadayon and Clay Sheaff for training me when I first started, and for all their advice on the project I inherited from them. I owe Ekaterina Morgounova Ippolito more than I can possibly describe for her steadfast friendship, encouragement, advice, and empathy in all matters related to work and life. I thank Joshua Punnoose for his cheerful friendship and for the many engaging discussions we have had. I'm also extremely grateful to the undergrads I have mentored, Julia Howes, Cameron Motameni and Asif Ashraful, for all their hard work.

I thank Glenn Kuschke, Kevin Roberts, Lage von Dissen, Paul Kimani and Laura Parmeter of the Minnesota Nano Center, and Ron Bystrom and his staff of the CSE workshop for always being so enthusiastic and approachable in helping me develop

reliable processes around rather unconventional substrates.

I deeply appreciate Zaw Win, Pantea Moghimi, David Zhang, Vahhab Zarei, Rohit Dhume, Ghaidan Shamsan, Steven Lee, Anh La, Shannen Kizilsky, Vasanth Ravikumar and Tianqi Li and for their warm friendship and all the help they have given me over the years. Many thanks also to the Barocas Lab for the daily lunchtime crosswords that always brightened my day, to Anand Kartha, Maya Raghunandan, Sandhya Koteshwara, Ravindra Khedkar, Kanchan Kulkarni, Raghu Venkataraman, and Mridul Yadav for being such encouraging friends and wonderful neighbors, and to my old friends, especially Savitha Srinivasan, Sindhu Devendar, Nikita Gurudath, Biswarup Mukherjee and Anand Chandrasekhar for consistently putting in the effort to reach out despite being on difficult journeys of their own.

The example and encouragement of several teachers in my early life, most notably Ms. Visalakshi N Rao, Mr. Chandran Kasu, Dr. Suguna M. Rao and Dr. Premila Manohar, have been crucial to my academic growth. I express my humble and heartfelt gratitude to them all.

My family has been an unwavering source of strength and support. I thank my aunts, uncles and cousins for all their love and encouragement. I am forever indebted to my parents for the values they imparted, for their extraordinary efforts to give me a wonderfully happy childhood, and for being the best examples of cheerful resilience in the face of adversity. I am so grateful for the strength and sense of purpose I find every day in the memory of my father, Prof. V.T Ranganathan, whose wisdom and quiet humour continue to give me clarity when I most need it. I thank my brother, Arun, for being simultaneously my favorite teacher, most honest critic and most protective friend. Finally, I thank my mother Sowmithri for her limitless love and tireless efforts to care for me, and for always being patient with me. I owe all my achievements to their silent sacrifices. Words cannot describe the love and gratitude I have for them all.

Abstract

The past few decades have seen a rapid rise in minimally invasive medical procedures performed around the globe. These procedures have been made possible largely because of innovations in medical imaging and sensing to guide physicians in performing the interventions safely. Ultrasound technology has remained highly popular through this transition due to its safety and efficacy. However, the demand for miniature flexible devices for increased accessibility has prompted a shift toward all-optical ultrasound devices. Additionally, photoacoustic imaging and sensing have emerged as a promising technology with abilities to enhance diagnostic capabilities in several clinical applications, most significantly in the imaging of atherosclerotic plaque.

The Fabry-perot ultrasound detector, being one of the more widespread optical ultrasound detection technologies, has been explored significantly in this context. This thesis presents a novel wave-guided configuration for fiber Fabry-Perot ultrasound detectors. This work demonstrates 16 times higher sensitivity than traditional piezolelectric technology at comparable size scales. The chapters that follow present the simulations and experiments conducted around (a) optimizing the fabrication of the wave-guided fiber Fabry-Perot devices, (b) the complete optical and acoustic characterization of the fabricated devices, and (c) the potential improvements that can be made with incorporating dielectric mirrors. The thesis concludes with a discussion on the possible configurations for creating a complete ultrasound and photoacoustic probe for guiding minimally invasive interventions.

Contents

List of Tables

List of Figures

Chapter 1

Introduction

Over the past few decades, health care has seen a paradigm shift toward minimally invasive procedures, data-driven decisions and personalized medicine. This shift has been made possible because of several crucial innovations which assist physicians in gathering information about the anatomy at the region of interest, and tools which help them perform interventions in precise and predictable ways. Several imaging and sensing tools have evolved as a result of these efforts. In cardiology, it has now become standard practice to use catheter based sensing tools to gauge the condition of a lesion, and to use intravascular imaging to study the health of the vessel wall. This thesis presents the work done towards filling a gap in the set of tools available to navigate vascular occlusions. The device developed in this work is a fiber optic tool to navigate complex vasculature by relying on a photoacoustic signal from the tissue encountered by the device. Although developed to fill a need in cardiology, this tool can be applied in any catheter/needle-based intervention in order to characterize tissue, and is thus open to a wide range of applications. The following sections and chapters elaborate on the state of the art in ultrasound technology, and present, in this context, our concept solution: A single element, forward-viewing transducer for all-optical ultrasound and photoacoustic sensing.

1.1 Intravascular Ultrasound (IVUS)

Intravascular imaging refers to the technique of introducing a catheter-based probe into a blood vessel to visualize the region of clinical interest. Early evidence of the use of high-frequency IVUS to image peripheral and coronary arteries appeared in the 1980s [1]. Reports showing the correlation between histologic characteristics of a vessel wall and the corresponding high frequency (40MHz) ultrasonic images established the potential of the system for diagnostic imaging [2]. Advancements in the development of such catheters (using various imaging modalities) have been driven by the increasing understanding among physicians that detailed and reliable information on the structure and composition of atherosclerotic lesions will help improve safety and efficacy of the interventional techniques employed to address them. IVUS has since been used in standard practice to evaluate atherosclerotic leasions. It has been used to estimate percentage of arterial cross-sectional stenosis[3], lumen size and wall morphology [4], to estimate flow [5], and plaque morphology [6][7], thus emerging as the gold standard in vascular imaging [8].

Increasingly, interventional techniques such as balloon angioplasty and mechanical atherectomy are being utilized to address vascular occlusions, and the risks of perforation and dissection associated with these techniques further emphasize the need for reliable imaging techniques. Intravascular imaging can provide valuable information regarding the size and shape of the lumen at the site of the lesion, as well as, in some cases, the composition of the plaque(fatty, calcific or fibrous)[9]. This information can assist physicians in choosing the correct tool for atherectomy or the appropriate stent size, and also help in the assessment of treatment progression and the risk of restenosis. Most importantly, IVUS has been explored as a way to guide and reduce risk of adverse events during the course of intervention such as perforation and detection of the arterial wall[10] [11] [12]. Current-day interventional cardiology is thus heavily dependent on the availability of good intravascular imaging and sensing catheters.

1.1.1 IVUS Technology

Over the years, a variety of devices have been developed and explored for intravascular ultrasound imaging. These include single-element mechanical intravascular ultrasound devices with rotating transducers, muti-element phased array systems, forward looking Capacitive Micromachined Ultrasound Transducers (CMUTs), and several others [13]. This section presents an overview of the most commonly used configurations with their advantages and limitations.

Rotating Single-element Transducers

A mechanical IVUS device consists of a single piezoelectric element located at the tip of a flexible drive cable housed in a protective sheath[14] [15]. The drive cable rotates the transducer about its axis, to form a cross-sectional image. This transducer can also be moved longitudinally within its sheath during rotation, enabling side-view imaging along with longitudinal pull-back. Therefore, it is possible to create a 2D image of a section of the vessel wall to assess the distribution of plaque. This technology is available commercially and has been used extensively in the clinic for the study of atherosclerotic plaque and to guide interventions[16] [17] [18].

An advantage of the mechanical IVUS system is that they typically have a large element size as compared to the elements on a array. Larger element sizes offer higher signal to noise ratios, thus achieving better resolution. A significant disadvantage, though, is that these systems can often suffer from uneven rotations due to the stress accumulated in the catheter from tortuosity. This can lead to image distortions called Nonuniform Rotational Distortions (NURD). Some efforts have been made to overcome NURD by using elecromagnetic [19] or ultrasonic[20] micromotors but are yet to be transferred to commercial catheters.

Phased Arrays

In addition to distortion, mechanically scanned transducers also imply fabrication challenges and bulky devices that are not flexible. An approach to overcome this is the use of phased array transducers. These devices use multiple (typically 64) elements arranged around the circumference of a catheter which fire sequentially to produce a beam. Such cylindrical phased arrays provide an alternative to radial scanning, eliminating the need for rotational mechanism and providing more uniform resolution through dynamic focusing. [21] The Volcano Eagle Eye is a widely used commercial system that employs this configuration[22].

Forward-looking CMUT

While side-view IVUS has its uses, there is also a need for forward-viewing devices in cases where penetration of occlusions is difficult/inadvisable. Of the developments made to address this need, the most promising approach is the Capacitive Micromachined Ultrasound Transducers(CMUT). These devices have two concentric arrays of capacitive elements for transmitting and receiving respectively[23]. Each element is an air-filled capacitor formed using one fixed and one flexible electrode, which deflects upon excitation. They are easy to fabricate using standard lithographic techniques and provide wide bandwidths and high sensitivity [24]. This technology is now being integrated onto catheters for imaging [25], however it is yet to gain widespread clinical adoption. An alternative configuration is of linear arrays making use of the face of the catheter [26]. However, these devices are frequency limited due to the small element size required to fit on the face of the catheter. Additionally, their relatively large sizes make both these configurations unsuitable for use in coronary arteries where their use would be most beneficial.

1.2 Intravascular Photoacoustic (IVPA) Imaging

IVPA is an emerging technique that has the potential to be applied toward gathering morphological information about plaque. This technique relies on the optical absorption of tissue to generate acoustic waves. Early evidence of the utility of IVPA emerged in 2006[27]. This study on tissue mimicking phantoms indicated that IVPA could be useful in detecting structure and composition of atherosclerotic plaque.

Subsequently several studies from Emilianov et al. explored this idea further. In a study in 2008, this group performed ex-vivo IVPA studies on healthy and atherosclerotic rabbit aortas. To assess plaque composition, multi-wavelength (680-950 nm) spectroscopic IVPA imaging studies were carried out to assess plaque composition. They showed that combined IVUS and IVPA imaging could be useful in plaque characterization[28]. In 2009, Beard et al. demonstrated that spectroscopic PA could be used to differentiate arterial tissue and lipid rich plaque using the wavelength range 740-1800 nm[29]. However, they acknowledge the need for a good intravascular probe to be able to facilitate discrimination of a wider range of tissue types such as calcified and fibrous tissues. The same group later extended this work by studying post mortem human aortas at NIR wavelengths, and obtaining images through blood, demonstrating that lipid rich atheromatous plaques could be identified using spectroscopic photoacoustic imaging[30]. Over the next decade, several other works have demonstrated the efficacy of PA imaging, and multimodal imaging techniques including PA, in identifying vulnerable arterial plaque [31] [32] [33][34].

In terms of the instrumentation required to advance this technique, these studies almost unanimously indicate the need to shift towards all-optical detection. The following section explains why all-optical probes would be most suitable.

1.2.1 Photoacoustic Detection

The detection of photoacoustic signals has a different set of requirements than the detection of conventional ultrasound signals [35].

1. The magnitude of PA signals are generally in kPa, having been generated from within the illuminated tissue. This is generally about 3 orders of magnitude less than signals typically generated in ultrasound imaging. This implies the need for very high sensitivity detection.
2. Photoacoustic signals span a much wider bandwidth (sub-MHz to hundreds of MHz) as compared to the relatively narrowband ultrasound signals (generally in the low MHz, spanning under 50% of the center frequency)
3. Collection of data over wider acceptance angles is usually required in photoacoustic imaging to improve image quality and reduce artifacts.
4. While ultrasonography provides greater penetration depth, photoacoustics has a significant advantage of inherent contrast due to the differences in tissue absorption. This also implies the potential impact of photoacoustics in interventional imaging/sensing applications.

Thus the size of the photoacoustic transducer must be small, and the construction suitable for integration into endoscopic/catheter-based devices. Piezoelectric transducers developed for conventional ultrasonography are therefore, not ideally suited for photoacoustic detection. Thus there has been a shift toward the use of all-optical transducers, which offer a higher signal-to-noise ratio per unit area as compared to piezoelectric transducers. Additionally, they are resistant to electromagnetic noise and offer wider detection bandwidths, which is desirable for photoacoustic signals. The next section explores all the different optical detection mechanisms that have been developed and discusses their use in photoacoustic detection.

1.3 Optical Ultrasound Detection

Optical methods of ultrasound detection may be broadly divided into refractometric and interferometric methods. Refractometric detection relies on the fact that acoustic waves incident on a medium induce mechanical stress in it, consequently changing the refractive index. These changes are then detected at an interface between two adjacent media by using an interrogating laser beam. Changes in intensity, deflection angle or phase of the beam are recorded by an optical detector, and represent the acoustic perturbations. Interferometric methods, on the other hand, detect changes in interference patters induced by ultrasound. This could be due to vibrations of a reflector or by altering the resonance frequency of the resonator. Below, the three most widespread optical ultrasound detection methods are explained, along with the merits and challenges of all-optical ultrasound detection.

1.3.1 Merits

There are several advantages to optical ultrasound detection over conventional piezoelectric detection. Optical detectors can be constructed on optical fibers, usually under 200 μm in diameter. This small size allows a lot of flexibility in the application. Moreover, optical detectors offer much higher sensitivities at these sizes than piezoelectrics can. There is no electrical cross talk or interference, which is often the case with electrical wiring for small elements. Perhaps most significantly, optical detection can be seamlessly combined with either optically generated ultrasound excitation or direct illumination for photoacoustic excitation. Thus, it is possible to create a complete probe on a single fiber. Details of possible transducer configurations to achieve this are presented in chapter 5. As discussed, combined ultrasound and photoacoustic imaging and sensing offer several diagnostic advantages over the individual modalities, which makes it all the more appealing to pursue optical ultrasound detectors.

1.3.2 Optical Ultrasound Technology

Microring Resonators

Polymer microring resonators are closed-loop waveguide structures (ring resonators) along a straight waveguide such that light couples in and out of the resonator. The coupling is confined to the small region where the light distributions overlap. When an ultrasound wave is incident, on the structure, it applies stress deforming both the ring waveguide and the coupling region, which in turn causes a change in the effective refractive index. This translates to a wavelength shift in the resonance of the structure. By choosing a wavelength of transmitted light which is on the steep edge of the transmission spectrum, a modulated output corresponding to the acoustic wave can be obtained. Thus, ultrasound detection with very high sensitivity can be performed using such structures[36].

The fabrication of such sensors using a simple mechanical imprinting process has been shown to repeatably produce high quality resonators [37] [38] [39]. Apart from being reproducible, this type of detector has several advantages such as high acoustic sensitivity (NEP as low as 10 Pa over 350 MHz), ultra-broad bandwidth(from DC to upto 350 MHz at -3dB), wide angular response(-6 dB beam width over 40 degree for rings of 40 μm diameter) and compact size [40]. All of these features are particularly helpful to perform photoacoustic sensing and imaging.

There have also been efforts to develop integrated US/PA all-optical scanheads[41]. The symmetrical, disc shaped geometry with diameters of around 100 μm makes these micro-resonators ideal for optoacoustic tomography, however they typically provide broad detection bandwidth only at narrow opening angles, which is less than ideal. Although it has been investigated for applications in microscopy and tomography, this technology has not been explored in the context of catheter based devices for minimally invasive procedure guidance.

Fiber Bragg Gratings(FBG)

Another all-optical ultrasound sensing system is the Fiber Bragg Grating or FBG. This is a type of sensor in which a distributed reflector is constructed within a segment of an optical fiber. By creating a periodic variation in the refractive index of the fiber core, some wavelegths are reflected while transmitting others. It can therefore be used as a filter or a wavelength specific reflector[42][43]. Recently, a special type of FBG has attracted attention for its ultrasound-sensing capabilities[44]. The π-phase shifted FBG, so called because of the π-phase discontinuity in the center of the grating, is made by introducing a π phase shift into the refractive index modulation of the FBG during its fabrication. Because of this, the spectral transmission has a narrow bandpass resonance within the middle of the reflection lobe. Thus, it can be described as a resonator cavity formed by two FBG mirrors which can be exploited for high-sensitivity ultrasound detection. The higher the reflectivity of the two mirrors, higher the quality of the resultant resonator.

π-FBG based sensing systems have been demonstrated as part of optoacoustic and endoscopic microscopy systems. They can provide sensitivities of 100 Pa and bandwidths upto 77 MHz[45][46]. They feature 1-D cavities on a size scale on the order of 100 μm. Therefore, they are treated as line detectors. Although they can be used for optoacoustic tomography, they provide lower resolution than point detectors. The most ideal configuration is to create miniaturized π-FBGs in optical waveguides which an generate higher refractive index contrast than optical fibers.

Fabry-Perot Resonators

A Fabry–Pérot interferometer/resonator is a cavity comprising two mirrors with a optical medium in between. Light incident into the cavity through one of the mirrors is reflected multiple times between the two mirrors, exhibiting a periodic resonance. By tuning the wavelength of light to a point on the transfer function corresponding to high slope, the movement of the spectrum (cause by perturbations such as acoustic waves) can be tracked with high sensitivities. Thus, by exploiting the sharp resonances, this device can be used as an all-optical ultrasound sensor. The detailed operation and metrics used to assess performance are presented in the next chapter.

Fabry-Perot resonators can be constructed either as free-space coupled devices or fiber coupled devices. This thesis concentrates on fiber Fabry-Perot cavities. These can broadly be classified into intrinsic and extrinsic cavities[47]. Intrinsic cavities have reflecting components within the fiber itself. This can be achieved by techniques such as micromachining[48][49] or chemical etching [50]. They are difficult to fabricate, and hence, expensive to produce. Extrinsic cavities on the other hand are those that rely on external structures[51]. They can utilize highly reflective mirrors[52], thus reaching very high finesse(see Chapter 2). They are simpler to fabricate than intrinsic cavities, but often suffer coupling losses, and require careful packaging[53].

Perhaps the most significant work in this direction has been by Beard et al. They demonstrate a plano-concave polymer resonator cavity deposited on the tip of a single mode optical fiber. The shape of the concave mirror is used to approximately match the shape of the emerging wavefront front, thus effectively recoupling light back into the fiber and achieving impressive sensitivities (acoustic response up to 40 MHz and noise-equivalent pressures as low as 1.6 mPa per $\sqrt{Hz}$)[54]. This work explores an alternate approach to fiber Fabry-Perot resonators, by including a waveguide in a flat cavity for light confinement.

1.3.3 Challenges

Although these are several advantages of using all-optical ultrasound detection, there are also some significant challenges to be addressed. Arrays are well supported by piezoelectric devices, whereas optical fiber transducers each serve as only a single element. In order to be able to do imaging, multiple fibers would need to be bundled together, or a single element will have to be mechanically scanned. Either of these cases implies the need for a space significantly larger than the fiber diameter, thus losing the advantage of the small size and accessibility. Additionally, for applications that could still benefit from the higher sensitivity offered by optical technologies, and where size isn't a major constraint (such as non-invasive PAI), there is still a need to connect each fiber in the bundle to an optical source. Applications requiring simultaneous use of all the fiber elements (such as flow imaging or any other dynamic measurement) might also require tuning these individual sources to exactly the same wavelength. While optical multiplexing can address some of these issues, it is still a significant limitation.

Therefore, the question arises about where single-element ultrasound detection technology can still be utilized. Given the tissue-discriminating ability of photoacoustics resulting from the inherent contrast due to the preferential absorption of different optical wavelengths by different tissue absorbers, several use-cases are envisaged. Some of these are presented in the next section.

1.4 Clinical Applications

1.4.1 Chronic Total Occlusions(CTO)

A chronic total occlusion is defined as a greater than 3- month- old, total obstruction of a coronary artery [55]. CTOs constitute a significant healthcare burden; literature shows that CTOs are identified in up to one third of patients referred for coronary angiography [56], yet CTO PCI is underutilized due to suboptimal success rates and procedural complexity. Intravascular guidance to aid CTO recanalization can significantly reduce risks of arterial dissection and perforation [57]. Several devices have been developed to address this issue [58], however there is still a need for further technical development to facilitate and simplify revascularization techniques. This presents an opportunity for the use of the proposed device: to significantly shorten procedure time and to reduce risk of dissection and perforation to improve the safety, standardization, and predictability of CTO recanalization [55]. Described in greater detail in chapters 5 and 6, the proposed device uses a sensing guidewire to identify the luminal borders and alert the physician when the arterial wall is approached. It would allow the physician to move quickly and safely through the occlusion without dissecting or perforating the artery wall, thus reducing procedure time, and consequently cost.

Often, since the risk of direct CTO crossing is very high, physicians employ the dissection-reentry method. This procedures involve arterial wall dissection to move the guidewire across the occluded portion of a vessel within the subintimal space. On the far end, the guidewire is pushed back into the true lumen. Several approaches have been developed to direct the guidewire back in the artery at a point distal to the occlusion. This technique requires substantially longer time to complete in comparison to crossing the CTO through the true lumen. additionally, the dissection-re-entry strategy results in higher rates of restenosis which is treated with a second PCI procedure [59]. Having a reliable signal from the device to tell the physician when it is safe to continue pushing the guidewire, and when it is critical to pull back and redirect the guidewire will help the physicians cross the occlusion safely using just the true lumen. This will also enable standardization of the procedure, enabling consensus among physicians and, consequently, wider availability of the procedure across hospitals.

1.4.2 Other Applications

Outside of cardiology applications, this technology could potentially be used in any minimally invasive procedure where tissue differentiation is required. This could include monitoring laser ablation of tissue as is performed in the treatment of certain types of cancer [60][61], or improving the yield of and reducing complications arising from biopsies by identifying the correct samples based on their photoacoustic signature. Further exploration of the optical properties of these tissue types is required to confirm the applicability of this technology in these areas.

1.5 Organization of Thesis

This thesis is organized into the following chapters: Chapter 2 presents the fundamentals of Fabry-Perot resonators, and describes the various metrics used to evaluate their performance. Chapter 3 lays out the simulation studies performed to guide the fabrication of the fiber-Fabry-Perot sensor. Chapter 4 presents the experiments done around identifying a method to create waveguiding pillars within the resonator, and the performance of the first iteration of the devices. This chapter also describes the effect of temperature on the stability of the characteristic spectra of the device. Chapter 5 then presents the fabrication and complete optical and acoustic characterization of the device. The final chapter describes studies to be conducted to demonstrate the capability of the device to perform photoacoustic sensing, and lays out the scope for future work.

Chapter 2

Fabry-Perot Interferometers for Ultrasound detection

As described in the introduction, the Fabry-Perot Interferometer has been explored for the detection of ultrasound waves. This chapter explains the mechanism of action, defines the various performance metrics used to evaluate FP ultrasound detectors, and highlights the main mechanisms of loss within such a FP cavity.

2.1 Working Principle

A Fabry–Pérot interferometer consists of a resonating cavity formed between two mirrors and an optically transparent medium between them, as shown in (Figure 2.1). Part of the light incident on the mirror gets reflected repeatedly between the two mirrors, thus forming a resonator. The Fabry-Perot ultrasound detector is constructed by depositing two mirrors on the tip of an optical fiber, with a waveguided polymer layer in between. This resonator has a certain interferometer transfer function (ITF) with resonances at all wavelengths of interrogation laser light such that the integral multiple of the effective half-wavelength is equal to the device thickness. When an acoustic wave is incident on this resonator, the thickness of the resonator,

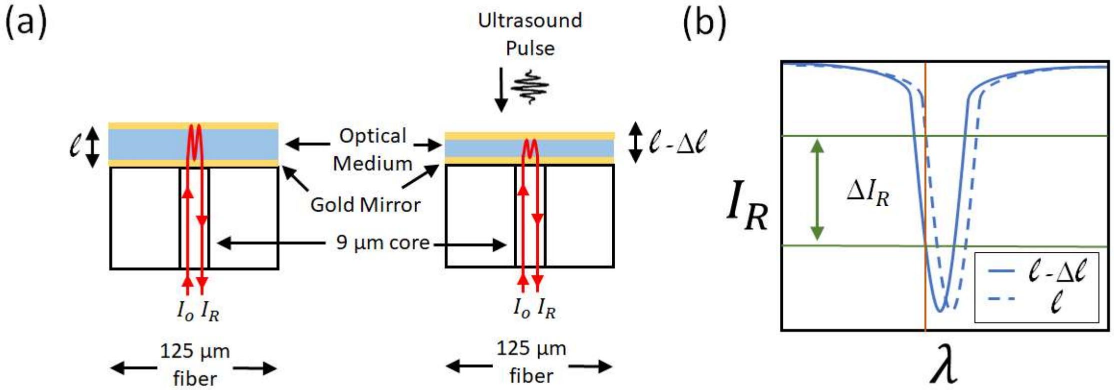

Figure 2.1: Fabry–Pérot ultrasound detector: (a) structure of the device showing NIR wavelength interrogation and (b) shift in resonance upon ultrasound detection.

and therefore, its interferometer transfer function, changes.

To operate the device as an ultrasound detector, the interrogation laser is tuned to a wavelength corresponding to the maximum slope of the ITF. When the acoustic pulse hits the resonator, the ITF shifts, causing either increased or decreased reflection at the tuned wavelength depending on the polarity of the acoustic pulse. Thus, over the duration of the pulse, the reflected light from the resonator fluctuates in a manner corresponding to the acoustic pulse. This fluctuation in reflected interrogation light is recorded as the optically detected ultrasound pulse.

The Interferometer Transfer Function(ITF)

The ITF can be expressed by the Airy function. The reflected intensity of the resonator I_R can be written as

$$I_R = I_0(1 - \frac{1}{(2F/\pi)^2 sin^2(\phi/2)}), \tag{2.1}$$

where

$$\phi = \frac{4\pi nl}{\lambda} \tag{2.2}$$

where I_0 is the incident intensity of light of wavelength λ, n is the refractive index of the medium, l is the resonator cavity length. F is the finesse, which can be defined by

$$F = \frac{\pi e^{(-\alpha_r l/2)}}{1 - e^{(-\alpha_r l)}} \tag{2.3}$$

where α_r is the energy loss coefficient of the cavity.

Energy losses in the cavity result, most significantly, from imperfect reflection of the mirrors, or from absorption/scattering within the resonator medium. In the case where these two losses are predominant,

$$\alpha_r = \alpha_s + \frac{1}{2l} \ln \frac{1}{R_1 R_2} \tag{2.4}$$

where α_s is the absorption/scattering coefficient and R_1 and R_2 are the reflectivities of the two mirrors(a value between 0 and 1). Therefore, combining the previous two equations and setting $\alpha_s = 0$,

$$F = \frac{\pi (R_1 R_2)^{1/4}}{1 - \sqrt{R_1 R_2}} \tag{2.5}$$

and when $R_1 = R_2 = R$, the finesse reaches its maximum attainable value given by

$$F = \frac{\pi \sqrt{R}}{1 - R}. \tag{2.6}$$

2.1.1 Mechanisms of Loss

There are three mechanisms by which there could be a loss of power in the resonator.

1. Absorption losses within the resonator medium.
2. Non-ideal reflection at the mirrors of the resonator, and
3. Lateral losses resulting from multiple reflections at non-normal incidence (beam

walk-away effect)

As seen above, the reflectivities of the mirrors of the resonator as well as the scattering/absorption of the medium affect the resonator finesse. In the work presented in this thesis, gold mirrors of 30 nm thickness have been used for ease of fabrication and to verify the performance improvement upon including a waveguide. However, these gold mirrors only offer about 95% reflectivity. This could be significantly improved by using dielectric mirrors, which offer reflectivities upto 99.9%. This is further discussed in Chapter 5. The following section addresses the third loss mechanism.

Effect of Waveguide

For an ideal resonator, both resonator mirrors are unconfined and perfectly reflecting, and no power is lost during the round trip. However, for a practical resonator with small mirror areas, lateral losses due to multiple reflections at non-normal incidence become significant[62]. These losses reduce the overall energy of the interferometer, which is equivalent to reduced reflectivity of the mirrors, and also cause phase dispersion due to increased path lengths. Therefore, the Q-factor of the resonator is significantly reduced.

In an optical resonator such as a Fabry-Perot cavity, these diffraction losses can be restricted by matching the shape of the wave-front to that of the mirror. There are two approaches to this: The first is to modify the shape of the mirror to exactly match the wave-front of the light, while the second approach is to restrict the light within the resonator to have a flat wavefront, while keeping the mirrors flat and parallel. In either case, the emergent wavefront matches the mirror in shape, leading to efficient recoupling of light, thus reducing losses.

In [54], the authors employ the approach of first approach; they demonstrate a plano-concave fiber ultrasound detector with impressive sensitivity (NEP=10 Pa over

20 MHz bandwidth). This device has a cavity thickness of 16 μm. Its high sensitivity is attained by a concave top mirror that is designed to match the curvature of the wavefront of the resonating optical field in the cavity. In this work, we explore the second approach where instead of matching the mirror to the shape of the wavefront, we change the wavefront to be flat and thus matched to a flat top mirror. To do that our cavity design includes a vertical waveguide that results with guided modes having flat wavefront.

Avoiding concave mirrors in the cavity has some practical advantages. The proposed fabrication method provides ease of reliable and consistent large-scale fabrication. Additionally, cavity thickness (and bandwidth) are independent of the lateral dimensions of the device. The fabrication techniques utilized in this work can be employed to scale the device to any desired thickness facilitating detection of higher frequencies. In the case of the plano-concave device [54], changing the device thickness while keeping the optimum mirror curvature would mean changing its width as well. Moreover, the method presented here is more suitable for the design of detector arrays using a fiber bundle. The sensitivity of the device reported herein is, however, significantly lower. We have measured an NEP of 350 Pa over a bandwidth of 25 MHz (see chapter 5). The lower sensitivity is mostly attributed to the fact that metallic mirrors were used in our design whereas dielectric mirrors were used in the plano-concave micro-resonator device. The potential improvement in the sensitivity of our devices upon incorporating dielectric mirrors is addressed in the end of chapter 5.

2.1.2 Performance Metrics

This section defines several parameters used to evaluate the performance of the all-optical ultrasound detectors.

Free Spectral Range

The Free Spectral Range or FSR of an optical resonator is the inverse of the round trip time (or delay) of an optical pulse. It is defined as

$$\Delta\nu = \frac{c}{2n_g l}, \tag{2.7}$$

where $\Delta\nu$ is the FSR in Hz, c is the velocity of light, n_g is the group index of the resonator medium and L is the resonator length. The FSR can therefore be used as a measure of the resonator length.

Finesse

The finesse of an optical resonator cavity is defined as its FSR divided by the full width at half-maximum (FWHM) bandwidth of its resonances. Resonator Finesse is dependent on cavity losses but independent of the resonator length.

$$F = \frac{\Delta\nu}{\partial\nu}, \tag{2.8}$$

Q-Factor

The Q-factor of a resonator is a measure of the strength of the damping of its oscillations. For an optical resonator, it can be defined as the ratio of the resonance frequency to the Full-Width at Half-Maximum bandwidth of the resonator.

$$Q = \frac{\nu_0}{\partial\nu}, \tag{2.9}$$

Alternatively, the Q factor is 2π times the ratio of the stored energy to the energy dissipated per oscillation cycle. Energy can be dissipated in one of many mechanisms of loss, discussed in the next section. These include absorption and scattering losses in the polymer medium of the resonator, as well as losses at the mirrors themselves.

The Q-factor rises as the resonator length increases, as this results in the decrease of optical losses per round trip. Very high Q resonators can be achieved by using dielectric mirrors with reflectivity >99.5%.

Visibility

Fringe visibility is defined in terms of the observed maximum and minimum intensities, and is defined as

$$V = \frac{I_{max} - I_{min}}{I_{max} + I_{min}}, \tag{2.10}$$

Visibility of the interference fringes determine the amplitude of the acoustic pulse that can be detected without saturating the sensor.

Noise Equivalent Pressure

Noise Equivalent Pressure, or NEP, is the minimum detectable pressure over a certain range of frequencies (acoustic detection bandwidth) and serves as a measure of the sensitivity of an acoustic detector. The NEP of a Fabry-Perot ultrasound detector improves with the finesse of the optical resonator. It can be defined as

$$P_{acmin} = \sqrt{\frac{4qB}{27I_0S}}\frac{\lambda}{Fn}\frac{Y}{l}, \tag{2.11}$$

where B is the acoustic bandwidth, q is the electronic charge, λ is the optical wavelength, F is the resonator finesse, Y is the Young's modulus of the resonator medium, n is the refractive index, S is the sensitivity of the photodetector and I_0 is the incident optical intensity.

While it is desirable to have the acoustic sensitivity of a detector be as high as possible (NEP as low as possible), it is worthwhile to consider the acoustic noise floor, beyond which an increase in sensitivity will not be reflected in the detected signal. A good approximation of the noise inherent to a fluid medium may be made by using the generalized approach used by Callen and Welton [63]. This paper relates the presence of acoustic radiation impedance in a medium to acoustic perturbations caused by its thermodynamic properties. Using the high temperature approximation in the paper, the mean square pressure can be expressed as

$$< P^2 >= \frac{1}{2}\pi^{-2}c^{-1}\rho k_B T \int_0^{\omega_c} \omega^2 d\omega, \tag{2.12}$$

where ω_c is the bandwidth, ρ is the density of the medium, k_B is the Boltzmann constant, T is the absolute temperature, and c is the velocity of sound in the medium. Integrating, we obtain

$$< P^2 >= \frac{\rho k_B T {\omega_c}^3}{6\pi^2 c}, \tag{2.13}$$

and taking the square root give us the acoustic noise floor in Pa. For a 40MHz bandwidth, which is reasonable for photoacoustic detection, this is about 25 Pa. Therefore, it is reasonable to say that, for this detection bandwidth, an NEP of 25 Pa is a sufficient target.

2.2 Single-Mode Waveguide

As explained above, our device incorporates a vertical waveguide within the resonator cavity to restrict lateral losses. The propagation along this waveguide can be described in terms of a set of guided electromagnetic waves, or modes, of the waveguide. Each guided mode is a pattern of electric and magnetic distributions that is repeated along the axis at equal intervals. Only a certain number of modes are capable of propagating along a waveguide, and this number is given by

$$M = V^2/2 \tag{2.14}$$

for large values of V, where

$$V = \frac{2\pi a}{\lambda} NA \tag{2.15}$$

is the V-number or V-parameter. a is the radius of the core of the waveguide, NA is the numerical aperture given by

$$NA = \sqrt{{n_1}^2 - {n_2}^2} \tag{2.16}$$

where n_1 and n_2 are the refractive indices of the core and cladding, respectively.

For values of V below 2.405, there is only one guided mode supported by the fiber. This single mode operation is desirable for high sensitivity operation of the ultrasound detector. Thus, the materials chosen to fabricate the polymer waveguide will need to have a refractive index difference that satisfies the condition for single-mode operation.

For monochromatic waves of frequency ω, a mode traveling along the z axis is given by

$$e^{j(\omega t - \beta z)} \tag{2.17}$$

where β is the z component of the wave propagation constant $K = 2\pi/\lambda$. β can only take specific discrete values for guided modes, as the mode field must satisfy Maxwell's equations as well as the boundary conditions at the core-cladding interface of the waveguide. A mode remains guided as long as

$$n_2 k < \beta < n_2 k. \tag{2.18}$$

2.3 Fiber Fabry-Perot resonator with Waveguide

The novelty of this work lies in demonstrating an alternative approach to the design of a small size, high Q-factor, polymer fiber Fabry-Perot resonator. The design incorporates a waveguide in a Fabry-Perot cavity to control diffraction losses. The new fabrication method allows for self-aligned polymer waveguide construction on a tip of a single-mode optical fiber facilitating seamless integration of detector and signal transmission fiber. In previous work, our lab has demonstrated the utility of waveguides in improving the Q-factor of Fabry-Perot resonators, but the devices were built on large glass wafer substrates and all of the instrumentation employed free space optics [64]. In this work, we present a method to achieve high Q-factor Fabry-Perot resonators by creating straight, self-aligned polymer waveguides on fiber substrates[65][66]. Subsequently, the use of this method to fabricate and characterize waveguided Fabry-Perot resonators for ultrasound detection is presented, demonstrating the improvement of waveguided Fabry-Perot resonators over those without waveguides. Optical characterization results from both devices are presented, highlighting the improved Q-factor in the waveguided case, followed by acoustic characterization to demonstrate that improved optical Q-factor leads to improved acoustic sensitivity.

Chapter 3

Simulation Studies

This chapter comprises the simulation studies done toward modelling the waveguided fiber Fabry-Perot resonator, and predicting its optical behavior. The optical simulation software tool used to perform these simulations is the RSoft Photonics Design Suite. ModePROP™ is an eigenmode expansion propagation tool within the RSoft Suite(ModePROP, Synopsys' RSoft) that accounts for both forward and backward propagation and radiation modes. It provides a rigorous steady-state solution to Maxwell's equations that is based on the highly-stable Modal Transmission Line Theory[67]. The models were designed on the RSoft CAD environment, which integrates with the ModePROP tool. All the devices simulated have been modeled using ModePROP to have cylindrical symmetry.

3.1 Simulation Studies

As described in the previous section, the device will consist of a resonating cavity between two mirrors. Because of its influence on sensitivity, the Q-factor of the resonator is one of the most important design criteria around which the device would be optimized. Considering the structure of the device, it was important to account for the following effects that negatively impact the Q-factor of the resonator:

(a) The beam broadens as it propagates within the cavity, which causes non-normal incidence on the second mirror, and in all subsequent reflections. Due to these successive reflections between the mirror at non-normal incidence, there is a loss in the power coupled back into the fiber core, i.e., power losses in the lateral direction.
(b) Any loss of energy due to imperfect mirror reflection is exacerbated because of the multiple successive reflections occurring within the cavity. Therefore, prior to fabricating the device, simulation studies were carried out on the Rsoft Design Suite software with the view to understand the impact of these losses on Q-factor and the best device design for minimizing them.

3.1.1 Waveguide to Address Diffraction Losses

In order to visually demonstrate the efficacy of a waveguide in restricting beam walk off upon transmission over a distance corresponding to several round trips, a simulation study was set up. This simulation has been performed over a thickness of 1000 μm even though the envisaged final device thickness is only about 20 μm in order to understand and compare the beam divergence for the two cases that would result after multiple round trips within the resonator. The refractive index of the material within the cavity was set to 1.5 (comparable to glass). The optical field in the polymer was studied to understand the distribution of energy. As seen in Figure 3.1(a), the near-infrared (NIR) field spreads in the polymer to a diameter of around 100 μm at an axial distance of 800 μm from the source. A second simulation was done to evaluate the effectiveness of including the waveguide in containing the field distribution. This was done by selectively modifying the refractive index of the waveguide to mimic the core and cladding of the fiber (1.506 and 1.500, respectively). The results of this simulation are seen in Figure 3.1(b). Without a waveguide, there is significant lateral loss in power over a transmission of 1000 μm. In the case of the device with waveguide, for a distance of 1000 μm (25 round trips for a 20 μm-thick device), the power is still restricted within the 9 μm core, proving the efficacy of the waveguide in reducing lateral losses.

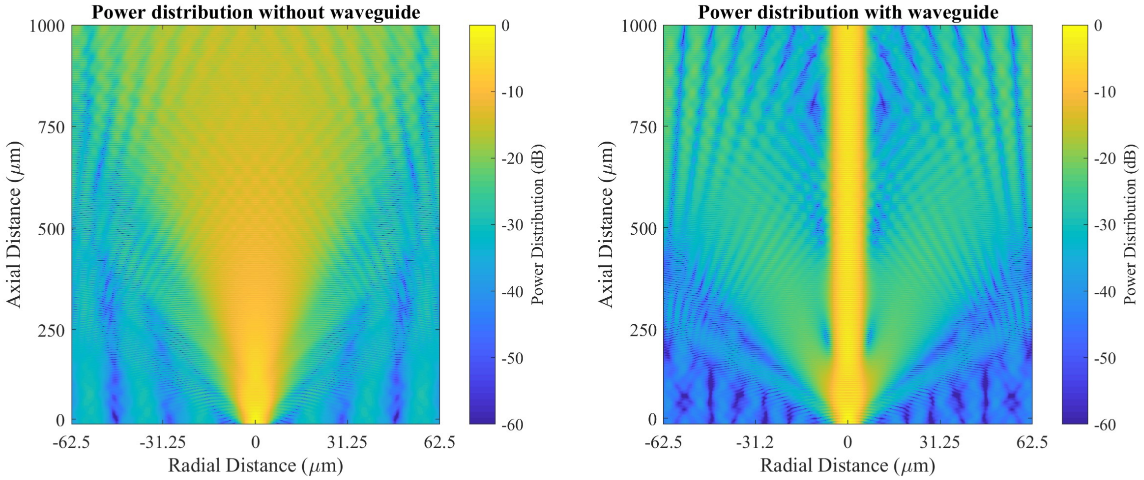

Figure 3.1: Simulation results showing power distribution in dB for Fabry–Pérot interferometer devices (a) without a waveguide and (b) with waveguide.

A subsequent simulation of the full device with real dimensions is presented in Figure 3.2, which shows a quantitative confirmation of the same effect via improvement in Q-factor. The values of the refractive indices assigned to the waveguide and surrounding portions of the polymer were 1.506 and 1.500, respectively. A 45-μm cavity was simulated between two gold mirrors of 30-nm thickness with and without a waveguide. The corresponding optical resonances confirm that the Q-factor was seen to improve significantly—from 1853.33 without a waveguide to 3173.04 after including a waveguide.

Since beam divergence increases with higher thickness, it was expected that the improvement with including a waveguide would be more drastic for thicker devices. To confirm this, a study was done comparing the improvement with the introduction of a waveguide for three different Fabry–Pérot interferometer thicknesses, 20, 45, and 80 μm. These thicknesses correspond to FSR of 40, 17, and 10 nm, respectively. As

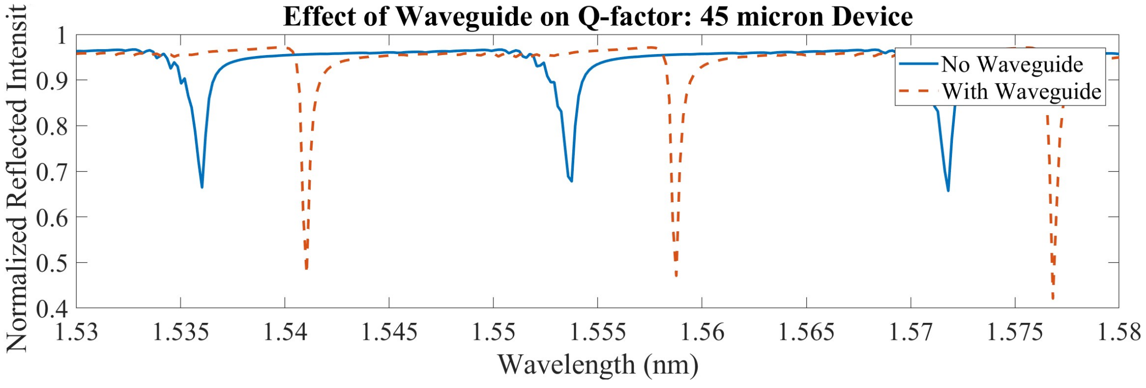

Figure 3.2: Improvement in Q-factor of the resonator upon introduction of waveguide.

Device thickness (μm)	80	45	20
Change in Q-Factor	3034 to 4779	1853 to 3173	1301 to 1403

Table 3.1: Improvement in Q-factor upon the introduction of the waveguide for different thicknesses.

expected, the improvement in Q-Factor with the presence of a waveguide is seen to increase with cavity thickness Figure 3.3. The improvement in Q-factor upon the introduction of the waveguide was highest for the 80-μm device, from 3034.01 to 4779.94. In the case of the 45-μm device, the improvement was reduced, and the Q-factor changed from 1853.33 to 3173.04. The least improvement, from 1301.04 to 1403.46, was observed in the case of the 20-μm device. These simulations served as a confirmation that a self-aligned waveguide would provide significant improvement to the Q-factor of the device 3.1.

3.1.2 Effect of Mirror Reflectivity

In the work discussed in the previous section, the mirrors for the resonating cavity were 30-nm gold layers. Gold was chosen as a mirror for the preliminary design because of the ease of fabrication, sufficient reflectivity at NIR wavelengths ($\sim$ 95%) used for interrogation of the cavity, and poor reflectivity at UV wavelengths, which need to penetrate the gold layer to cure the epoxy—the optical medium of the res-

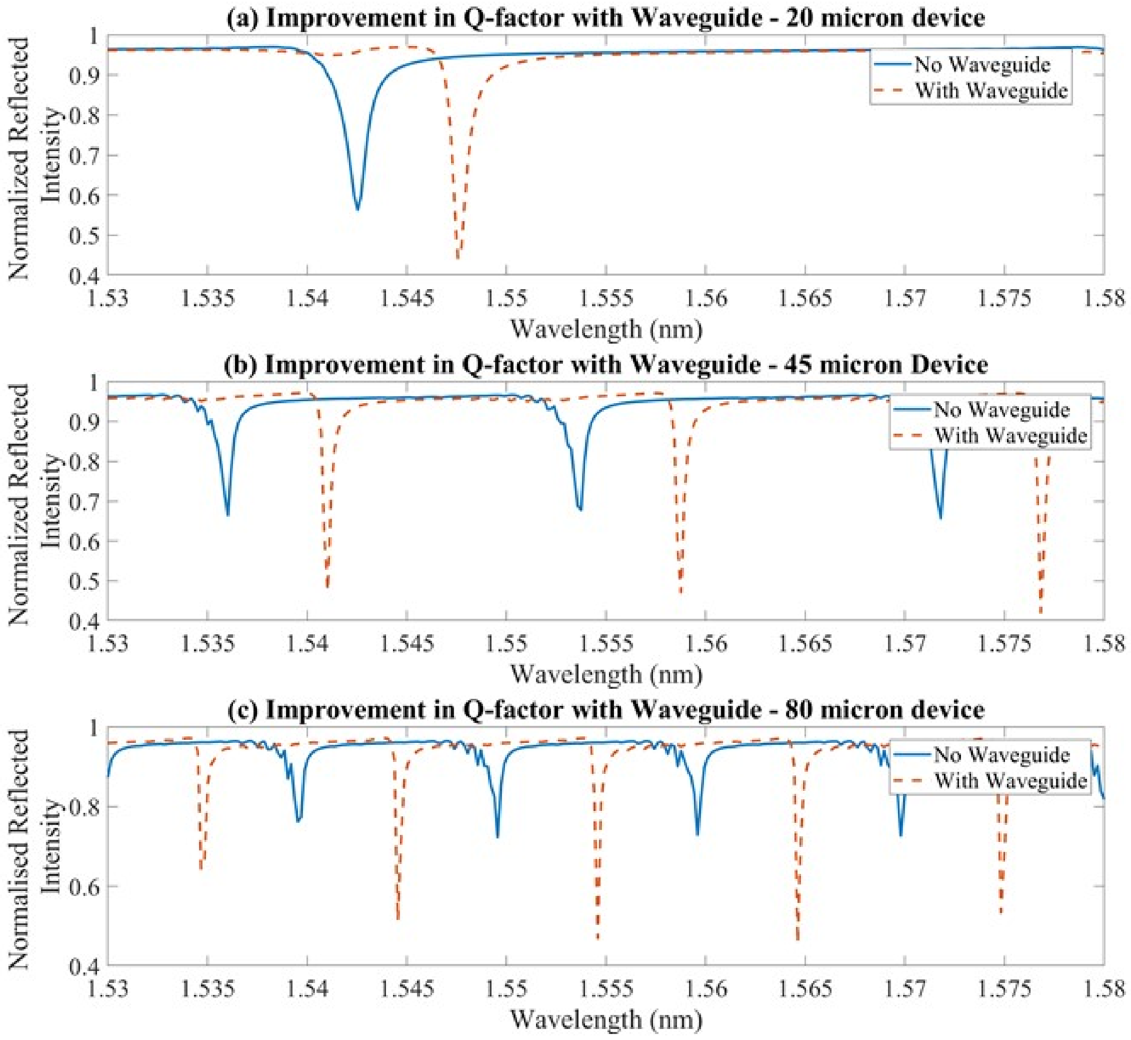

Figure 3.3: The improvement of Q-Factor with the presence of a waveguide for different cavity thicknesses.

onator. However, since there are multiple successive reflections, there is significant energy lost from the cavity even with 95% reflectivity offered by the gold mirrors. Since the finesse, and therefore, the Q-factor of the resonator depend on mirror reflectivity,[68] the Q-factor for devices with gold mirrors was not very high. This can be improved using dielectric Bragg mirrors instead.

Dielectric mirrors consist of multiple thin layers of (usually two) different transparent optical materials and offer very high reflectivity (above 99%) because the reflections from the multiple interfaces constructively interfere. Bragg mirrors comprise several dielectric layers, each of which has a thickness equal to quarter of the design wavelength. This design leads to the highest possible reflectivity for a given number of layer pairs and given materials. Tadayon et al., in [64], used similar Bragg mirrors in their Fabry–Pérot interferometer in large size multimode devices, consisting of eight quarter-wavelength layers of titanium dioxide (n $\equiv$ 2.19) and seven quarter-wavelength layers of silicon dioxide (n $\equiv$ 1.46), designed for high reflectivity at 1550 nm.

A 45-μm thick cavity simulated using this design showed an improved Q-factor of 7855.96 as compared to 2095.32 with gold mirrors, as seen in Figure 3.4. Including a waveguide structure in addition to the dielectric mirrors further improved the Q-factor of the device to 10827.66. This is especially significant as it implies that high Q-factors may be achieved even at lower thicknesses, which allows for greater acoustic bandwidths.

3.1.3 Planar Versus Plano Concave Simulation Models

The planar structure described in sections 3.1.1 and 3.1.2 provides a simplified model to test the improvement in Q-factor upon the inclusion of a waveguide. However, this does not accurately describe the structure fabricated on the tip of a single-mode fiber. Dip-coating of the epoxy would result in a plano-concave structure due to

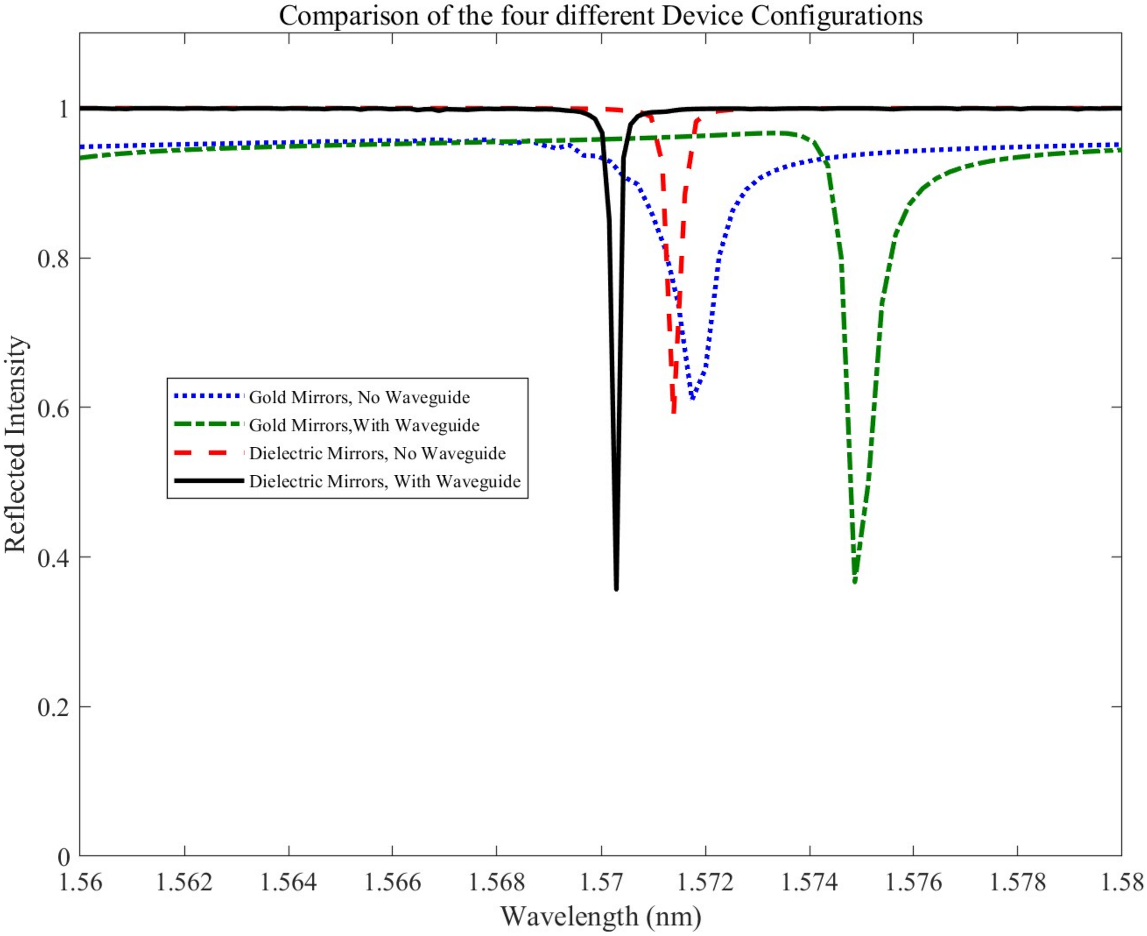

Figure 3.4: Q-factor enhancement with waveguides and dielectric mirrors.

surface tension holding the epoxy on the fiber tip surface. In order to accurately model this and understand the effect of cavity shape on the device performance, the planar simulation model was studied in comparison to plano-concave structures. The largest contact angle possible for a planoconcave device would be 90°, resulting in a hemispherical drop. For lower contact angles, a gentler curvature on the droplet can be expected. Figure 3.5 shows a comparison of the optical characteristics of planar and hemispherical devices plotted alongside the focused plano-concave cavity created with the dimensions of the device presented by Guggenheim et al[54]. The total height of the planar and hemispherical devices was kept the same for a fair comparison.

The hemispherical device showed a negligible Q-factor of 387.18 (finesse of 3.22) in comparison to the planar cavity with Q-factor of 3123.17 and finesse of 26.23 for the planar device. This difference is because the hemispherical cavity is unable to focus light effectively back into the fiber cavity. The focused plano-concave model, on the other hand, can do so most effectively as its curvature exactly matches the emerging wave front. This approach has been used to improve finesse by a factor of 4 as compared to planar devices[69]. An important difference in our approach, however, is the presence of a waveguide— implying a flat wave front as opposed to the divergent beam that would be present in a device without a waveguide. This dictates that we require the second mirror to be as flat and parallel to the first mirror as possible for optimal performance. In order to understand the effect of the device curvature in the case of waveguided devices, a second set of simulations was performed, comparing waveguided hemispherical and planar cavities, presented in Figure 3.6

As expected, the performance of the planar cavity surpassed that of the hemispherical cavity as the flat second mirror is better suited to reflect the plane wave front that emerges from the waveguide.

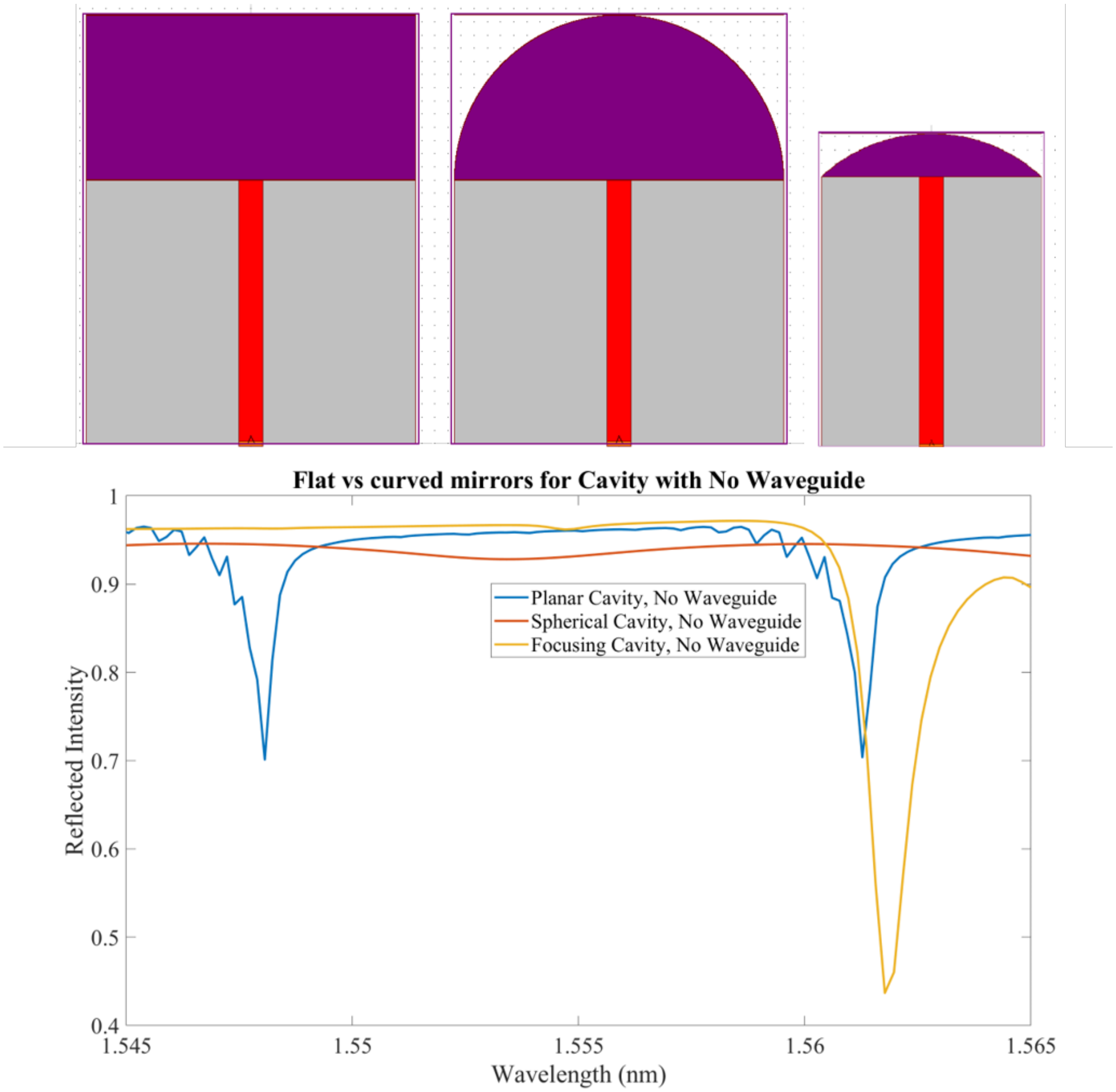

Figure 3.5: Comparison of characteristic curves of (a) planar, (b) hemispherical, and (c) focusing resonator structures.

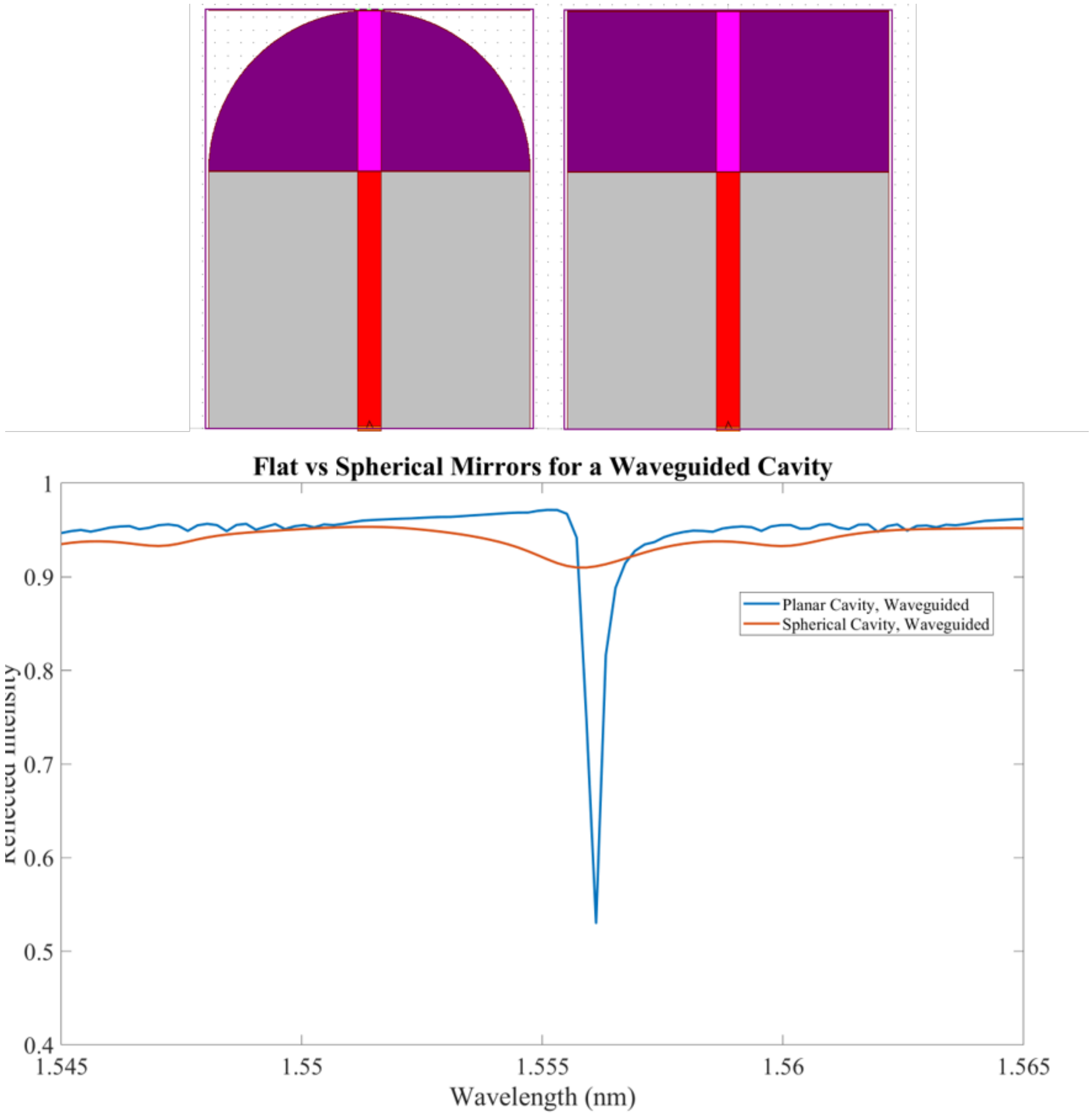

Figure 3.6: Characteristic curves of hemispherical and planar waveguided cavities illustrate the importance of having a flat mirror for waveguided cavities.

3.1.4 Plano-Concave Resonators with Gentle Curvature Approaching Flat Mirrors: the Fiber-Ferrule Device

Although it is possible to control the curvature of the concave second mirror to an extent using epoxies with different contact angles, it is difficult to achieve the flat parallel resonator structure required for optimal performance of the waveguided device on a bare fiber. One way to achieve this is to insert the fiber into a ferrule and use the larger surface area to deposit a flat parallel mirror. This approach was evaluated through simulations using a model based on dimensions resulting from experimental measurements of dip-coating using a fiber-ferrule assembly (described in Chapter 4). The distance between the tip of the pillar and the second mirror can be varied depending on how far beyond the surface of the ferrule the fiber is placed and secured. To determine to what extent this positioning might affect the device Q-factor, and therefore, the tolerance on the position of the fiber with respect to the ferrule, a set of simulation models were designed to scale (for the portion of the device demarcated in Figure 4.11 using the contact angle of 37° from the experiment described in Chapter 4, and the ferrule surface of diameter 1.8 mm.

As shown in Figure 3.7, it is observed that the distance between the tip of the fiber and the second mirror significantly affects the Q-factor. The Q-factor for the device without a waveguide was 1558.30 (finesse 14.11), and those of the devices with waveguides that were 75%, 85%, 95%, and 100% of the total height of the device were 3113.59 (finesse 26.20), 3916.51 (finesse 32.22), 5255.45 (finesse of 39.79), and 5205.40 (finesse 40.40), respectively. From this study, it was inferred that the fiber must be positioned above the ferrule at a position such that the waveguide structure is at least 90% of the total device height. Running this test also provides us with the best estimate for the Q-factor of a device fabricated using this approach. As discussed in Chapter 5(Figure 5.10), dielectric mirrors in place of the gold mirrors used would

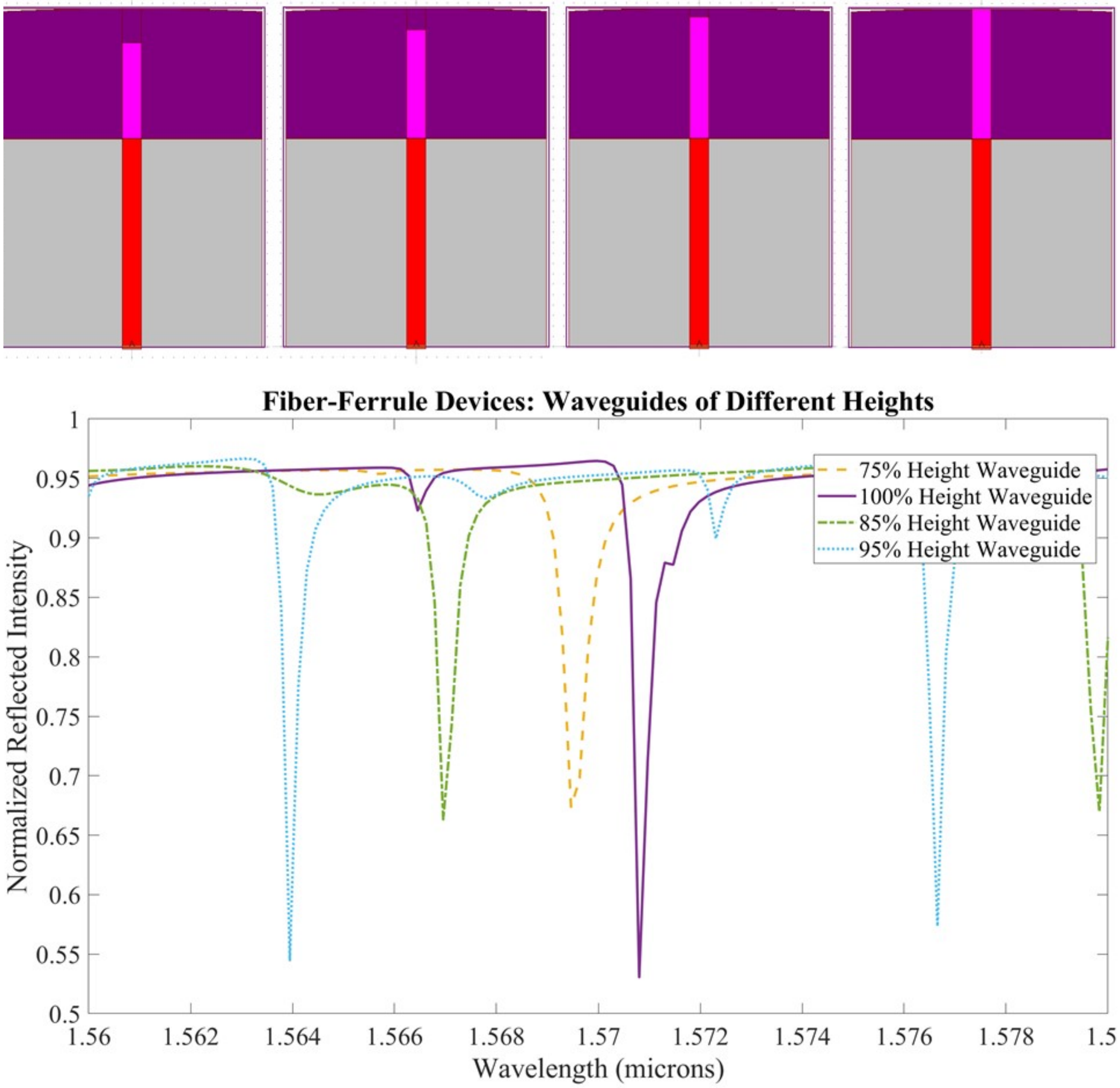

Figure 3.7: Simulations run to estimate the tolerance on distance of the fiber tip from the second mirror and the associated characteristic curves.

result in a significantly higher Q-factor.

These simulation studies served to highlight the importance of having flat and parallel mirrors for resonators with waveguides. The following chapters explore the fabrication methods employed to achieve this design, and the characterization of the resulting devices.

Chapter 4

Toward a highly sensitive polymer waveguide fiber Fabry–Pérot ultrasound detector

This chapter describes the material and mechanical design considerations for the fabrication of the fiber Fabry-Perot ultrasound detector. Different photo-sensitive polymers were evaluated for their use as the material to create the resonator waveguide, followed by the construction of an encapsulated waveguide device to study the optical performance of the device. The content of this chapter was published as a research article in the *Journal of Biomedical Optics* by Thathachary and Ashkenazi [66]

4.1 Self-Aligned Polymer Waveguides

Polymers are a natural choice as the resonator medium for the ultrasound detector since they have a lower Young's modulus than glass. In order the create a single mode polymer waveguide within the body of the resonator, it is necessary to generate a step refractive index profile, with the waveguiding core having a higher refractive index. This can be achieved by using photo-polymers whose refractive indices can be changed, typically by exposure to UV wavelengths. Additionally, for ease of fabrication it is convenient to write the waveguide by illuminating from the back end of the fiber. This would result in self-aligned waveguides - a simpler alternative to alignment and illumination from the front. Thus, desirable properties of the polymer are tunable refractive index, good absorption at UV wavelengths and transparency at the NIR wavelengths used for interrogation. In the following sections, the experiments done to evaluate two photo-polymer types are described.

4.1.1 Benzo-Cyclo-Butene Waveguide devices

Since it was determined that our design for the device would involve creating a waveguide structure within the cavity of the resonator, it was imperative to identify a photosensitive polymer that would allow modification of refractive index upon appropriate exposure. A survey of literature led to the choice of the polymer Benzocyclobutene, or BCB, which undergoes a change in refractive index upon exposure to UV, as suggested by Liang-Yin Chen et all [70]. The advantage of this polymer is that it is cured by heat, and therefore is solid while writing the waveguide onto it using UV. Thus, by exposing the fiber resonator to UV from the back end, it would be possible to write a self-aligned single mode waveguide into the cavity.

Refractive Index Change in BCB

To determine the extent of refractive index change that could be induced in BCB upon exposure to UV, a polymer square wave phase grating was designed. The fabrication of this grating involved spinning the Polymer (BCB-46) to a thickness of 5 μm onto a 1-inch circular glass wafer and curing at 500°F for 1 hour. Subsequently, the square wave grating was written onto the polymer by exposing the cured polymer film to a 355 nm UV pulsed laser (for 45 minutes at 0.5 μW, 1000 Hz) through a mask.

The mask had a square wave pattern of periodicity 10 μm (50% duty cycle) written onto it. The exposed areas undergo a change in refractive index, and to estimate the value of this change in refractive index, Δn, the phase grating was illuminated with a 655 nm red laser, and the intensity of the various diffracted modes was measured. Diffraction efficiency of the nth mode is defined as the ratio of incident intensity to the intensity of the nth mode. Using the expression derived for diffraction efficiency for the first mode of a square wave phase grating:

$$\eta_1 = \frac{2}{\pi^2}(1 - cos(\Delta\phi)), \tag{4.1}$$

the change in phase, $\Delta\Phi$,was found to be 0.1627 radian. The corresponding change in refractive index, Δn, was 3.392 x 10^{-3},

$$\Delta\phi = \frac{2\pi t}{\lambda}\Delta n, \tag{4.2}$$

where t=thickness of the BCB layer (5 μm), and Λ= readout wavelength (655 nm). Since the refractive index difference between core and cladding in an optical fiber is comparable to this number (Single mode fiber SM980-5.8-125 from Thor Labs Inc. has index difference of 0.006 between core and cladding), it was concluded that the refractive index change to be induced in the BCB layer for wave guiding could be achieved by using the 355 nm laser. To understand how this induced refractive index change, Δn, varies with increase in exposure time to UV, the above experiment was repeated with 4 different samples, exposed for 1 hour, 2 hours, 3 hours and 4 hours respectively. The results from this experiment are summarized in the table 4.1below.

The above test confirmed that the exposure would have to be around 2 hours to induce a refractive index change of about 4×10^{-3}. In order to achieve the same refractive index change on the fiber optic device, exposure time was expected to vary because (i) the amount of UV energy that can be coupled into the fiber would affect

Exposure time (hours)	1	2	3	4
Delta-n(x 0.001)	3.796	3.996	7.380	7.629

Table 4.1: Variation of induced Refractive Index change in BCB with exposure time

the process, and (ii) the exposure to UV for the fiber optic device would be done through a single Gold mirror and reflection/absorption by this layer would have to be taken into account.

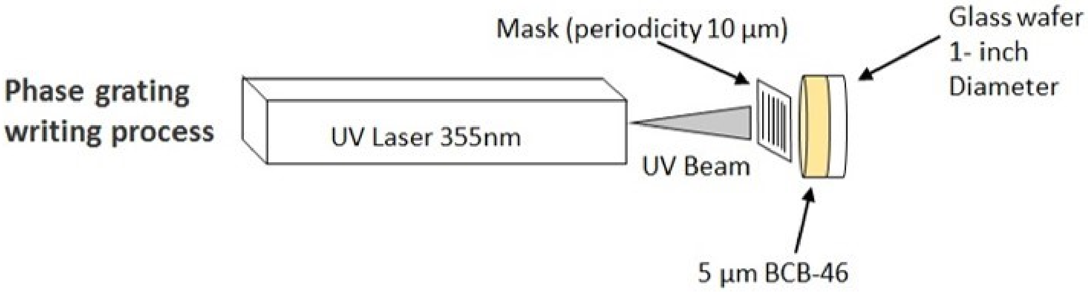

Figure 4.1: Writing a phase grating to determine the grating efficiency, and thus refractive index change, in Benzo-Cyclo-Butene photosensitive polymer

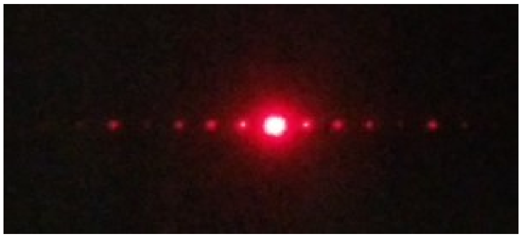

Figure 4.2: Read-out pattern using a 655 nm wavelength red laser: Diffraction efficiency of the grating was used to determine the refractive index change induced in BCB.

Fiber Device Fabrication

A single mode optical fiber with 9µm core, 125 µm cladding and a coating of Polyimide for protection against high temperatures was chosen as the base for the device. This fiber was then inserted into a glass ferrule of 1.8mm diameter to increase the surface area for ease of fabrication. The fiber-ferrule assembly was then polished on polishing paper of various grain sizes so as to have a perfectly smooth surface on which to construct the transducer. A fabry-perot resonator was then constructed on this fiber substrate. The mirrors of the cavity were Gold films 30 nm thick, deposited using electron beam evaporation. A 70 µm layer of the BCB polymer was then sprayed on the first mirror using an air brush. The four factors which determine the thickness include the concentration of the polymer solution, distance of the sample from the tip of the airbrush, the pressure of the gas used and the duration of the spray coating procedure. The device was then tested for optical resonances using a fiber circulator and a tunable NIR laser source with a wavelength range of 1510-1640 nm. Resonance was observed, with a free spectral range (FSR) of 11.5 nm, as seen in the blue curve in 4.4. The device was then exposed to UV via the fiber connector as shown in 4.3 in order to write the self-aligned waveguide and the resonance retaken as seen in the red curve in 4.4.

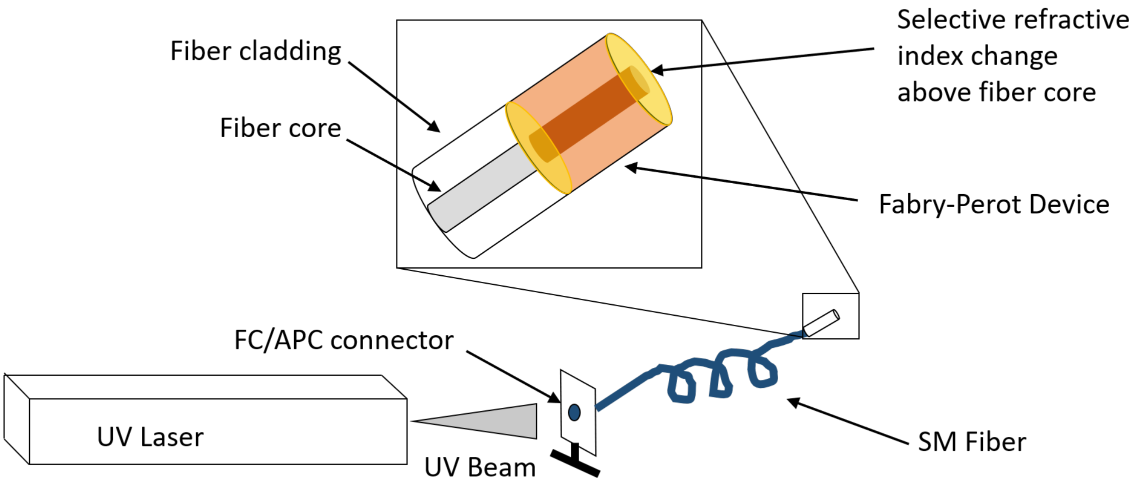

Figure 4.3: Setup used to write the self-aligned waveguide into the BCB layer of the fiber Fabry-Perot device.

Optical Characterization

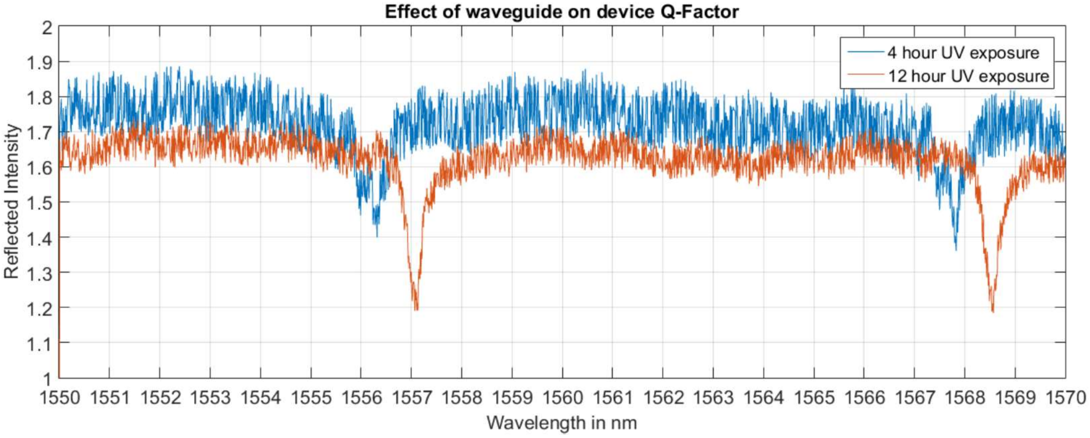

Figure 4.4: Resonance measured for the prototype, showing the increase in Q-factor from exposure of 4 hours to 12 hours. The device is seen to have a FSR of 11.5 nm, which corresponds to thickness of around 70 μm.

While there did appear to be improvement in the Q-factor after writing the waveguide, this improvement did not appear to be consistent with simulation studies. We hypothesized that this was due to the extinction of UV light within the thick BCB layer. To confirm this, a transmission measurement was made of 355 nm UV light through a 5 μm BCB layer deposited on a glass slide. It was observed that the incident intensity dropped to 30% of its value after passing through this layer. By using the equation

$$I_t = I_0 e^{-\alpha l}, \tag{4.3}$$

it was confirmed that the absorption coefficient was around 240000 m^{-1}, where I_t is the transmitted intensity, I_0 is the incident intensity, α is the absorption coefficient and l is the thickness of the layer, in this case 5 μm. The penetration depth, therefore, is around 4 μm. Therefore, the penetration depth for 355 nm was not enough to write into the entire >20 μm thick device in a single step.

This problem could be overcome by either altering the concentration of the BCB by diluting it with an appropriate solvent, or by building the device and writing the waveguide in steps, where each layer was a sufficiently small thicness for the 355 nm to penetrate. While it is possible to pursue these directions, an alternative method using optical epoxies was found to work more suitable, as described below.

4.1.2 Optical Epoxy Waveguides

Another method to create polymer waveguides in the fiber was to use two different polymers, one for the core and one for the cladding, and complete the fabrication in two steps. For this, the polymers would need to have different refractive indices. This option was explored using optical epoxies from Norland Inc. Writing self-aligned waveguides was possible using these epoxies as they solidify upon exposure to UV light and thus the light dictates the shape of the pillar formed.

Fiber Device Fabrication

The first iteration of devices fabricated consisted of planoconcave Fabry–Pérot interferometers constructed on singlemode optical fibers 125-μm diameter. The following steps were followed for fabrication, as presented in our earlier work:[66]

1. The single-mode optical fiber substrate with 9-μm core and 125-μm cladding was stripped and cleaved to produce an optically smooth surface.

2. A 30-nm gold layer was deposited on the polished surface by e-beam evaporation, forming the first mirror of the resonator, as shown in Figure 4.5(a).

3. The gold-coated fiber tip was then dipped into a vial of UV curable epoxy Norland Optical Adhesive (NOA) 81 having refractive index 1.56. The speed of immersion and retraction as well as the depth of immersion were controlled so as to obtain a droplet on the fiber tip, as shown in Figure 4.5(b). 4. The droplet was exposed to a UV lamp

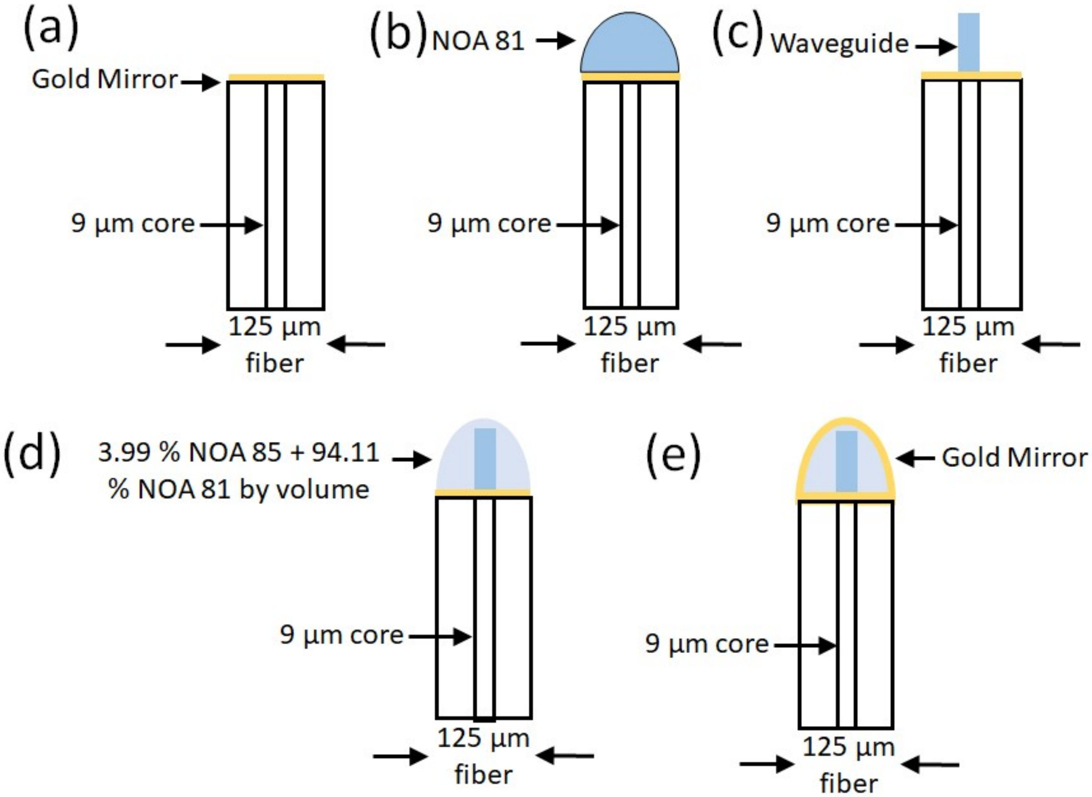

Figure 4.5: Fabrication steps for fiber device: (a) first mirror deposited on fiber, (b) dip coating in waveguide epoxy, (c) pillar obtained by selective curing, (d) dip coating in cladding epoxy, and (e) deposition of second mirror.

(Omnicure S1000) having wavelength range of 320 to 500 nm. The exposure was done through the fiber connector, thus selectively curing only the portion of epoxy directly above the core. The fiber tip, along with the partially cured droplet, was then washed in acetone, resulting in an epoxy pillar as pictured in Figure 4.5(c). A microscope image of the same is seen in Figure 4.6(a).

5. A mixture of epoxies NOA 85 and NOA 81 was made choosing the rations of the two polymers to achieve an effective refractive index 1.556. The fiber tip containing the pillar was then dipped in this mixture to create the cladding of the device, as seen in Figure 4.5(d).

6. This cladding was flood exposed to UV from the front side, thus curing the entire droplet, with the pillar of higher refractive index embedded at its center. A second 30-nm gold layer was then deposited, completing the resonator, as seen in Figure 4.5(e). A microscope image of the completed device is seen in Figure 4.6(b).

As seen in Figure 4.6(a), the wave-guiding pillar was not straight and flat as desired but rather had an irregularly shaped tip, which would adversely affect the performance of the device by distorting the emerging wave front. Experiments conducted to further understand the cause for this are presented in subsequent sections. The completed device was then tested for optical resonance and the results are presented below.

Fiber Device Characterization

The completed device was then tested for optical resonance on a tunable NIR laser of wavelength range 1510 to 1640 nm via a fiber circulator. Results are as shown in Figure 4.7. The top graph shows results obtained on a device manufactured without a waveguide. In this case, the FSR is 2386 GHz. This corresponds to a droplet height of 40.29 μm. The Q-factor and finesse of this device were found to be 5139.80 and 62.79, respectively. The bottom graph shows the improved sensitivity in a device fabricated

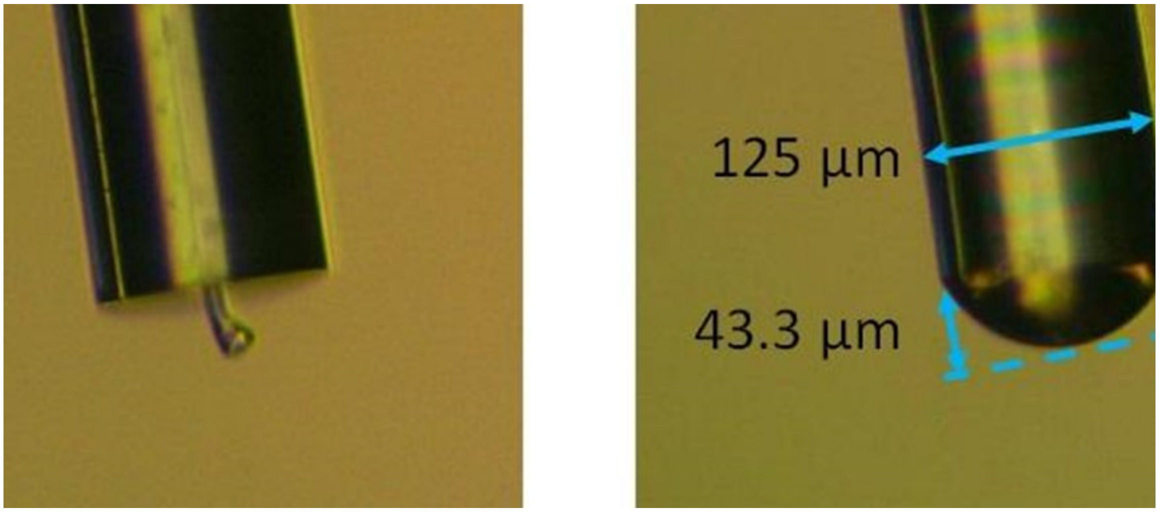

Figure 4.6: Microscope images of the device (a) after fabrication of the wave-guiding pillar and (b) after the dip-coating of the surrounding epoxy.

including a waveguide. In this case, the Q-factor and finesse are calculated to be 7728.50 and 93.94, respectively. In addition to optical testing, the device without waveguide was also tested for acoustic sensitivity. For this, a protective conformal Parylene coating of 2 μm was deposited on the device. An Olympus NDT transducer of 25 MHz with a focus at 1" distance was used as a transmitter. After characterizing the pressure using an ONDA Hydrophone, as seen in Figure 4.8, the hydrophone was replaced with the fiber optic sensor and pressure measurements taken, as seen in Figure 4.9. The NEP estimated was 21.85 kPA. Several factors could contribute to this high value of NEP value, such as noise introduced by the photodetector used (FPD 510, Menlo Systems), and outdated calibration data for the Hydrophone. Future work planned includes experiments to investigate and eliminate these noise sources.

Although the optical characteristics showed a slight increase in the case of the device with waveguide, the sensitivity, and therefore NEP, of these devices could be vastly improved by addressing the non-ideal shape of the pillar. Methods to do so are described in the following sections.

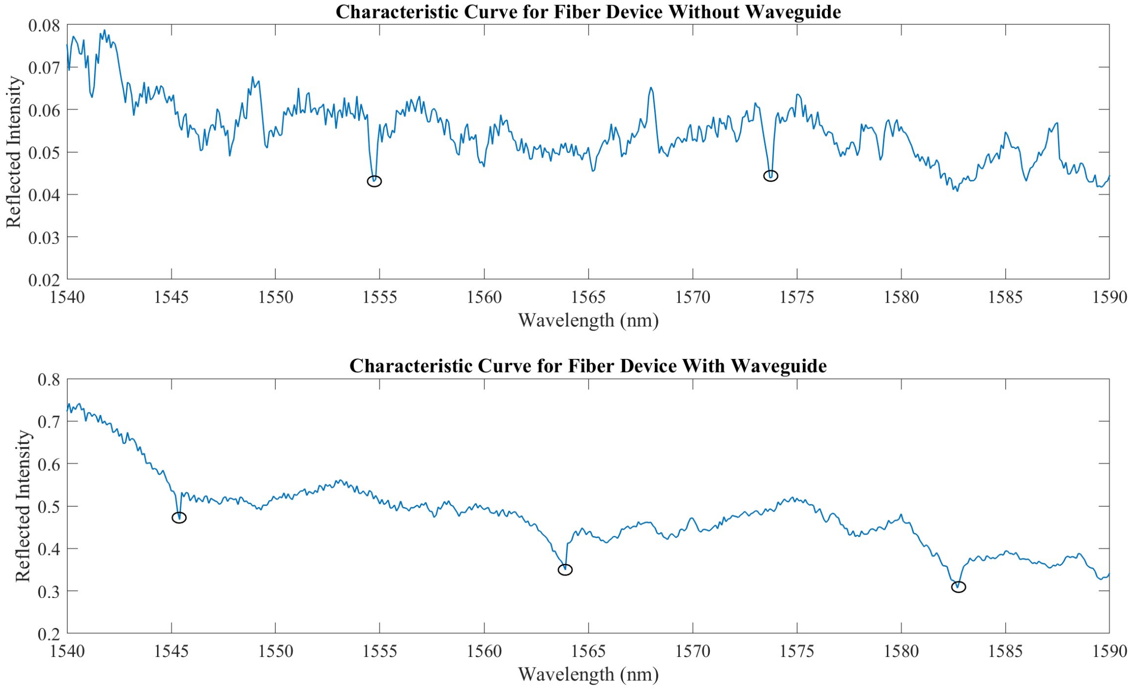

Figure 4.7: Characteristic curves of the device (top) without waveguide and (bottom) with waveguide. Encircled points represent the resonant peaks.

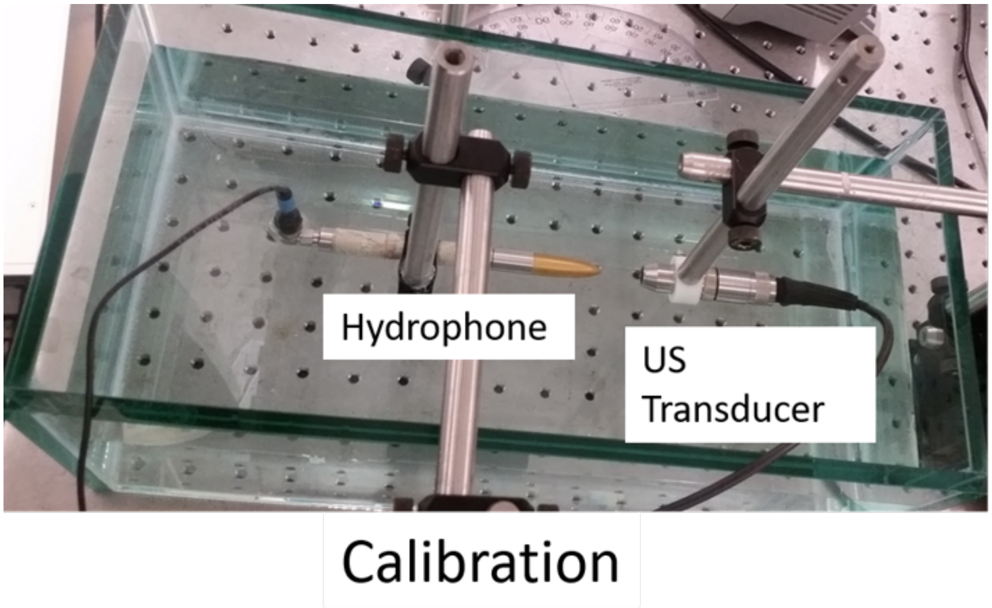

Figure 4.8: Measurement of the acoustic output of the commercial transducer using the calibrated Hydrophone

Fiber-Ferrule Device Fabrication

The Q-factor, and therefore sensitivity, of the interferometer increases with greater thicknesses as seen in Figure 3.3. However, it is also desirable to have a thin device in order to improve the sensing bandwidth, leading to a trade-off between these parameters for an optimal design of the ultrasound detector. Additionally, the surface tension of the concave droplet on the fiber tip would not allow the second mirror of the resonator to be parallel to the first, and the resonator would have to be a certain thickness dictated by the shape of the concave droplet. To fabricate resonator mirrors that are as flat and parallel to each other as possible, a method is proposed that employs a glass ferrule to hold the fiber. This increases the surface area available for dip coating of the cladding and thus offers control over the curvature of the cladding and the second mirror. Additionally, the thickness can also be scaled as required. This process was developed to obtain the dimensions for the model presented in Figure

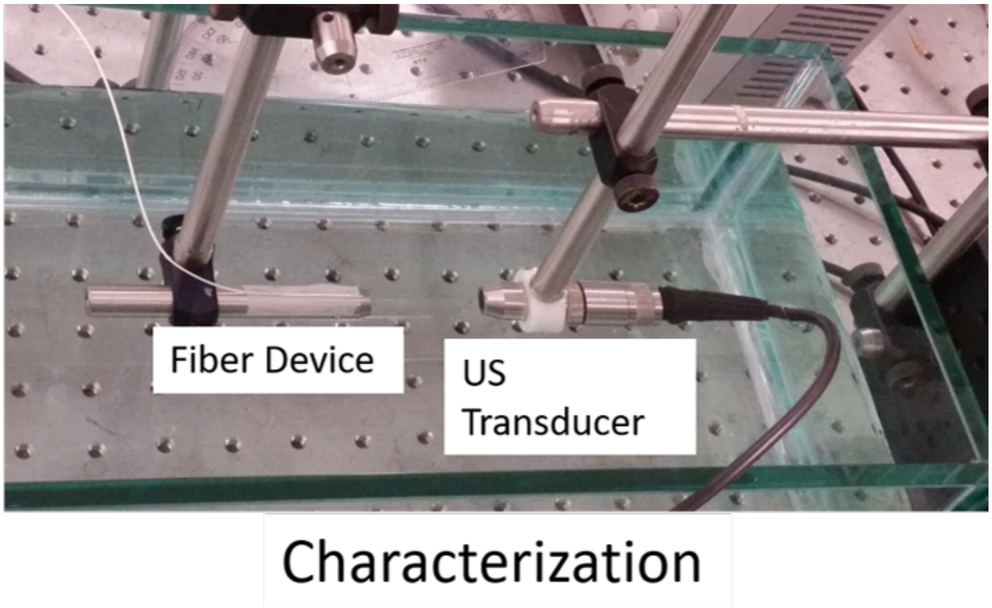

Figure 4.9: Characterization of the acoustic performance of the fiber device

3.7, as well as to confirm the feasibility of depositing mirrors with gentler curvature than a hemispherical droplet.

Figure 4.10 shows the fabrication method proposed. First the 125-μm bare fiber is inserted into a glass ferrule with inner diameter 125 μm and outer diameter 1.8 mm and secured using UV-cured epoxy. The fiber surface is above the ferrule surface as shown in Figure 4.10(a). Thereafter, the first mirror is deposited using e-beam evaporation. The gold-coated fiber tip is then dipped into the high-refractive index epoxy used to manufacture the waveguiding pillar resulting in a droplet as shown in Figure 4.10(b). The dipped fiber is then exposed to 405-nm UV light through the back connector, and then washed in acetone to remove the uncured epoxy. This results in the waveguiding pillar as depicted in Figure 4.10(c). To form the cladding, the combination is dipped into the cladding epoxy to the level of the ferrule, as shown in Figure 4.10(d). This results in a droplet with a certain contact angle, depending on the epoxy. As an example, the ferrule shown in Figure 4.11(b) resulted in a contact angle of 37 deg when dipped in epoxy stereolithography (SLA) 3-D printer resin. Since this curve is spread over a relatively large area of diameter 1.8 mm as compared to the 125-μm diameter of the fiber, the portion of the mirror above the fiber is almost parallel to the first mirror—meeting this important requirement for the waveguide device as described above.

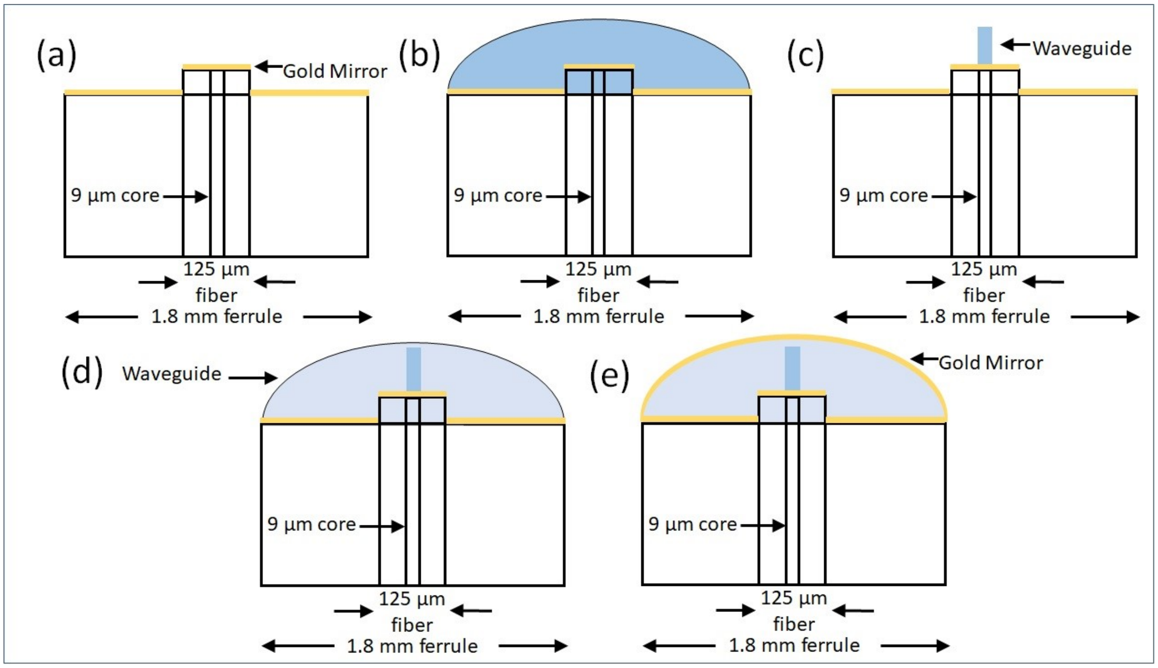

Figure 4.10: Fabrication process proposed for fiber-ferrule devices: (a) first mirror deposited on fiber affixed to ferrule, (b) dip coating in waveguide epoxy, (c) pillar obtained by selective curing, (d) dip coating in cladding epoxy, and (e) deposition of second mirror.

As seen in Figure 4.10(d), the distance between the tip of the pillar and the second mirror can be varied depending on how far beyond the surface of the ferrule the fiber is placed and secured. As shown in Figure 3.7, it is observed that the distance between the tip of the fiber and the second mirror significantly affects the Q-factor.

Since the goal is to fabricate this device at the smallest possible size scale, it would be desirable to separate the fiber from the ferrule once the device has been completed.

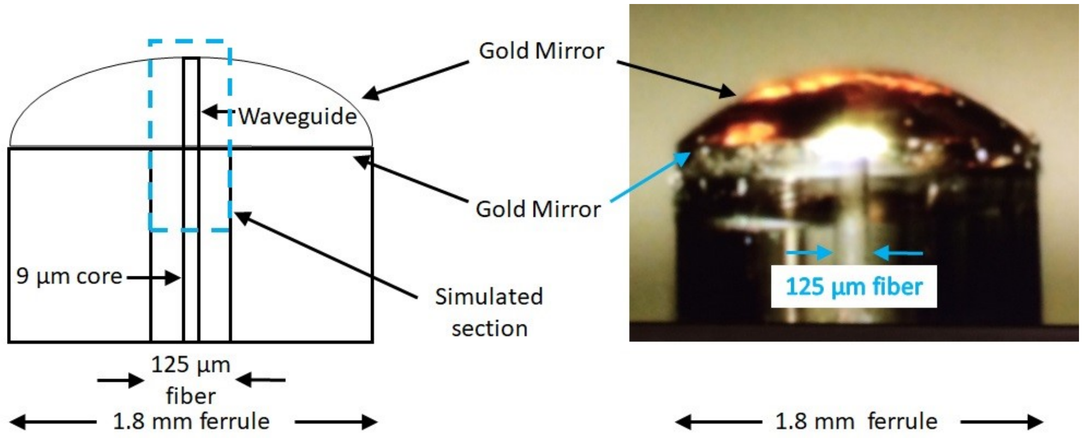

Figure 4.11: Fiber-ferrule assembly highlighting (a) the simulated section and (b) a photograph of the same used for contact angle estimation.

There are several ways this can be done:

1. The device can be made on a double clad fiber inserted into the ferrule. In this case, the cladding of the device can be selectively cured using the outer cladding of the fiber, allowing the use of the ferrule to achieve the desired contact angle but still separate the device after fabrication.
2. The portion of the device directly above the fiber can be selectively cured from above using a mask/focused exposure.

Pillar Shape and Refractive Index Tuning

The greatest challenge in our work so far has been to control the shape of the epoxy pillar produced, which serves as the waveguide. A perfectly flat waveguide is essential in order to preserve the flat wave front emerging from the fiber core. To understand the process of UV-curing within the polymer, two sets of experiments were conducted. First, the hemispherical drop of epoxy on the fiber tip resulting from dip coating was exposed to UV light through the fiber connector while varying the duration of exposure. The fibers were then washed in acetone, and the resulting pillars imaged under the microscope. As seen in Figure 4.12, the pillars obtained from shorter duration exposures are seen to have a sharp, pointed tip, rather than the desirable cylindrical shape, and a larger mass appears to cure on top of this pointed pillar when exposure time is increased to 60 s. To better understand the shapes of the pillars produced, the study was repeated while keeping the fiber tip immersed in a bulk volume of the epoxy during curing and washing in acetone thereafter. As expected, the shapes obtained reflected complex geometries.

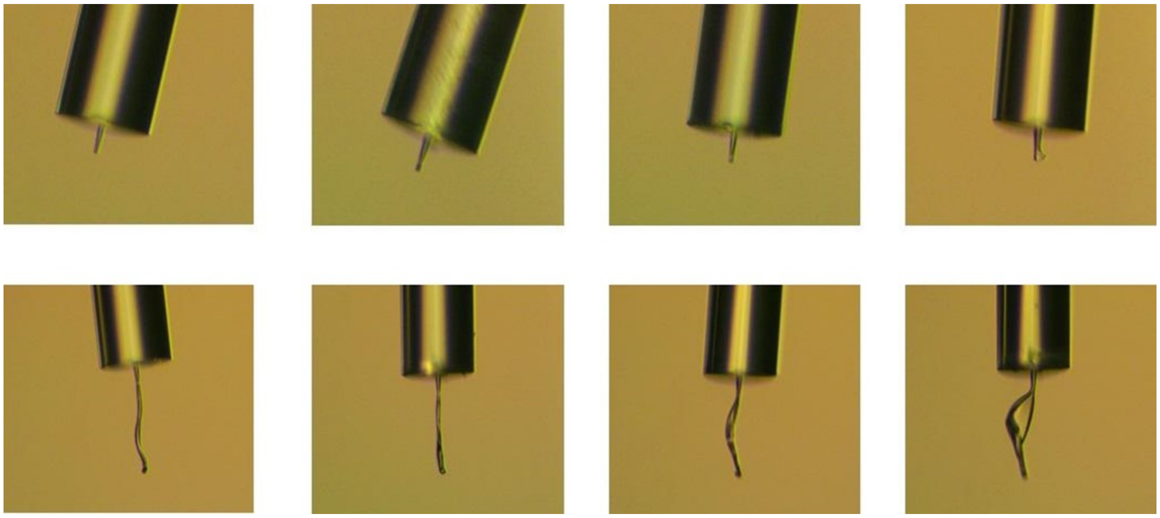

Figure 4.12: Comparison of epoxy pillars resulting from (top row) droplet cure and (bottom row) bulk cure for cure times of 30 s, 60 s, 2 min, and 5 min.

A possible reason for this could be because the UV source used to cure the epoxy was broadband, containing wavelengths from 320 to 500 nm, and the fiber is not a single-mode conductor for UV wavelengths. In addition, the curing of the epoxy is a dynamic process, in which portions of the epoxy that get cured first decide the path for UV light reaching the volume beyond. Therefore, it was desirable to use longer wavelengths so that their penetration depth is greater than the device thickness, eliminating the complications resulting from progressive curing of epoxies at different depths. Another possibility was to change the epoxy being used since the photochemistry of the epoxy and the photoinitiator also affect the curing process.

To test this, fibers were dip-coated in different epoxies and cured using a 405-nm laser through the back connector, and then dipped in acetone to wash away uncured epoxy. It was seen that epoxy SLA 3-D printer resin, designed to cure at 405 nm UV produced pillars that were consistently seen to be straight, perpendicular to the fiber surface, and with flat tops, satisfying our most important requirement. This is seen in Figure 4.13.

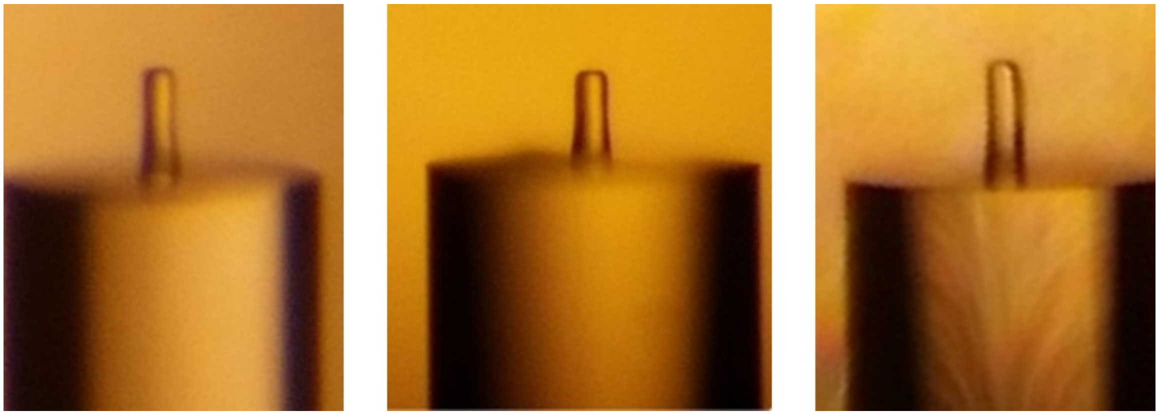

Figure 4.13: Photographs of straight pillars obtained using 405-nm curing and multiple samples demonstrate repeatability of the process. Fiber diameter is 125 μm, and pillar diameter is 9 μm.

This experiment confirmed that it was possible to fabricate epoxy waveguides with flat top surfaces by selective curing of UV sensitive epoxies, thus overcoming our biggest challenge. This waveguide structure can be incorporated into either bare fiber devices or fiber-ferrule assemblies as described above. Further, since the waveguide is self-aligned, this fabrication method can easily be extended to fiber bundles as well. Future work shall include complete characterization—optical and acoustic performance—of the devices fabricated with the waveguide and a cladding surrounding the waveguide with the requisite refractive index difference between the two materials for single-mode operation (about 0.006, calculated theoretically and confirmed via simulations), as well as dielectric mirrors for improved reflectivity.

4.2 Encapsulated Polymer Waveguide Device

4.2.1 Fabrication

In the previous section, we have presented a method to achieve high quality factor FP resonators by creating straight, self-aligned polymer waveguides on fiber substrates[66]. Having established the feasibility of creating these polymer waveguides, the next task was to fabricate a device with these straight polymer waveguides and complete the optical characterization to quantify the improvement in optical Q-factor that could be achieved with including the waveguide within the resonator structure. In this section, we use this method to fabricate and characterize waveguided FP resonators for ultrasound detection, demonstrating the improvement of waveguided FP resonators over those without waveguides. Optical characterization results from both devices are presented, highlighting the improved Q-factor in the waveguided case, which would in turn lead to improved acoustic sensitivity.

Simulation studies presented in Chapter 3 highlight the importance of having flat and parallel mirrors, and also the importance of having the pillar height be exactly equal to the cavity length. To achieve this, the devices described in this paper were constructed between the FC-PC connectors of two SM fibers, by holding them together in perfect alignment using a ceramic ferrule sleeve. This design helped us understand the optical behavior of waveguided fiber FP devices, but do not allow for acoustic sensing as the device is encapsulated in between the two fiber connectors. In the next chapter, a modification of this design is presented which allows us to characterize both optical and acoustic performance.

To fabricate the devices with waveguide, the following steps were followed:

1. 30 nm gold layer was evaporated on the FC ends of two FC/APC - FC/PC 125/250/900 um single mode patch cords (Precision Fiber Products, Inc.) to serve as the two mirrors of the resonator.

2. A viewing hole of about 1.5 mm diameter was drilled through the middle of a ceramic fiber optic mating sleeve (Precision Fiber Products, Inc.) to provide access for imaging and fabrication.

3. The gold-coated FC connectors were inserted into the sleeves, moving incrementally until the desired separation (30 μm) was achieved, as seen in Figure 4.14(c). This was done by estimating the distance using the magnified image under the camera.

4. The optical spectrum for this air-gap device was then measured, and the distance verified from the Free Spectral Range.

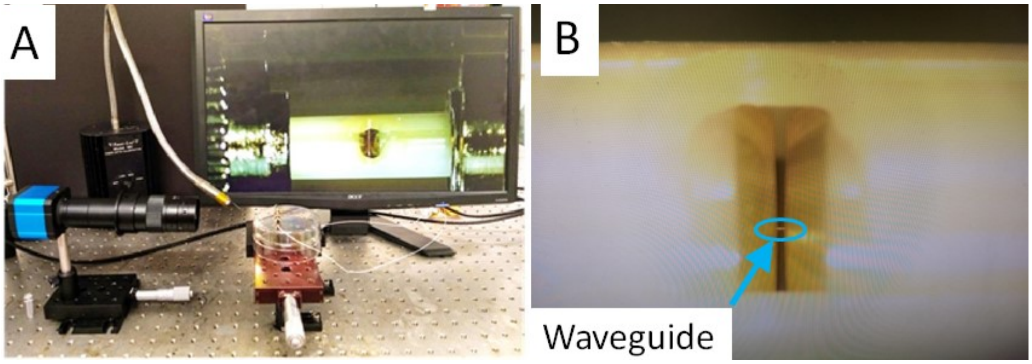

Figure 4.14: A-Setup used for fabrication showing fiber illuminator, digital camera with lens, and stage used for mounting the device, B Zoomed in view showing the presence of the waveguiding pillar in between the two connectors.

5. A high RI photopolymer (NOA 86; RI 1.56) was then dropped into the cavity via the viewing hole and cured via the fiber FC/APC connector using 405 nm UV laser, leading to selective curing of the portion of the polymer aligned with the cores of the two fibers.

6. The device was rinsed in acetone to dissolve and remove the uncured polymer, revealing a waveguide pillar in between the two fibers (Figure 4.14 (d)).

7. A photopolymer of lower RI (NOA 85) was then dropped into the cavity to surround the pillar, and cured using a UV lamp, resulting in a higher RI waveguide

embedded in low RI cladding. The spectrum was then measured using the schematic presented in Figure 4.15 (a), and is presented in Figure 4.16 (b), (d), and (f).

To fabricate the devices without waveguide, a similar process was followed, with the difference being that only the high RI polymer was used to fill the entire cavity. Curing was done using a UV lamp, resulting in a polymer Fabry-Perot cavity with no waveguide. The spectrum for this cavity was measured using the schematic presented in Figure 4.15 (a), and is presented in Figure 4.16 (a), (c), and (e). To measure the characteristic spectrum of the device, the instrumentation setup used in reflection and transmission mode are as presented in the schematic in Figure 4.15 (a) and (b) respectively.

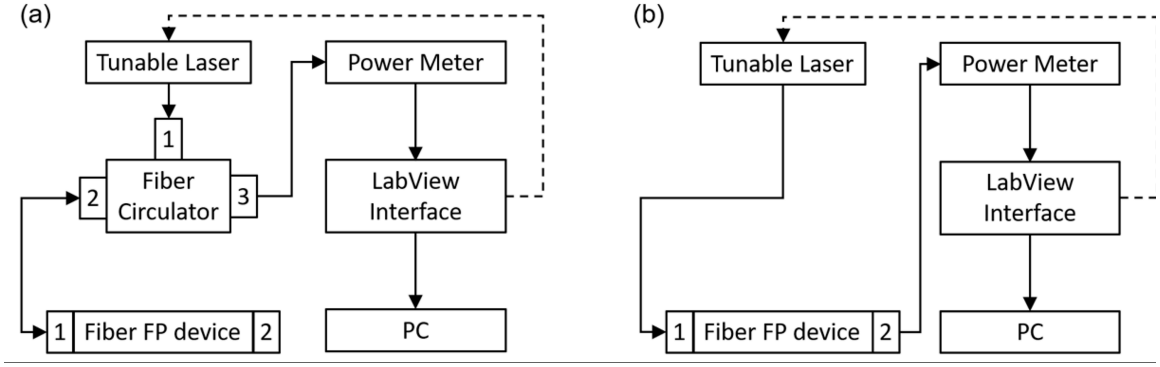

Figure 4.15: Schematic of system used to capture the spectrum of the device based on (a) reflection and (b) transmission measurements.

4.2.2 Characterization

Optical Characteristics - comparison

A tunable NIR laser (1510 - 1640 nm) was used as the source. Power measurements were made via a LabVIEW Interface, which also controls the power and wavelength of the laser for each acquisition. Using the fabrication method described above, three devices each with and without polymer waveguides were fabricated whose characteristic curves are presented in Figure 4.16). The Q-factors of devices with waveguide are in the range of 2500-3000, a marked improvement from the range of 800-1000 observed in the devices of similar thickness fabricated without a waveguide.

Temperature Effects

The sharper resonances seen in the case of the waveguided devices were expected due to reduced diffraction losses, but the apparent asymmetry was not. To confirm the asymmetrical optical spectra of the device, the characteristic curve for a waveguided device was recorded again at various input powers of the tunable laser. The results are as seen in Figure 4.17)

From these results, it is clear that the asymmetry observed is significant at higher powers of the tunable laser. We hypothesized that the apparent asymmetry at higher powers was due to higher temperatures caused by the increased absorption of the metallic mirrors at resonant wavelengths. To test this hypothesis, it was necessary to confirm that (i) there is significant absorption at the resonant peaks, and (ii) the spectrum shifts to the left at increased temperatures. These factors were verified by two additional experiments. Since scattering and diffraction losses are negligible in this case, the absorption is measured by subtracting reflection and transmission power from the input power. Figure 4.18 shows the normalized reflected, transmitted, and absorbed powers for 0.5mW input. This shows that a large fraction of the power is absorbed, and therefore temperature rise due to absorption is expected to be significant.

Further, the spectra (reflection and transmission) from the device at low input power of 0.5 mW were compared to those obtained from a simulated device (Rsoft - Photonics Design Suite), to confirm that the magnitude of absorption at wavelengths corresponding to the resonance peaks and true shape of resonance were similar to

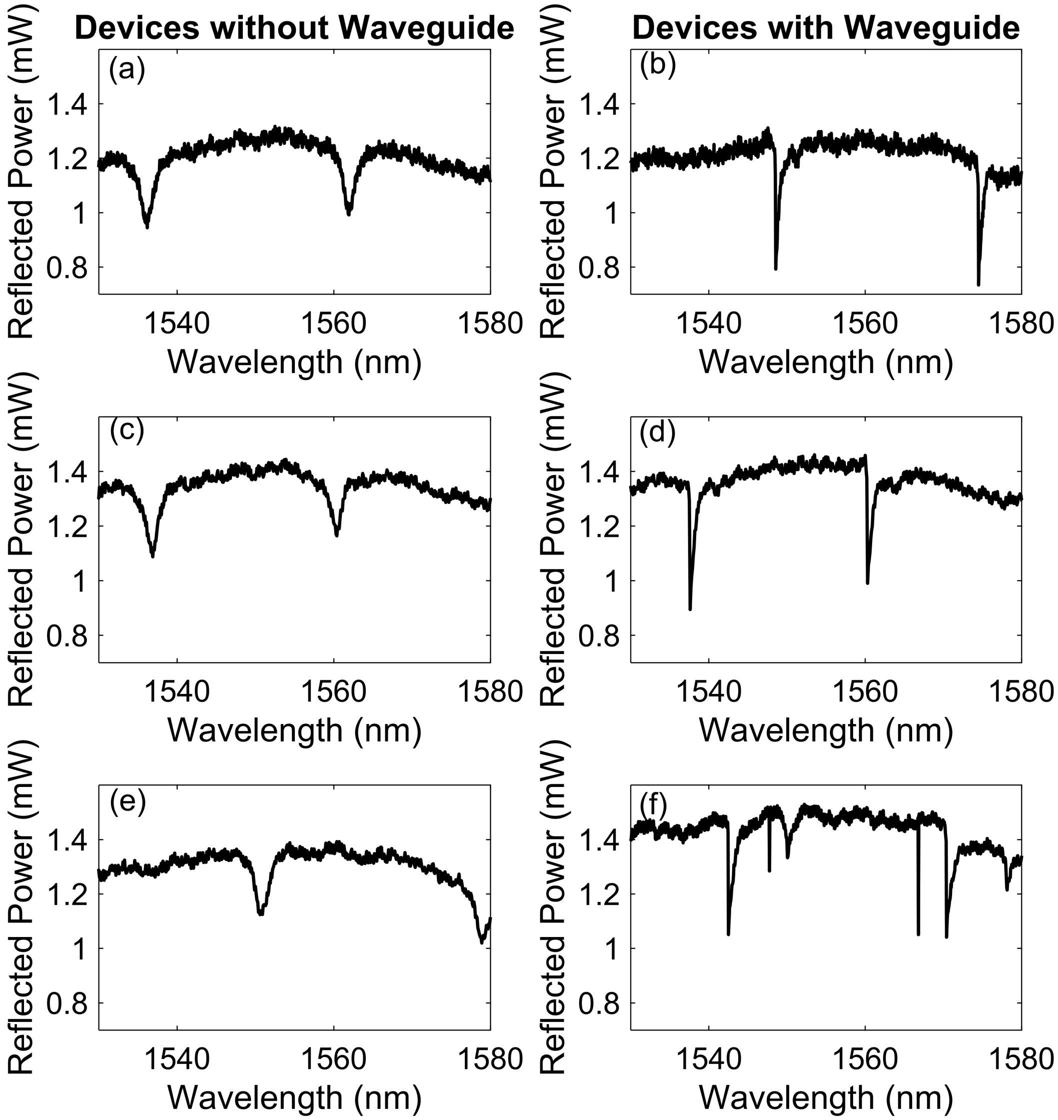

Figure 4.16: Characteristic curves measured from devices fabricated without waveguide (a), (c), and (e) show lower contrast and Q-factor as compared to devices with waveguide (b), (d), and (f).

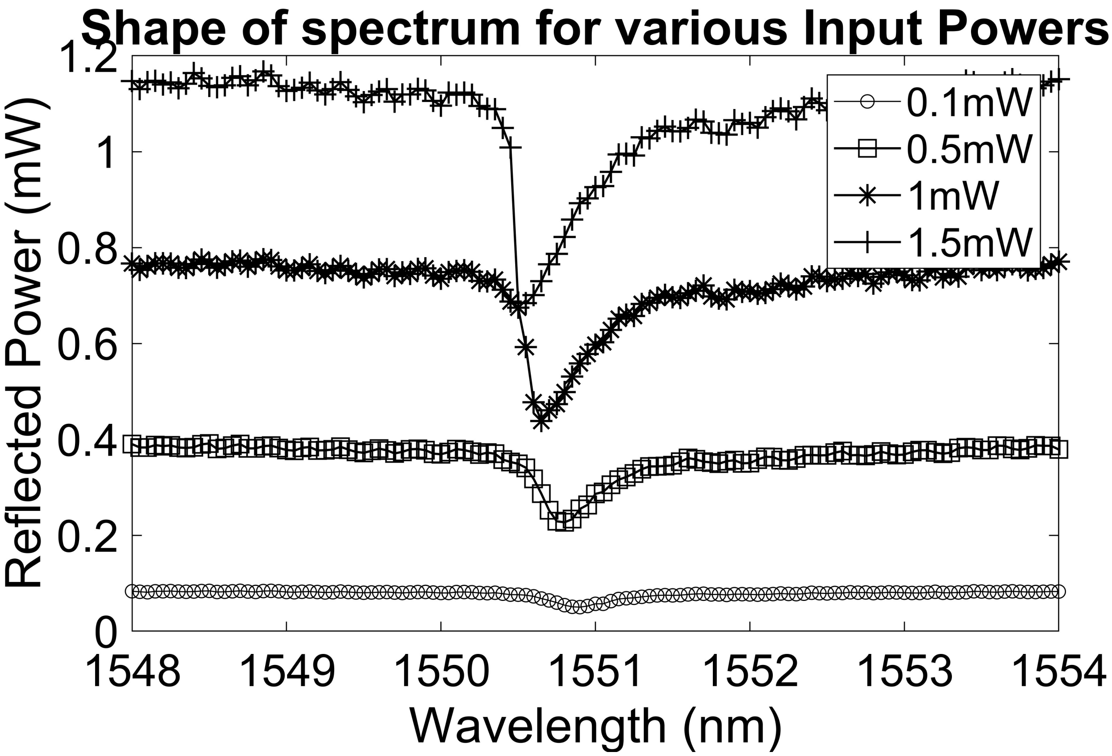

Figure 4.17: Graph comparing resonance shapes for various input powers.

expected values. As seen from Figure 4.18(a) and (b), the characteristic spectrum of the physical device is seen to closely follow that of the simulated device. Measurements indicate the simulated device has a Q-factor of 1552.75 and a Finesse of 25.91, and these numbers are closely matched by the physical device at Q-factor of 1550.30 and Finesse of 22.60.

Next, to isolate the effect of temperature rise on the spectrum, the device was placed in a thermally isolated container and the reflection spectrum measured at low input power (0.5 mW). This measurement was then repeated for increasing temperatures, and the direction of shift of the spectrum was observed. The results, pictured in Figure 4.19), confirm that the spectrum shifts to the left with increased temperatures. This is also validated below using a theoretical model. The amount of shift with temperature was captured using the best fit of this data, as seen in Figure 4.19)

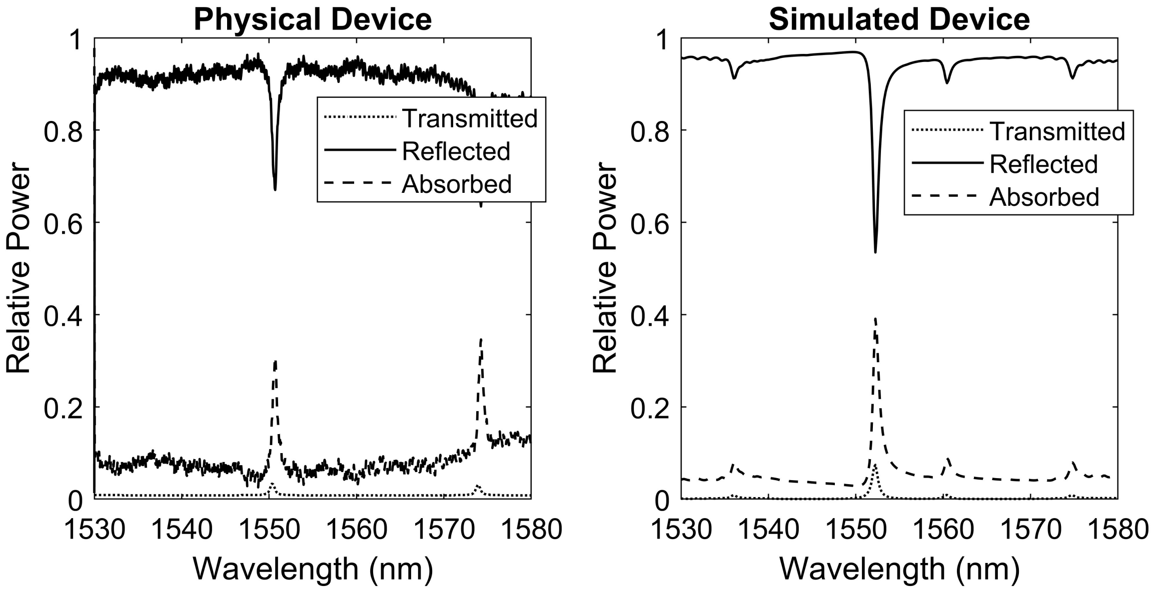

Figure 4.18: Normalized reflected, transmitted, and absorbed powers for 0.5mW input for (a) the physical device and (b) the simulated device.

(b), and is used as the value γ in the theoretical model below.

To better understand the role that temperature rise plays in observed spectral asymmetry, a theoretical model was developed based on the basic model described in Figure 4.20 (a). The outer cylinder represents the ferrule sleeve of 2mm diameter, and the inner cylinder represents the volume of the functional device where the absorbed power is concentrated. With mirror diameters of 9 μm and a spacing of 30 μm between them, the device behaves as a point source of heat with a temperature Tdevice. The heat generated by the mirrors is then conducted to the surface of the ferrule which is at a temperature Tsurface. Ideal heat removal is assumed at the surface of the ferrule.

Therefore, the temperature difference driving conduction of heat to the surface is

$$T_{diff} = T_{device} - T_{Surface}. \tag{4.4}$$

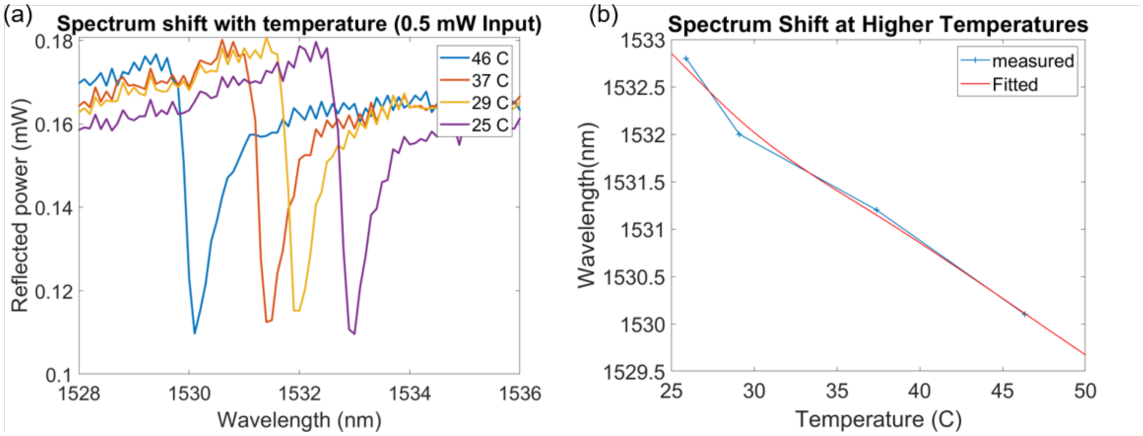

Figure 4.19: Graph comparing resonance shapes for various input temperatures.

The rate of change of temperature can therefore be described as

$$\frac{\partial T_{diff}}{\partial t} = A\alpha - BT_{diff}, \tag{4.5}$$

where $\alpha = \frac{1}{C_{eff}}$, C_{eff} being the heat capacity in Joule/K, and $\beta = \frac{KS}{RC_{eff}}$, where K is the heat conductivity in $Wm^{-1}K^{-1}$, S is the surface area of the ferrule through which the heat is lost, and R is the ferrule radius - the distance over which the temperature difference is T_{diff}. A is the power dissipated in the mirrors and is assumed to be temperature dependent due to the temperature dependence of the resonance curve.

The temperature rise due to absorption, and the related shift of the spectrum can be understood using Figure 4.20 (b). As seen here, the wavelengths corresponding to maximum reflection (and consequently minimum absorption) do not shift as there is no significant temperature rise. As the reflection decreases, absorption increases, and consequently heat is generated. Thus, at wavelengths corresponding to reduced reflection, there is a shift of the spectrum corresponding to the temperature

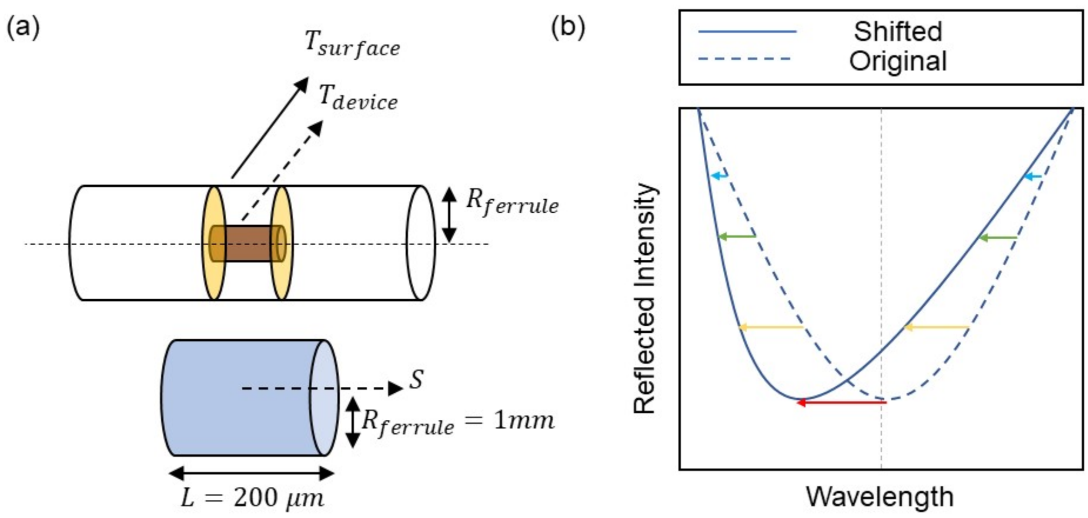

Figure 4.20: (a) Model used to describe temperature effects in the device and (b) expected spectral shift at resonant wavelengths due to temperature rise.

change. The maximum shift, denoted by the longest arrow, occurs at the wavelength corresponding to the resonance peak.

At each wavelength, since there is constant heat generation due to absorption and heat loss due to conduction to the ferrule surface, the steady state wavelength shift can be obtained by setting the rate of temperature change as zero, or $\frac{\partial T_{diff}}{\partial t} = 0$. Thus, we solve for the case

$$\alpha A(\Delta\lambda + \lambda_{Laser}) = \beta T_{diff}, \tag{4.6}$$

where $A(\Delta\lambda+\lambda_{Laser})$ is the absorption at the shifted wavelength. The wavelength shift, in turn can be described by $\Delta\lambda = \gamma T_{diff}$, which yields

$$\alpha \frac{\gamma}{\beta} A(\Delta\lambda + \lambda_{Laser}) = \Delta\lambda, \tag{4.7}$$

This was solved graphically for $K = 1\ Wm^{-1}K^{-1}$, $C_{eff} = 0.0016 Joule/K$, $S = 1.25e - 6m^2$, $R = 1e - 3m$, $\gamma = 0.15nm/K$ at input power of 2 mW. As seen in Figure 4.21 , the results from theoretical model show a leftward shift due to

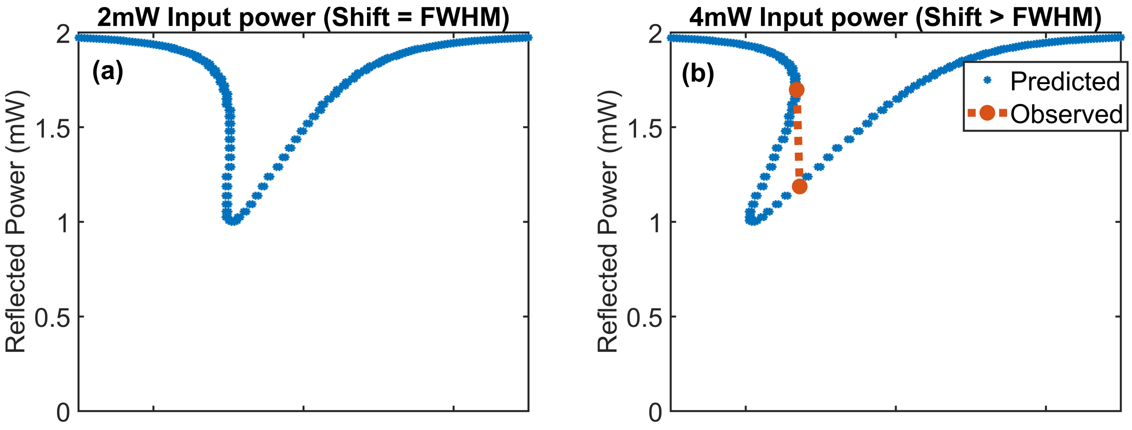

Figure 4.21: Results from theoretical model for wavelength shift due to absorption showing increased asymmetry with absorption.

absorption leading to observed asymmetrical reflection spectra as seen in experimental results, thus validating our hypothesis. Thus, a fair comparison between the performances of waveguided and non-waveguided devices would be at low powers, where the temperature induced shift is negligible. At higher power the model yields a region of three solutions and an instability causing a jump from one solution branch to another (see Figure 4.21(b)). In the measured reflection spectrum, obtained experimentally by wavelength scanning, this jump generates a vertical discontinuity.

Figure 4.22 demonstrates the drastic improvement with waveguide at 0.5 mW input power but using lower input power also results in reduced contrast. Dielectric mirrors would be a better choice as they offer much higher reflectivity, eliminating the problem of absorption induced shift and consequently improving the contrast. The predicted improvement in NEP would be twofold because of the increased reflectivity and the ability to drive the device at higher input powers.

The experiments described herein allowed accurate prediction of optical performance of the polymer-waveguided devices. In order to perform acoustic characterization, the device fabrication had to be altered to allow one face of the resonator to be open to the acoustic perturbation. The fabrication, as well as optical and acoustic

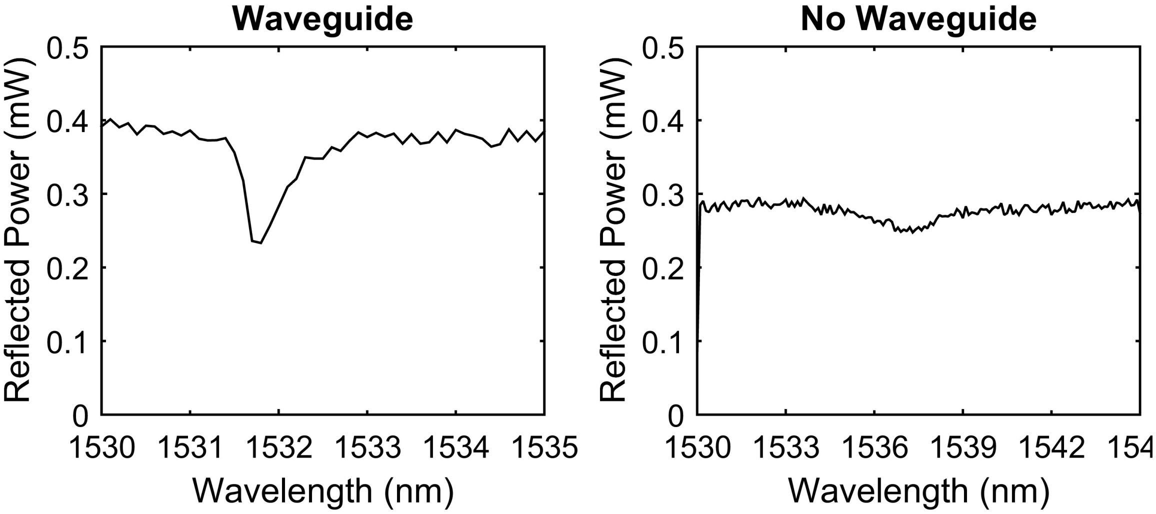

Figure 4.22: Results comparing waveguided and non-waveguided devices at low input power.

characterization of these devices is presented in the following chapter.

Chapter 5

Fiber Fabry-Perot Ultrasound Detectors with Polymer Waveguides for Improved Sensitivity

The content of this chapter has been submitted for review as a research article in the *IEEE Sensors* Journal.

5.1 Polymer Waveguides for Improved Sensitivity in Fiber Fabry-Perot Ultrasound Detectors

5.1.1 Methods

Fabrication

The devices described in this paper were constructed on the FC-PC connectors of Single Mode (SM) fibers held within ceramic ferrule sleeves with inner diameter 1.8

mm to ensure that the two mirrors of the resonator were exactly parallel to each other. To fabricate the devices with waveguides, the following steps were followed:

1. A 30 nm gold layer was evaporated on the FC end of a FC/APC - FC/PC 125/250/900 μm single mode patch cords (Precision Fiber Products, Inc.) to serve as the first mirror of the resonator.

2. An access window of about 1.5 mm diameter was drilled through the end of a ceramic fiber optic mating sleeve (Precision Fiber Products, Inc.) to provide access for imaging and fabrication.

3. The gold-coated FC connector was inserted into the sleeve, moving incrementally until the desired separation from the sleeve end (30 μm) was achieved, as seen in Figure 5.1. This was done by estimating the distance using a magnified image seen via a camera. A glass slide was coated with 30 nm of gold to serve as the second mirror of the resonator.

4. The ferrule-sleeve assembly was then placed on the glass slide such that the mirrors were parallel to each other and separated by the distance (about 30 μm) corresponding to the resonator length.

5. The optical spectrum for this air-cavity device was then measured, and the distance verified from the Free Spectral Range.

6. A high Refractive Index (RI) photopolymer (NOA 86; RI 1.56) was then injected into the cavity via the viewing hole and cured via the fiber FC/APC connector using 405 nm UV laser, leading to selective curing of the portion of the polymer aligned with the core of the fiber.

7. The device was rinsed in acetone to dissolve and remove the uncured polymer, revealing a waveguide pillar in between the two mirrors (Figure 5.1(b)).

8. A photopolymer of lower RI (NOA 85; RI 1.46) was then injected into the cavity to surround the pillar, and flood cured using a UV lamp, resulting in a higher RI waveguide embedded in low RI cladding (Figure 5.1 (c)).

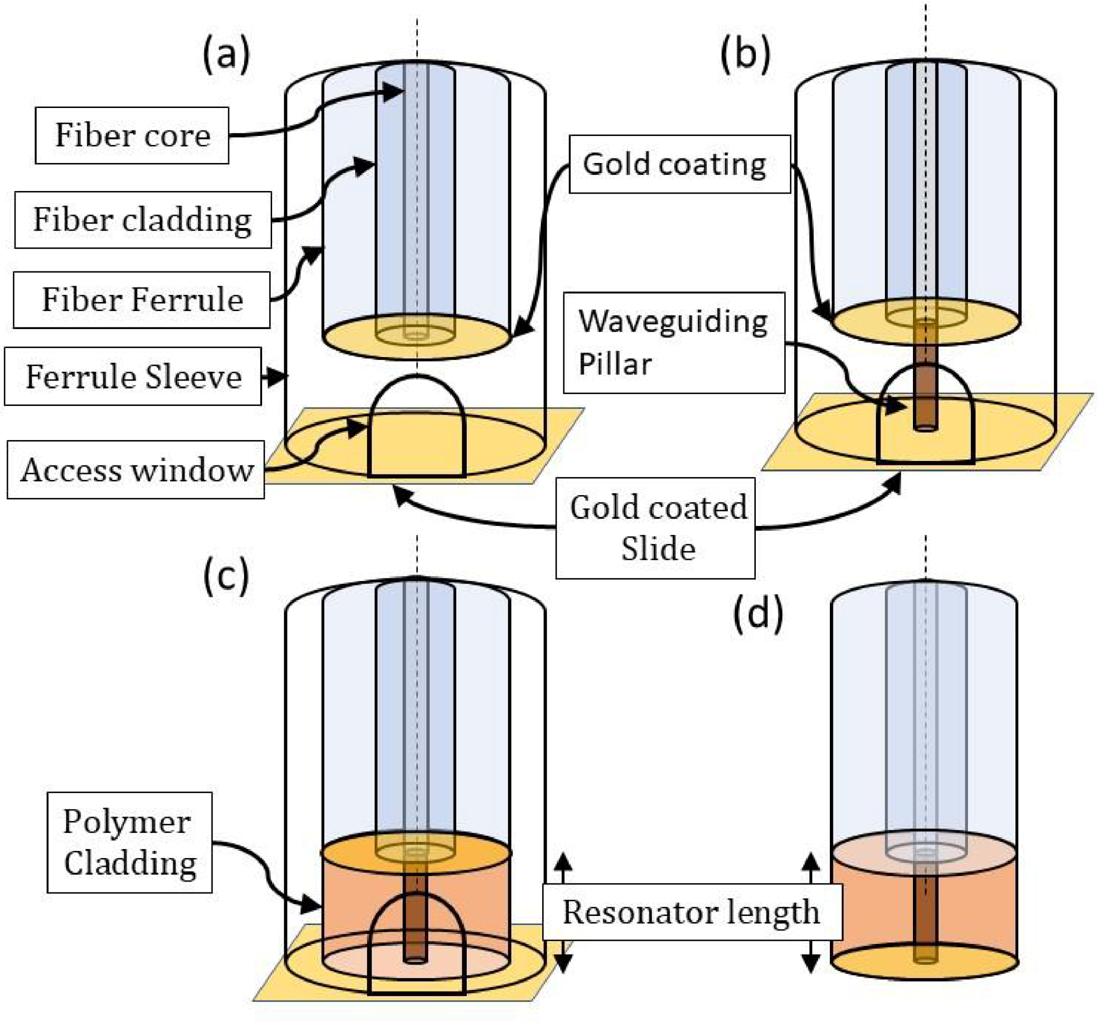

Figure 5.1: Illustration of the fabrication process. (a) Assembly of the fiber ferrule within the ferrule sleeve at the desired distance (b) Polymer waveguide created between the two mirrors by selective curing of higher RI epoxy (c) Cladding composed of lower RI epoxy surrounding the waveguiding core (d) Complete device

9. The spectrum was then measured using the schematic presented in Figure 5.3, and is presented in Figure 5.7(b), (d), and (f). A photograph of the device is presented in Figure 5.2.

10. To fabricate the devices without waveguide, a similar process was followed, with the difference being that only the high RI polymer was used to fill the entire cavity. Curing was done using a UV lamp, resulting in a polymer Fabry-Perot cavity with no waveguide. The spectrum for this cavity was measured using the schematic presented in Figure 5.3, and is presented in Figure 5.7(a), (c), and (e).

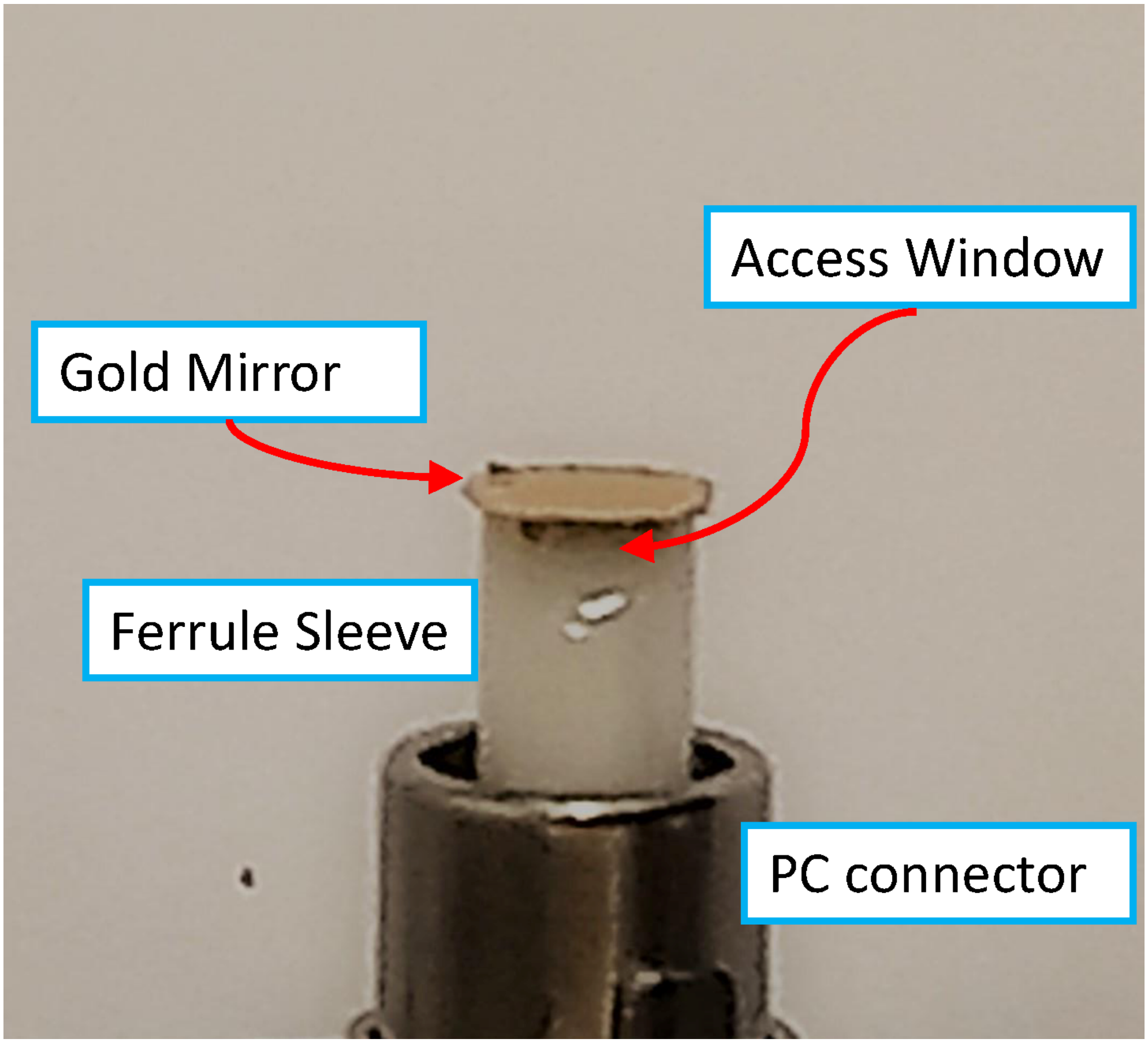

Figure 5.2: Photograph of the device built on the ferrule of a fiber connector.

Optical Characterization

To measure the interferometer transfer function (ITF) or characteristic curve of the device in reflection mode, the instrumentation used is presented in the schematic in Figure 5.3. A tunable NIR laser (1510 - 1640 nm, output power: 4 mW, HP 8168F, Agilent Technologies, Santa Clara, CA) was used as the source. This fiber coupled laser was then connected to the input port of an optical fiber circulator (6015-3-APC - Fiber Optic Circulator, 1525 - 1610 nm, SMF, FC/APC, Thorlabs Inc., Newton, NJ). The light then travels via bidirectional port 2 of the circulator to the device, from which the reflected light travels back into port 2 of the circulator where it is directed to output port 3, where it is read by a power meter (PM 100, Thorlabs Inc., Newton, NJ). Power measurements were made via a LabVIEW interface, which also controls the power and wavelength of the laser for each acquisition.

Using the fabrication method described above, devices each with and without polymer waveguides were fabricated at three different thicknesses. Their characteristic curves are presented in Figure 5.7. The Q-factors of devices with waveguide are in the range of 1500-2100, a marked improvement from the range of 400-800 observed in the devices of similar thickness fabricated without a waveguide.

Acoustic Characterization

For acoustic characterization of the devices, the instrumentation used is as pictured in 5.4. A single element piezoelectric piston transducer at 10 MHz (active area: 13 mm; focal length: 25.4 mm; V311, Olympus NDT Inc., Waltham, MA) was used as an acoustic source. The pulser/receiver (bandwidth: 50 MHz; DPR300, JSR Ultrasonics, Pittsford, NY) settings were adjusted to restrict the amplitude of the pulse to be below 75kPa. First, a calibration was performed by detecting the acoustic waveform using a 40-MHz hydrophone with a 20-dB preamplifier (aperture: 85 μm; HGL-0085/ AH-2010, Onda Corp., Sunnyvale, CA) to ascertain the true acoustic pressure ampli-

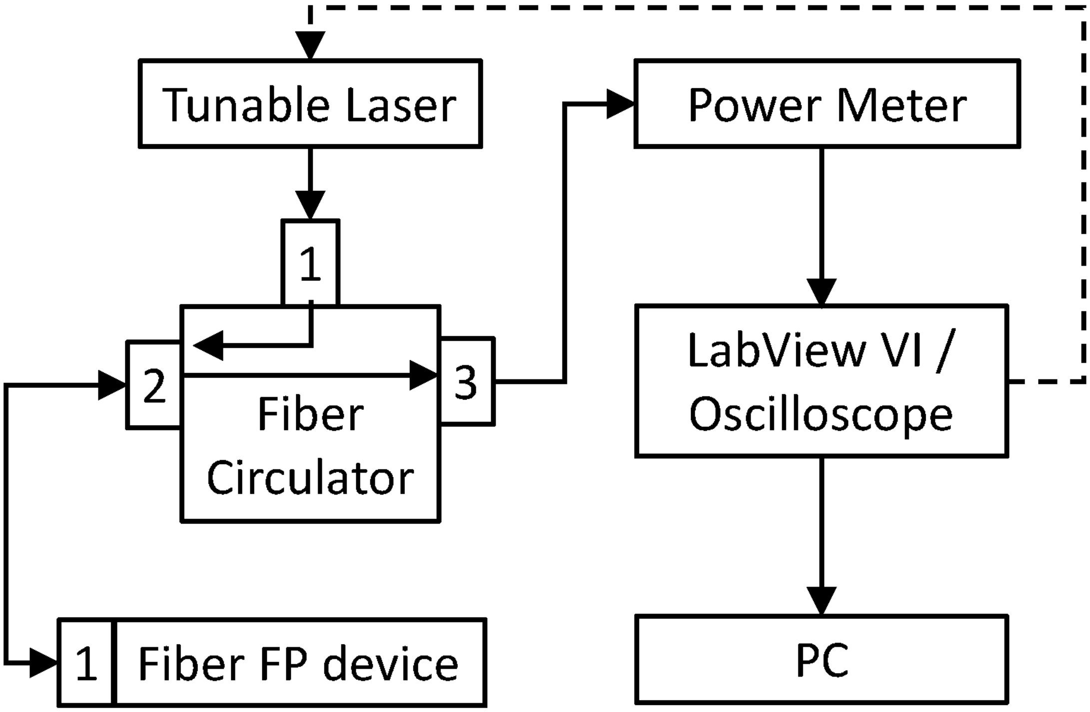

Figure 5.3: Schematic of the instrumentation setup used to acquire the Interferometer Transfer Function (ITF) for the device. Dotted lines represent control connections, whereas solid lines represent power/data.

tude.

Thereafter, the hydrophone was replaced by the fabricated device and the same acoustic signal was acquired. The wavelength of the CW NIR laser was tuned to the point of highest slope in the ITF, in order to obtain the highest sensitivity. The output of the fiber-optic circulator was fed to a high-speed photodetector. By equating the pk-pk voltage with the acoustic pressure amplitude ascertained in the calibration step using the hydrophone, the pressure corresponding to the noise (Noise Equivalent Pressure) was calculated. For this, the standard deviation of the noise over 2 μs immediately preceding the signal was used.

5.1.2 Results

This section describes the results of experiments conducted around the device. First, we present the results of simulations used to optimize the design of the resonator. Next, we present the results of the comparison of waveguided vs nonwaveguided simulated devices. Following this, a comparison of the optical characterization of the waveguided devices vs the non-waveguided devices is presented for the fabricated devices. Finally, we present the results of the acoustic characterization of the sensor in terms of its sensitivity and bandwidth.

Design Simulation for Optimization

To determine the design parameters of the device to be fabricated, the device was modeled on the RSoft Photonics Design Suite. Gold was selected for the initial design as the mirror material due to the ease of fabrication and satisfactory reflection at NIR wavelengths used for sensing (0.94 around 1550 nm). In the future, dielectric mirrors will be incorporated instead for higher reflection and consequently higher Q factors, as discussed later.

First, A simulation study was performed to determine the refractive indices of the

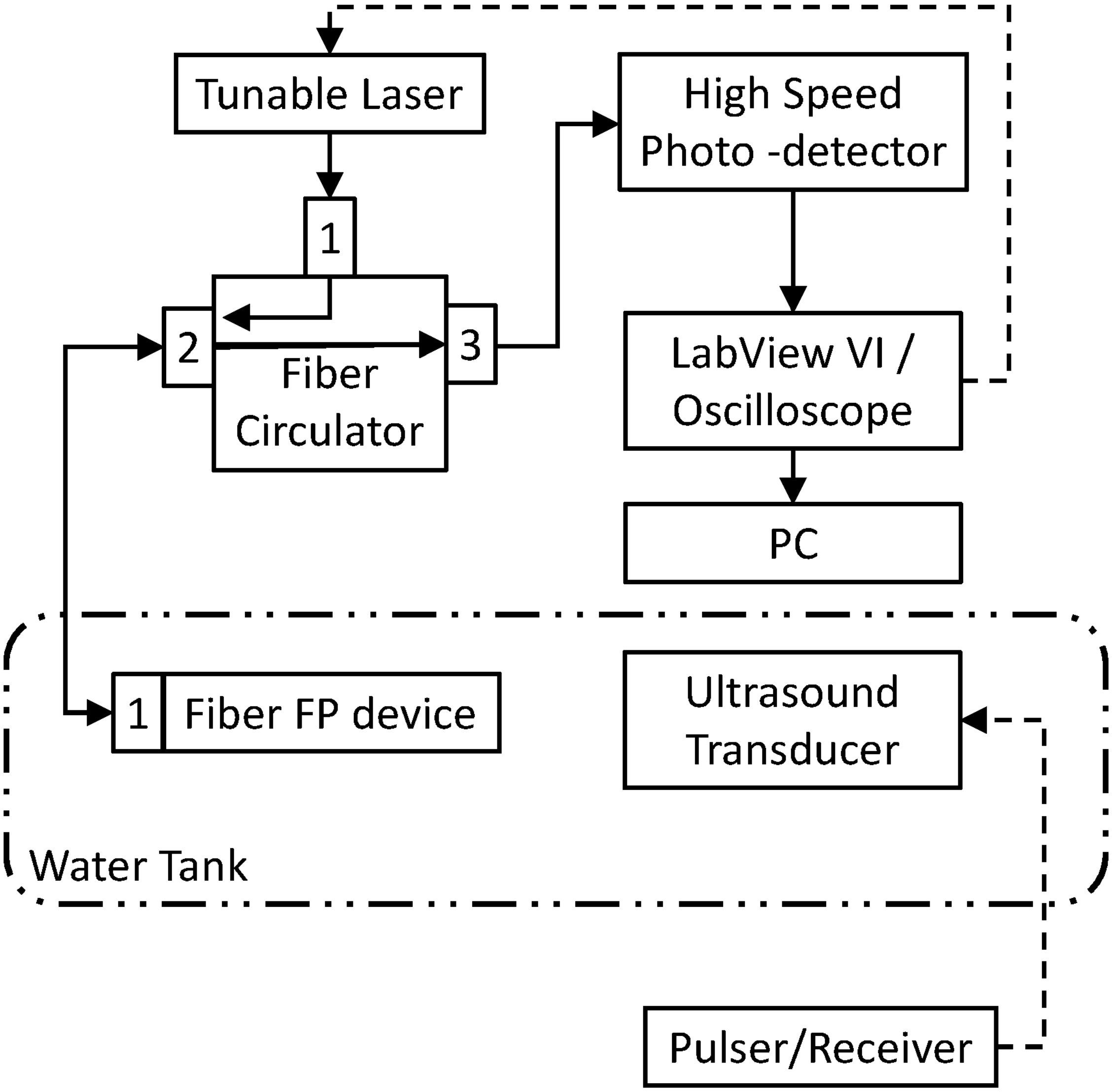

Figure 5.4: Schematic of the instrumentation setup used to perform acoustic characterization of the device. Ultrasound pulses are generated using a piston transducer, which is focused on a hydrophone during the calibration step, and then the fabricated device in place of the hydrophone in the measurement step. As was the case in Fig. 3, dotted lines represent control connections, whereas solid lines represent power/ data.

polymers used to fabricate the core and cladding of the resonator. For this, the refractive index difference between the two segments of the simulated resonator was reduced incrementally, and the Interferometer Transfer Function plotted. As pictured in Figure 5.5, it was seen that below a difference of 0.1, the Q-factor does not significantly improve. Thus, two polymers, NOA 86 and NOA 85, with refractive indices 1.56 and 1.46 respectively, were chosen for fabrication.

Similarly, another simulation was run to visualize the impact of mirror thickness on the optical performance. As shown in Figure 5.5, it was observed that Q-factor improves with thicker mirrors, but at the cost of visibility, and vice-versa upon increasing mirror thickness. An optimal mirror thickness of 30 nm was chosen for fabrication based on this tradeoff.

Optical Performance

Simulated Resonators

Once the design parameters were established, a simulation study was conducted using the refractive index difference of 0.1 and a gold mirror thickness of 30 nm to estimate the Q-factor and finesse for devices with waveguide and compare them to those without waveguide. This study was performed for three thicknesses – 30 μm, 25 μm, and 18 μm. The Free Spectral Range (FSR) of the ITF was used to confirm the device thickness in each case. Refractive indices of the sections corresponding to the core and cladding of the resonator were set to 1.55 and 1.46 respectively to match the RI of polymers used to fabricate devices subsequently.

The Interferometer Transfer Functions for each of these cases is presented in Figure 5.6. The corresponding finesse and Q-factor for each simulated device is as shown in Table II. As expected, the Q-factor and finesse values for the devices simulated with waveguide are higher than the corresponding values for devices without waveguides.

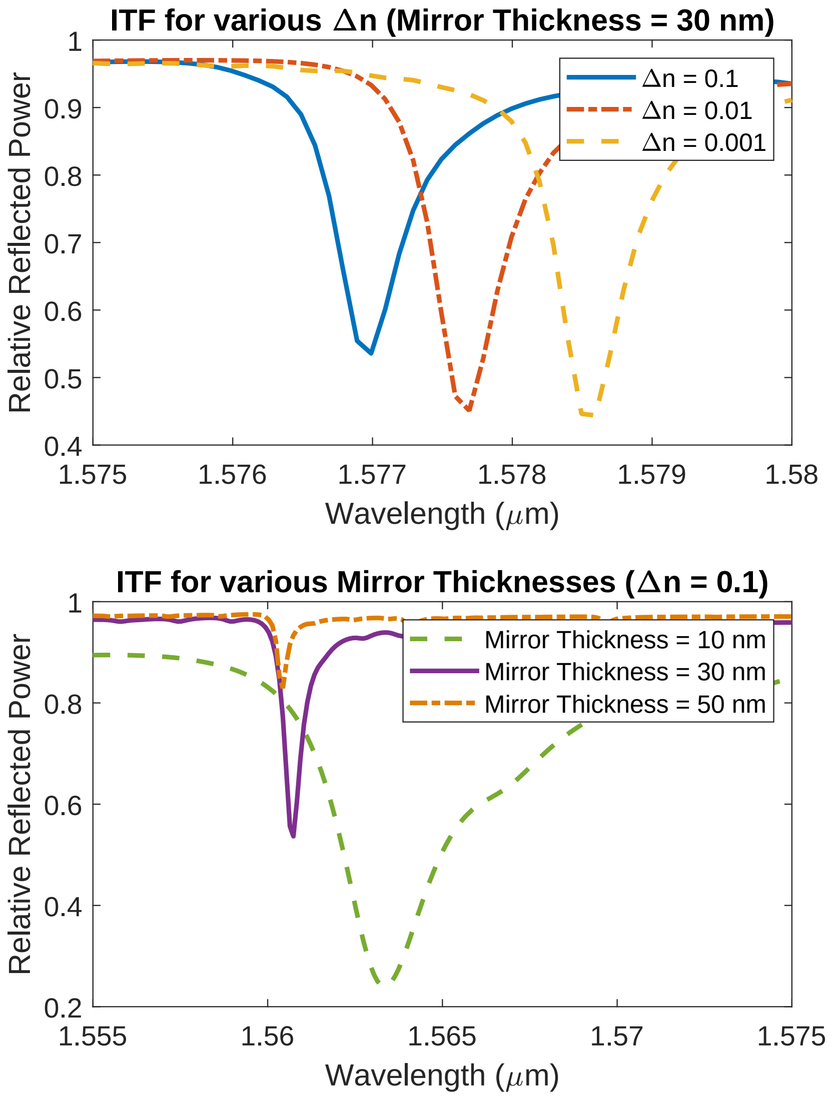

Figure 5.5: Simulation results employed to guide resonator design. Top: Refractive index difference between polymers used to create the core and cladding of the waveguided design does not impact the Q-factor as long as it is below 0.1. Bottom: Based on the trade-off between visibility and Q-factor of the resonator upon varying mirror thickness, a 30 nm mirror thickness was chosen for fabrication.

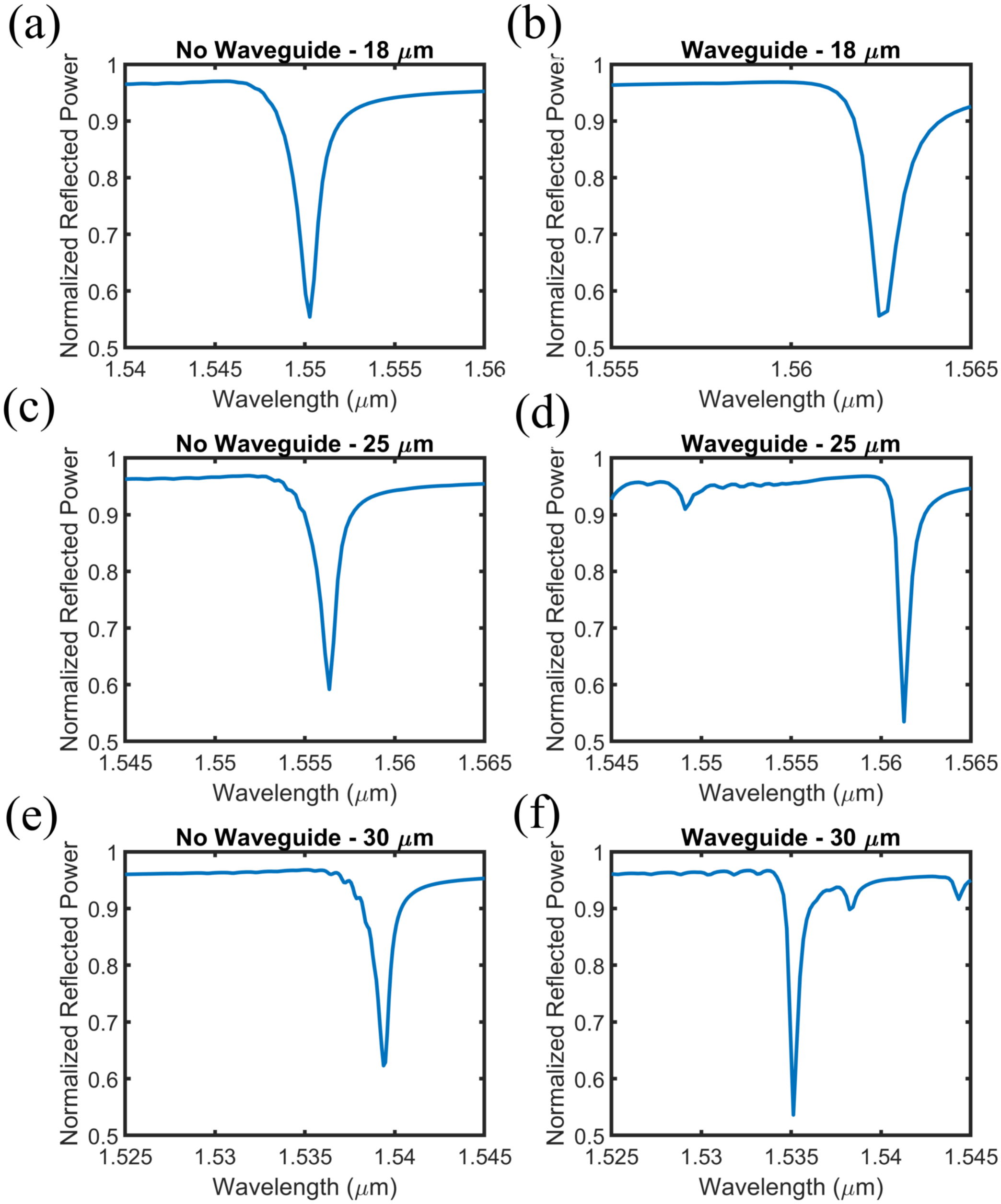

Figure 5.6: Interferometer Transfer Functions captured in reflection mode for simulated devices with waveguide and without waveguide for three different thicknesses. In each case, the devices with waveguide show a sharper resonance with a higher Q-factor than the devices without waveguide.

No Waveguide			Waveguide		
Size(μm)	Q-factor	Finesse	Size(μm)	Q-factor	Finesse
18	1032.75	31.49	18	2083.17	58.93
25	1523.69	31.32	25	2550.9	49.01
30	1924.18	34.03	30	4386.55	73.05

Table 5.1: Metrics for Simulated Devices

Fabricated Resonators

Following the simulation study, the devices with the same mirror thickness, refractive index difference between core and cladding, and the same three thicknesses as the simulated devices were also fabricated using the process presented in the methods section. The results from optical characterization of the fabricated devices with and without waveguide are presented in Figure 5.7.

No Waveguide			Waveguide		
Size(μm)	Q-factor	Finesse	Size(μm)	Q-factor	Finesse
18	382.01	11.87	18	1913.75	54.64
22	518.83	10.89	25	1557.25	33.73
30	767.50	14.71	30	2077.80	33.85

Table 5.2: Metrics for Fabricated Devices

The corresponding finesse and Q-factor for each simulated device is as shown in Table II. As expected, the Q-factor and finesse values in each case are seen to be higher in the presence of the waveguide due to the reduction in diffraction losses within the resonator. In addition to affecting the sharpness of the resonances, optical losses also affect the fringe visibility. These losses may be due to reflection at the input interface, losses in the optical medium, or recoupling losses into the fiber. The waveguide addresses the third mechanism of loss. The difference in finesse and fringe visibility between simulated and fabricated devices can be explained by the absorption in the cavity medium.

A high contrast as well as Q-factor are desirable in order to have high sensitivity without saturating the sensor. Fringe visibility decreases with increase in cavity length for devices without waveguide due to recoupling losses. Since waveguides address this issue, the 30 μm waveguided device was chosen for acoustic characterization. It provides sufficiently high Q-factor for high sensitivity ultrasound detection while still providing enough optical contrast to stay out of saturation.

Acoustic Performance

The 30 μm waveguided fiber-optic ultrasound sensor was then characterized for its acoustic sensitivity and bandwidth and compared against the performance of a commercial piezoelectric hydrophone of size 85 μm. For this, the setup as described in Figure 5.4 was used. First, a focused single-element ultrasound transducer was set up as shown in Figure 5.4, and a piezoelectric hydrophone was used to detect the resultant acoustic pulse, as shown in Figure 5.8(a).The signal was then passed through a 25 MHz low-pass filter, as seen in Figure 5.8(b). Excitation to the transducer was kept low to maintain the pressure amplitude under saturation for the detector. From the hydrophone calibration data, the acoustic pressure corresponding to this pk-pk amplitude was confirmed to be 59 kPa. The standard deviation of the noise collected over 2 μs preceding the signal peak was then calculated and used to estimate the Noise Equivalent Pressure of the hydrophone. This was found to be 5.6 kPa over the 25 MHz measurement bandwidth, seen in Figure 5.8(c).

Next, the hydrophone was replaced with the fabricated device and the measurement was repeated using the same acoustic source. The signals measured from the device before and after 25 MHz low-pass filtering are as seen in Figure 5.8(c) and Figure 5.8(d), respectively. By equating the pk-pk device signal to the pressure amplitude of 59 kPa, the device NEP was calculated. Over the same 25 MHz bandwidth (Figure 5.8(e)), the device shows a noise equivalent pressure of only 350 Pa, implying a 16-fold improvement in acoustic sensitivity compared to the hydrophone.

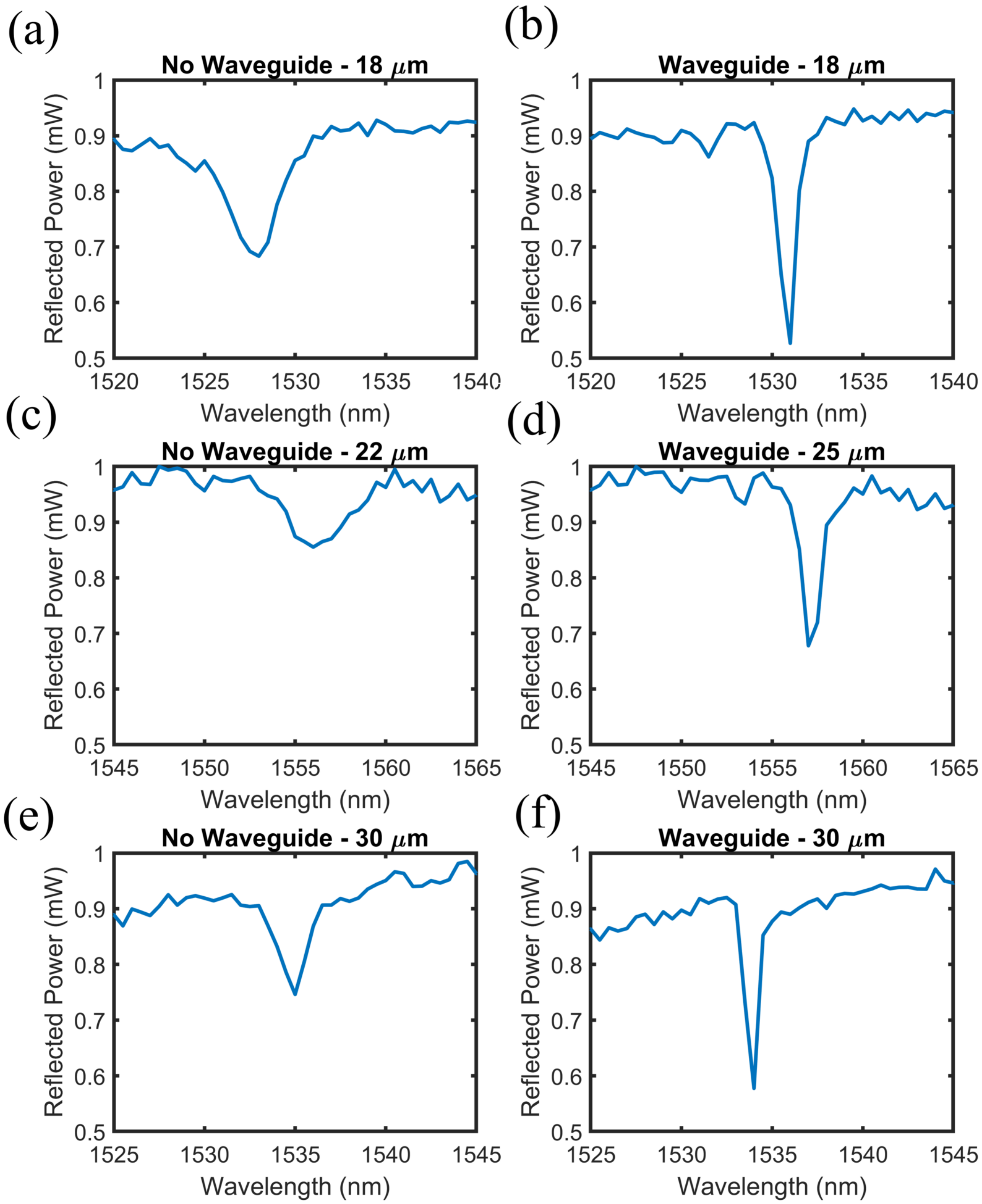

Figure 5.7: Interferometer Transfer Functions captured in reflection mode for fabricated devices with waveguide and without waveguide for three different thicknesses. In each case, the devices with waveguide show a sharper resonance with a higher Q-factor than the devices without waveguide.

To better characterize the bandwidth, and observe changes in bandwidth with device thickness, a similar experiment was conducted using a broadband acoustic source. To create this broadband acoustic source, a 355 nm UV laser was used to illuminate a glass plate coated with 5 μm of Polyimide. As the polyimide absorbs the UV light, it undergoes thermoelastic expansion, generating a broadband acoustic pulse by the photoacoustic effect. This photoacoustic pulse was then detected using the fabricated devices. The frequency spectrum of the signals detected using the 18 μm, 25 μm, and 30 μm thick devices was then calculated. As seen in Figure 5.9, the thinner the device, the broader is its detection bandwidth.

5.1.3 Discussion

This design employs a self-aligned polymer waveguide to arrest diffraction losses within the cavity, thus improving the optical Q-factor and acoustic sensitivity of the device. The sensitivity offered by all-optical technology at this scale far surpasses that of piezoelectric devices. As seen in the results presented in Figure 5.8, all-optical detection offers a 16 times higher sensitivity in a 9 times smaller active detection area (9 μm optical core as opposed to 85 μm piezoelectric element.)

The current device has an active sensing region of only 9 μm but an overall dimeter of 2 mm due to the ferrule – ferrule-sleeve assembly. Further, a multimode fiber would be required to couple enough light for illumination in order to perform photoacoustic measurements. To combine multimode illumination with single-mode detection, a dual-clad fiber design can be employed. This would allow integration of multimode illumination and single mode detection into a single fiber of 150 μm diameter. In order to allow these illumination wavelengths to pass through the resonator and into the region of interest, gold mirrors will have to be replaced with dielectric mirrors. Di-

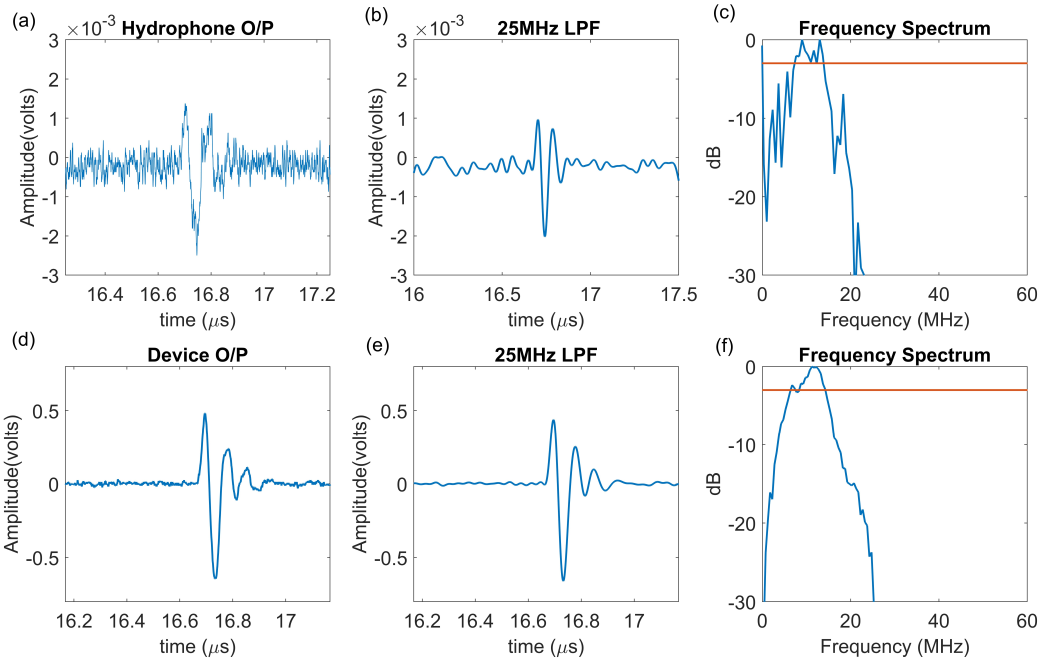

Figure 5.8: Response recorded by the hydrophone before (a) and after (b) 25MHz low-pass filter and the corresponding frequency spectrum (c), followed by the signal recorded by the fabricated device before(c) and after (e) 25 MHz low-pass filter and the corresponding frequency spectrum (f) for the same acoustic excitation. Over the same 25 MHz bandwidth (Fig. 8(e)), the device shows a noise equivalent pressure of only 350 Pa, implying a 16-fold improvement in acoustic sensitivity compared to the hydrophone.

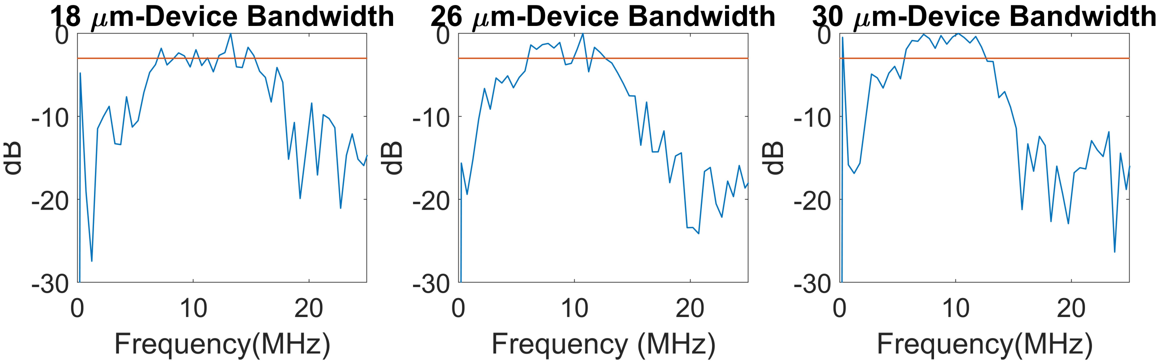

Figure 5.9: Frequency response from devices of three different thicknesses to a broadband photoacoustic source. It is observed that an 18 μm device has broader detection bandwidth, which then decreases as the thickness approaches 30 μm.

electric mirrors, while being transparent to lower wavelengths, offer very high (>99%) reflectivity at NIR wavelengths used for sensing, which will help to improve the Q-factor of the detectors. Further, the tip of the device can be coated with polyimide to allow for optical ultrasound generation by thermoelastic expansion. Thus, both all-optical ultrasound and photoacoustic sensing functions can be integrated into a single fiber of about 150 μm diameter.

The NEP of the device reported here - 350 Pa - can be further improved by optimizing both the device materials, as well as the electronics used for detection. In particular, incorporating dielectric mirrors into the design can dramatically improve the NEP. To support this claim, simulation studies were conducted on models incorporating the waveguide as well as dielectric mirrors of varying reflectivity.

The values of Q-factor versus reflectivity are as seen in table III above. For the same RI difference between core and cladding (0.1) and the same device thickness (30 μm) as the devices presented in this paper, the Q-factor was seen to improve significantly with the use of dielectric mirrors. The reflectivity could be improved even further by further increasing the mirror reflectivities, until the losses in the mir-

Mirror	Reflectivity	Q-factor
4 bilayer dielectric	0.8990	1,962.62
30 nm Gold	0.9445	4,386.55
5 bilayer dielectric	0.9725	7,781.97
6 bilayer dielectric	0.9855	9,227.47
7 bilayer dielectric	0.9945	17,429.25
8 bilayer dielectric	0.9979	78,432.13

Table 5.3: Reflectivity Vs Q-factor

rors become negligible compared to absorption losses within the polymer medium, at which point the improvement in Q-factor will likely saturate. Therefore, to improve the device signal-to-noise ratio, future work will include investigating NIR sources and photodetectors that can be operated at higher powers, as well as the use of dielectric mirrors to further improve the resonator Q-factor.

5.2 Complete Photoacoustic Probe

The all-optical ultrasound detector can be combined with a second fiber for excitation to create a complete all-optical probe. This second fiber can provide both photoacoustic excitation via direct illumination, as well as ultrasound exitation by thermoelastic ultrasound generation(TUG). To generate ultrasound pulses, thin films of highly absorptive materials can be made to absorb appropriate wavelengths to generate a thermoelastic wave. The temporal characteristics of this wave correspond to those of the optical pulse absorbed. Several materials have been developed for this purpose including black dyes[71][72], Gold nanostructures[73], metal thin films[74][75][76], and carbon nanotube composites[77]. Since the detection mechanism is also optical, it is important to chose wavelengths of light for generating TUG that are sufficiently lower,e.g UV wavelengths. Thus, an entirely optical probe for both generation and detection of US/PA waves can be created.

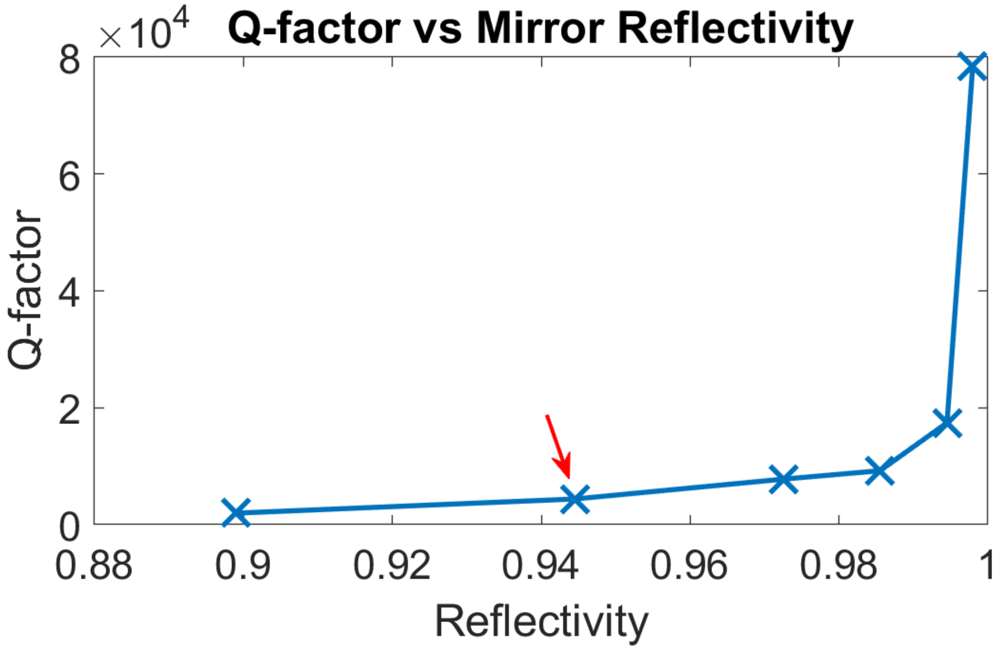

Figure 5.10: Simulation results showing increase in Q-factor with increasing mirror reflectivity. The arrow indicates the reflectivity of the gold mirrors used in devices presented in this paper, while the other data points are from dielectric mirrors stacks with 4, 5,6,7 and 8 bilayers for increasing reflectivity.

This all-optical probe can be created in one of two configurations. In the first, depicted in Figure 5.11, the two fibers are held together side by side within external tubing. The second configuration, depicted in Figure 5.12 is using a double-clad fiber. This type of fiber functions as a single mode at NIR wavelengths used for detection, and as a multimode fiber at lower wavelengths used for excitation. The resonator can be fabricated on top of the absorptive layer deposited for TUG. Thus, both excitation and detection can be combined into a single fiber, bringing down the diameter of the overall probe significantly.

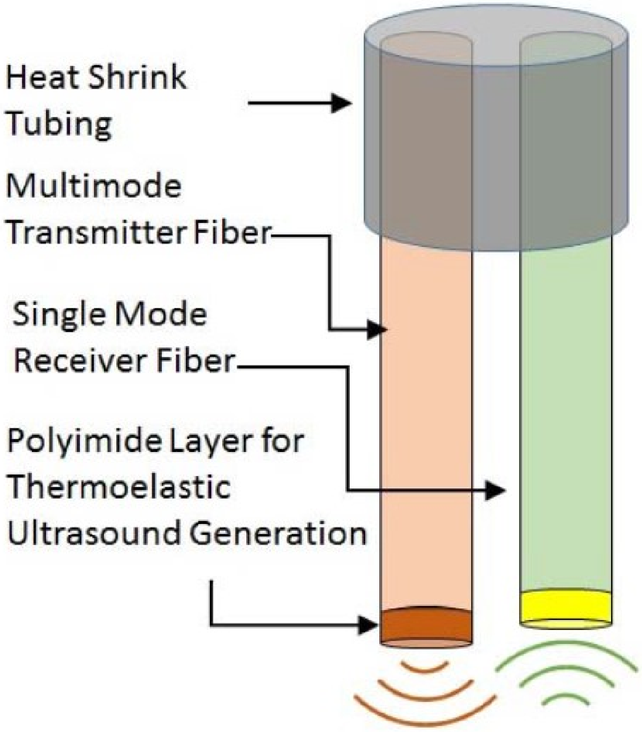

Figure 5.11: Transducer configuration 1

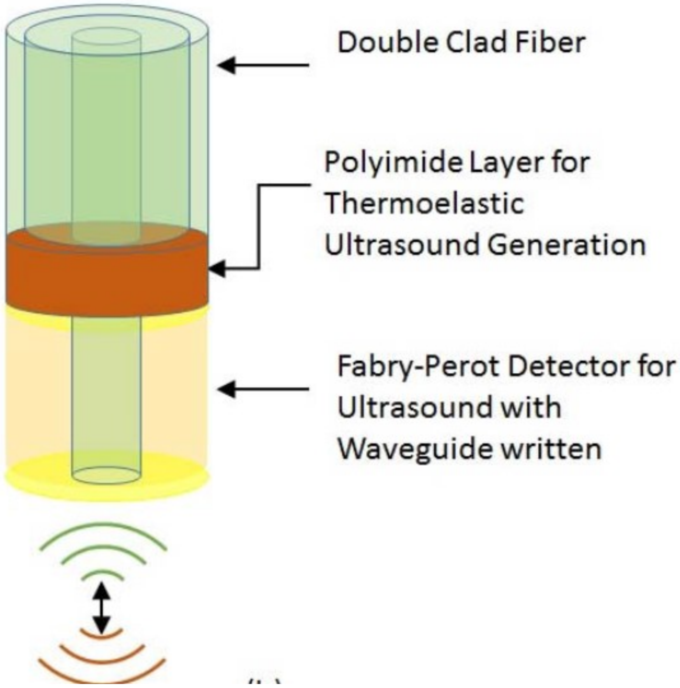

Figure 5.12: Transducer Configuration 2

Chapter 6

Conclusions and Future Work

This chapter presents the plans for future work on the single-element photoacousic probe, as well as models that can be created and used to test this device in-virto and in-vivo.

6.1 Sensing Guidewire

As described in the previous chapter, both illumination and excitation mechanisms, for both ultrasound as well as photoacoustic sensing modalities, can be fabricated on a single fiber of about 250 μm diameter. This will enable embedding the fiber into a standard guidewire (0.014"). This will require the following modifications to the design demonstrated in previous chapters:

1. Changing the gold mirrors to dielectric mirrors to allow visible and near infrared light transmission. The mirrors will have high (>80%) transmission in the range of 400 – 950 nm, and high reflectivity (>98%) in the range of 1520-1580nm (interrogation wavelength range). Visible and near infra-red transmission is required for photoacoustic illumination and for thermoelastic ultrasound generation.

2. Use of dual cladding fiber (multimode and single mode) instead of single mode only fiber. This modification is required to allow photoacoustic and phosphorescence light transmission.

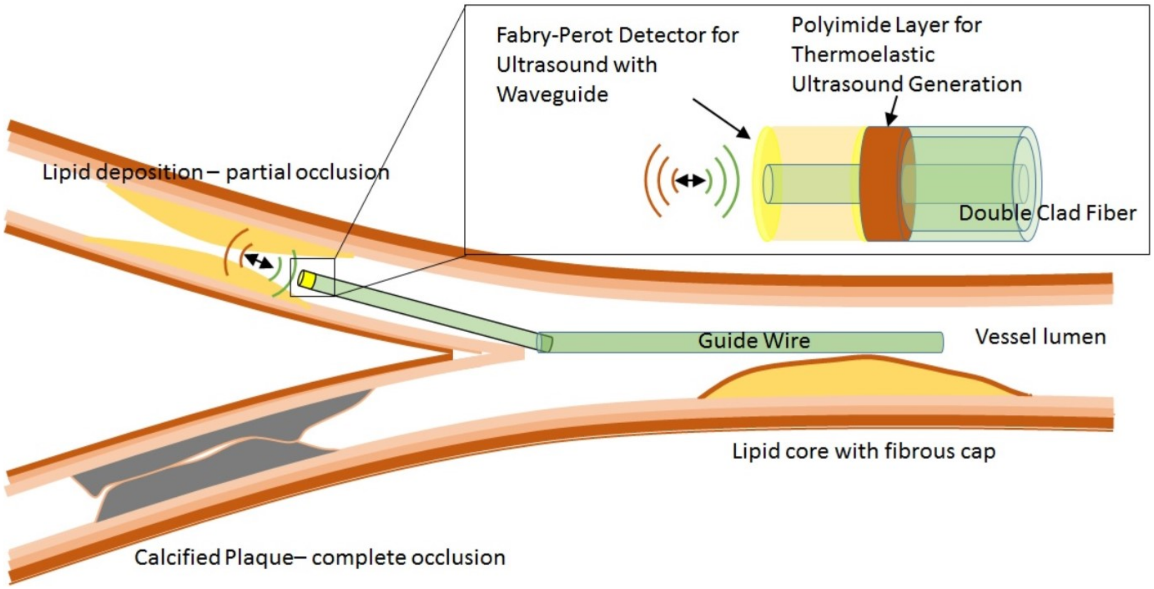

Figure 6.1: Vision for smart guide wire with embedded ultrasound cum photoacoustic probe to aid CTO intervention. The Double-clad fiber design allows for NIR interrogation of the FP sensor for ultrasound detection through the single-mode core, as well as illumination for photoacoustic excitation through the multi-mode core and thermoelastic ultrasound generation from the polyimide layer.

In addition to the above, the guidewire will need to be steerable. Standard guidewires have a bend in their proximal tip to allow steering the device and navigating to the anatomy of interest. The device will need to be suitably modified to allow for this. The plans for testing in tissue phantoms and animal models presented in this chapter are limited to performance evaluation of the sensor itself, leaving the design of housing and other mechanical constraints to future efforts.

6.2 Photoacoustic Sensing Demonstration

In order to verify the sensing capabilities and estimate the detection range of the sensor in tissue, the following experiment will be conducted. A tissue-mimicking phantom will be created using clear plastic/tygon tubing of small diameter (1 mm) within which blood or hemogobin solution will be circulated. this tubing will be placed within a reservor containing a scattering solution. The solution will be prepared such that the scattering coefficient and acoustic properties match that of tissue. Several recipes using substances such as milk and gelatin are available in literature for the creation of such phantoms to test photoacoustic sensors [78] [79] [80].

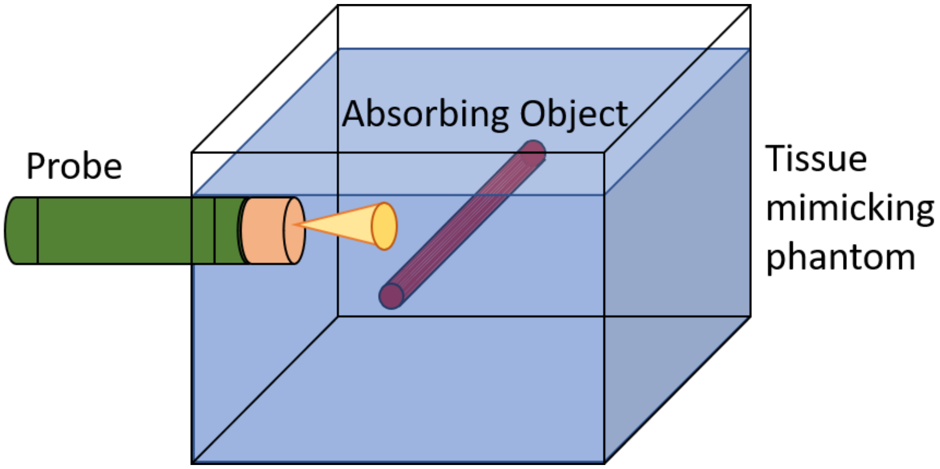

Figure 6.2: Tissue mimicking phantom setup to demonstrate photoacoustic sensing and estimate the range of detection

The device will then be placed within this reservoir and photoacoustic measurements taken at various distances to estimate the range of detection. For illumination, the fiber-bundle coupled output of a tunable pulsed laser (OPOTEK, Phocus system 660 – 950 nm), will be focused through a lens into the multimode core. The same CW

NIR laser described in earlier chapters will be used for the all-optical detection. From this experiment, it can be confirmed that the device is able to deliver sufficient illumination for photoacoustic excitation, and that the resulting photoacoustic wave can be reliably detected over the desirable distances(1-4 mm) in an anatomically accurate model.

6.3 Pre-clinical Testing

Having verified the performance of the probe in an in-vitro model, the next phase of the project envisaged is the pre-clinal testing of the device. For this, the guidewire developed can be tested in its ability to safely guide crossing a CTO lesion in a swine model.

6.3.1 CTO Characterization

The main goal would be to test the hypothesis that multi-wavelength photoacoustic sensor signals can be utilized to identify and distinguish the following three cases of the guidewire tip position:

1. Tip is in the true lumen: in this case the physician can continue crossing in the same direction.
2. Tip is in close proximity to the vessel wall :in this case, the guidewire needs to be redirected before continuing
3. Tip is approaching the distal cap of the CTO: This is the safe and intended exit point, and the physician can prepare to cross the occlusion completely.

This design is based on the hypothesis that the tissue in the occluded section is depleted of oxygen and therefore differs in its photoacoustic signature from oxygenated blood on either side, as well as from the vessel wall which is still perfused with oxygenate blood through the vaso vasorum.

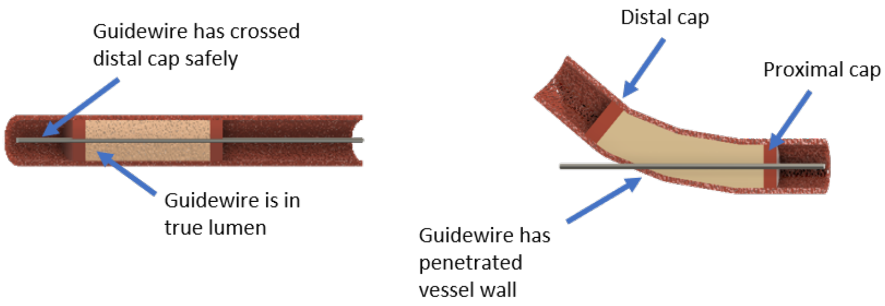

Figure 6.3: CTO sites prepared in hind limbs of a swine. Straight section (left) to study PA signatures from true lumen within occlusion, and true lumen beyond distal cap and site where the artery is bent (right) to study signals obtained while in the layers of the vessel wall

6.3.2 Porcine Model of CTO

There are works of literature that outline procedures to create CTO animal models for the proposed work[81][82][83]. The model described by Fefer et al. appears the most suitable. This procedure includes insertion of a collagen plug to a desired CTO site to block arterial flow. This model has been shown to recreate many features that have been recognized in human CTO maturation. These include an initial thrombotic occlusion, acute inflammatory response, calcium deposits, microvessels, and collagen-rich fibrous tissue.

A set of experiments will be designed to test the functionality of the sensing guidewire and the ability to correctly identify the tip position in one of the three cases above. Since the design of the sensing guidewire will still not include a tip bend that is essential for changing propagation direction while penetrating the solid lesion, the device would only be able to cross a CTO in a straight line. Therefore, some of the sites for inducing a CTO lesion in the animal models can be chosen along a straight artery segment to allow a straight-line crossing of the lesion from the entry point in the proximal cap to the exit at the distal cap. Other sites can be chosen along a bend in the artery such that a straight line from the entry point will lead to perforating the vessel wall. In both cases a centering balloon can be used before penetrating the proximal cap to assure that the entry point is positioned at the center of the lumen. By collecting the photoacoustic response to Hb and HbO2 at these locations, it is envisaged that the three locations mentioned above can be differentiated.

6.4 Conclusion

A novel design for all-optical fiber Fabry-Perot ultrasound detectors has been demonstrated. Employing a polymer waveguide to restrict diffraction losses and improve the Q-factor, this design allows high sensitivity detection of ultrasound with a fully flat, scalable design. The flat construction offers the opportunity to scale bandwidth for wider bandwidth detection. Further, this fabrication method is amenable to both single fiber and fiber-bundle devices. The high sensitivity and scalable bandwidth are significant for photoacoustic sensing, and open avenues in forward sensing at a size scale where piezoelectric devices are significantly less effective. This all-optical detection mechanism can be combined with simultaneous photoacoustic and optical-ultrasound excitation, enabling sensing using two different modalities. Such a device could be incorporated into either needle-based sensors to guide biopsies, or standard guidewires used in interventional cardiology for combined IVUS and photoacoustic sensing, thus creating a useful tool to address a range of clinical problems including interventions for CTO, which are an important and open clinical challenge. The high sensitivities demonstrated surpass the performance of standard piezoelectric transducers at this size scale, thus creating new opportunities to sense in a range of biological areas that were previously inaccessible.

Bibliography

[1] W. J. Gussenhoven, C. E. Essed, P. Frietman, F. Mastik, C. Lancée, C. Slager, P. Serruys, P. Gerritsen, H. Pieterman, and N. Bom. Intravascular echographic assessment of vessel wall characteristics: a correlation with histology. *The International Journal of Cardiac Imaging*, 4(2):105–116, Jun 1989.

[2] Carlo Di Mario, Stanley Madretsma, Robert J van Suylen, Richard A Wilson, Nicolaas Bom, Patrick W Serruys, Elma J Gussenhoven, Jos RTC Roelandt, Yin Zhong, L Wenguang, et al. Detection and characterization of vascular lesions by intravascular ultrasound: an in vitro study correlated with histology. *Journal of the American Society of Echocardiography*, 5(2):135–146, 1992.

[3] Natesa G Pandian, Andreas Kreis, and Thomas O'Donnell. Intravascular ultrasound estimation of arterial stenosis. *Journal of the American Society of Echocardiography*, 2(6):390–397, 1989.

[4] Steven E Nissen, John C Gurley, Cindy L Grines, David C Booth, Rick McClure, Martin Berk, Charles Fischer, and Anthony N DeMaria. Intravascular ultrasound assessment of lumen size and wall morphology in normal subjects and patients with coronary artery disease. *Circulation*, 84(3):1087–1099, 1991.

[5] Neal W White Jr and Paul G Yock. Intravascular ultrasound: catheter-based doppler and two-dimensional imaging. *Cardiology clinics*, 7(3):525–536, 1989.

[6] Krishnakutty Sudhir, Peter J. Fitzgerald, and Paul G. Yock M.D. Potential for tissue characterization of plaque and arterial wall using intravascular ultrasound. In Abund Ottokar Wist, editor, *Clinical Applications of Modern Imaging Technology*, volume 1894, pages 115 – 121. International Society for Optics and Photonics, SPIE, 1993.

[7] John McB Hodgson, Karan G Reddy, Randeep Suneja, Ravi N Nair, Edward J Lesnefsky, and Helen M Sheehan. Intracoronary ultrasound imaging: correlation of plaque morphology with angiography, clinical syndrome and procedural results in patients undergoing coronary angioplasty. *Journal of the American College of Cardiology*, 21(1):35–44, 1993.

[8] Bruce F Waller, Cass A Pinkerton, and JD Slack. Intravascular ultrasound: a histological study of vessels during life. the new'gold standard'for vascular imaging. *Circulation*, 85(6):2305–2310, 1992.

[9] N. G. Pandian. Intravascular and intracardiac ultrasound imaging. An old concept, now on the road to reality. *Circulation*, 80(4):1091–1094, 1989.

[10] Yukunori Korogi, Toshinori Hirai, and Mutasumasa Takahashi. Intravascular ultrasound imaging of peripheral arteries as an adjunct to balloon angioplasty and atherectomy. *CardioVascular and Interventional Radiology*, 19(1):1–9, Jan 1996.

[11] PAUL G. YOCK, PETER FITZGERALD, NEAL WHITE, DAVID T. LINKER, and BJOERN A.J. ANGELSEN. Intravascular ultrasound as a guiding modality for mechanical atherectomy and laser ablation. *Echocardiography*, 7(4):425–431, 1990.

[12] Junko Honye, Donald J Mahon, Ashit Jain, Christopher J White, Stephen R Ramee, James B Wallis, Amer Al-Zarka, and Jonathan M Tobis. Morphological effects of coronary balloon angioplasty in vivo assessed by intravascular ultrasound imaging. *Circulation*, 85(3):1012–1025, 1992.

[13] Paul G Yock and Peter J Fitzgerald. Intravascular ultrasound: state of the art and future directions. *The American journal of cardiology*, 81(7):27E–32E, 1998.

[14] Yun Zhou, Peter S McKinnis, and Neal E Fearnot. Mechanical scanning ultrasound transducer with micromotor, October 4 2016. US Patent 9,456,802.

[15] Peter NT Wells. Ultrasound imaging. *Physics in Medicine & Biology*, 51(13):R83, 2006.

[16] Michael Maschke. Device for implementing a cutting balloon intervention with ivus monitoring, February 7 2012. US Patent 8,109,951.

[17] Sorin Grunwald and Tat-Jin Teo. Adaptive cancellation of ring-down artifact in ivus imaging, July 3 2001. US Patent 6,254,543.

[18] Gastón A Rodriguez-Granillo, Nico Bruining, Eugene Mc Fadden, Jurgen MR Ligthart, Jiro Aoki, Evelyn Regar, Pim de Feyter, and Patrick W Serruys. Geometrical validation of intravascular ultrasound radiofrequency data analysis (virtual histology) acquired with a 30 mhz boston scientific corporation imaging catheter. *Catheterization and cardiovascular interventions*, 66(4):514–518, 2005.

[19] CT Lancee, N Bom, and J Roelandt. Future directions in intravascular ultrasound: From micro-motors to imaging guidewire systems. *Echocardiography*, 12(3):275–281, 1995.

[20] Masayuki Tanabe, Shangping Xie, Norio Tagawa, Tadashi Moriya, and Yuji Furukawa. Development of a mechanical scanning-type intravascular ultrasound system using a miniature ultrasound motor. *Japanese Journal of Applied Physics*, 46(7S):4805, 2007.

[21] M O'Donnell, M.J Eberle, D.N Stephens, J.L Litzza, K San Vicente, and B.M Shapo. Synthetic phased arrays for intraluminal imaging of coronary arteries. *IEEE Transactions on Ultrasonics, Ferroelectrics, and Frequency Control*, 44(3):714–721, 1997.

[22] Arash Taki, Holger Hetterich, Alireza Roodaki, SK Setarehdan, Gozde Unal, Johannes Rieber, Nassir Navab, and Andreas König. A new approach for improving coronary plaque component analysis based on intravascular ultrasound images. *Ultrasound in medicine & biology*, 36(8):1245–1258, 2010.

[23] Gokce Gurun, Coskun Tekes, Jaime Zahorian, Toby Xu, Sarp Satir, Mustafa Karaman, Jennifer Hasler, and F Levent Degertekin. Single-chip cmut-on-cmos front-end system for real-time volumetric ivus and ice imaging. *IEEE transactions on ultrasonics, ferroelectrics, and frequency control*, 61(2):239–250, 2014.

[24] Omer Oralkan, A Sanli Ergun, Jeremy A Johnson, Mustafa Karaman, Utkan Demirci, Kambiz Kaviani, Thomas H Lee, and Butrus T Khuri-Yakub. Capacitive micromachined ultrasonic transducers: Next-generation arrays for acoustic imaging? *IEEE transactions on ultrasonics, ferroelectrics, and frequency control*, 49(11):1596–1610, 2002.

[25] Douglas N Stephens, Uyen T Truong, Amin Nikoozadeh, Ömer Oralkan, Chi Hyung Seo, Jonathan Cannata, Aaron Dentinger, Kai Thomenius, Alan De La Rama, Tho Nguyen, et al. First in vivo use of a capacitive micromachined ultrasound transducer array–based imaging and ablation catheter. *Journal of Ultrasound in Medicine*, 31(2):247–256, 2012.

[26] Amin Nikoozadeh, David J Wygant, Der-Song Lin, Omer Oralkan, A Sanli Ergun, Douglas N Stephens, Kai E Thomenius, Aaron M Dentinger, Douglas Wildes, Gina Akopyan, et al. Forward-looking intracardiac ultrasound imaging using a 1-d cmut array integrated with custom front-end electronics. *IEEE transactions on ultrasonics, ferroelectrics, and frequency control*, 55(12):2651–2660, 2008.

[27] S Sethuraman, Salavat Aglyamov, J Amirian, R Smalling, and Stanislav Emelianov. Intravascular photoacoustic imaging to detect and differentiate atherosclerotic plaques. In *IEEE Ultrasonics Symposium, 2005.*, volume 1, pages 133–136. IEEE, 2005.

[28] Stanislav Emelianov, Bo Wang, Jimmy Su, Andrei Karpiouk, Evgeniya Yantsen, Konstantin Sokolov, James Amirian, Richard Smalling, and Shriram Sethuraman. Intravascular ultrasound and photoacoustic imaging. In *2008 30th Annual International Conference of the IEEE Engineering in Medicine and Biology Society*, pages 2–5. IEEE, 2008.

[29] Thomas J Allen and Paul C Beard. Photoacoustic characterisation of vascular tissue at nir wavelengths. In *Photons plus ultrasound: imaging and sensing 2009*, volume 7177, page 71770A. International Society for Optics and Photonics, 2009.

[30] TJ Allen, A Hall, A Dhillon, JS Owen, and PC Beard. Photoacoustic imaging of lipid rich plaques in human aorta. In *Photons Plus Ultrasound: Imaging and Sensing 2010*, volume 7564, page 75640C. International Society for Optics and Photonics, 2010.

[31] Bo Wang, Jimmy L Su, James Amirian, Silvio H Litovsky, Richard Smalling, and Stanislav Emelianov. Detection of lipid in atherosclerotic vessels using ultrasound-guided spectroscopic intravascular photoacoustic imaging. *Optics express*, 18(5):4889–4897, 2010.

[32] Iulia M Graf, Jimmy Su, Doug Yeager, James Amirian, Richard Smalling, and Stanislav Emelianov. Methodical study on plaque characterization using integrated vascular ultrasound, strain and spectroscopic photoacoustic imaging. In *Photons Plus Ultrasound: Imaging and Sensing 2011*, volume 7899, page 789902. International Society for Optics and Photonics, 2011.

[33] Bo Wang, Andrei Karpiouk, Doug Yeager, James Amirian, Silvio Litovsky, Richard Smalling, and Stanislav Emelianov. Intravascular photoacoustic imaging of lipid in atherosclerotic plaques in the presence of luminal blood. *Optics letters*, 37(7):1244–1246, 2012.

[34] Krista Jansen, Gijs van Soest, and Antonius FW van der Steen. Intravascular photoacoustic imaging: a new tool for vulnerable plaque identification. *Ultrasound in medicine & biology*, 40(6):1037–1048, 2014.

[35] Georg Wissmeyer, Miguel A Pleitez, Amir Rosenthal, and Vasilis Ntziachristos. Looking at sound : optoacoustics with all-optical ultrasound detection. *Light: Science & Applications*, 2018.

[36] Shai Ashkenazi, Chung-Yen Chao, L Jay Guo, and Matthew O'donnell. Ultrasound detection using polymer microring optical resonator. *Applied physics letters*, 85(22):5418–5420, 2004.

[37] Chung-Yen Chao, Shai Ashkenazi, Sheng-Wen Huang, Matthew O'Donnell, and L Jay Guo. High-frequency ultrasound sensors using polymer microring resonators. *ieee transactions on ultrasonics, ferroelectrics, and frequency control*, 54(5):957–965, 2007.

[38] Sheng-Wen Huang, Sung-Liang Chen, Tao Ling, Adam Maxwell, Matthew O'Donnell, L Jay Guo, and Shai Ashkenazi. Low-noise wideband ultrasound detection using polymer microring resonators. *Applied physics letters*, 92(19):193509, 2008.

[39] Adam Maxwell, Sheng-Wen Huang, Tao Ling, Jin-Sung Kim, Shai Ashkenazi, and L Jay Guo. Polymer microring resonators for high-frequency ultrasound detection and imaging. *IEEE Journal of Selected Topics in Quantum Electronics*, 14(1):191–197, 2008.

[40] Cheng Zhang, Sung-Liang Chen, Tao Ling, and L Jay Guo. Review of imprinted polymer microrings as ultrasound detectors: Design, fabrication, and characterization. *IEEE Sensors Journal*, 15(6):3241–3248, 2015.

[41] Bao-Yu Hsieh, Sung-Liang Chen, Tao Ling, L Jay Guo, and Pai-Chi Li. All-optical scanhead for ultrasound and photoacoustic dual-modality imaging. *Optics Express*, 20(2):1588–1596, 2012.

[42] G Meltz, W_W Morey, and WH Glenn. Formation of bragg gratings in optical fibers by a transverse holographic method. *Optics letters*, 14(15):823–825, 1989.

[43] Kenneth O Hill and Gerald Meltz. Fiber bragg grating technology fundamentals and overview. *Journal of lightwave technology*, 15(8):1263–1276, 1997.

[44] Amir Rosenthal, Daniel Razansky, and Vasilis Ntziachristos. High-sensitivity compact ultrasonic detector based on a pi-phase-shifted fiber bragg grating. *Optics letters*, 36(10):1833–1835, 2011.

[45] Georg Wissmeyer, Dominik Soliman, Rami Shnaiderman, Amir Rosenthal, and Vasilis Ntziachristos. All-optical optoacoustic microscope based on wideband pulse interferometry. *Optics letters*, 41(9):1953–1956, 2016.

[46] Amir Rosenthal, Stephan Kellnberger, Dmitry Bozhko, Andrei Chekkoury, Murad Omar, Daniel Razansky, and Vasilis Ntziachristos. Sensitive interferometric detection of ultrasound for minimally invasive clinical imaging applications. *Laser & Photonics Reviews*, 8(3):450–457, 2014.

[47] Byeong Ha Lee, Young Ho Kim, Kwan Seob Park, Joo Beom Eom, Myoung Jin Kim, Byung Sup Rho, and Hae Young Choi. Interferometric fiber optic sensors. *sensors*, 12(3):2467–2486, 2012.

[48] Zengling Ran, Yunjiang Rao, Jian Zhang, Zhiwei Liu, and Bing Xu. A miniature fiber-optic refractive-index sensor based on laser-machined fabry–perot interferometer tip. *Journal of Lightwave Technology*, 27(23):5426–5429, 2009.

[49] Tao Wei, Yukun Han, Hai-Lung Tsai, and Hai Xiao. Miniaturized fiber inline fabry-perot interferometer fabricated with a femtosecond laser. *Optics letters*, 33(6):536–538, 2008.

[50] VR Machavaram, RA Badcock, and GF Fernando. Fabrication of intrinsic fibre fabry–perot sensors in silica fibres using hydrofluoric acid etching. *Sensors and Actuators A: Physical*, 138(1):248–260, 2007.

[51] Yun-Jiang Rao. Recent progress in fiber-optic extrinsic fabry–perot interferometric sensors. *Optical Fiber Technology*, 12(3):227–237, 2006.

[52] David Hunger, Tilo Steinmetz, Yves Colombe, Christian Deutsch, Theodor W Hänsch, and Jakob Reichel. A fiber fabry–perot cavity with high finesse. *New Journal of Physics*, 12(6):065038, 2010.

[53] JS Sirkis, DD Brennan, MA Putman, TA Berkoff, AD Kersey, and EJ Friebele. In-line fiber etalon for strain measurement. *Optics letters*, 18(22):1973–1975, 1993.

[54] James A. Guggenheim, Jing Li, Thomas J. Allen, Richard J. Colchester, Sacha Noimark, Olumide Ogunlade, Ivan P. Parkin, Ioannis Papakonstantinou, Adrien E. Desjardins, Edward Z. Zhang, and Paul C. Beard. Ultrasensitive plano-concave optical microresonators for ultrasound sensing. *Nature Photonics*, 11:714–719, Nov 2017.

[55] S Aziz and DR Ramsdale. Chronic total occlusions—a stiff challenge requiring a major breakthrough: is there light at the end of the tunnel? *Heart*, 91(suppl 3):iii42–iii48, 2005.

[56] Pinak B Shah. Management of coronary chronic total occlusion. *Circulation*, 123(16):1780–1784, 2011.

[57] Abhiram Prasad, Charanjit S Rihal, Ryan J Lennon, Heather J Wiste, Mandeep Singh, and David R Holmes. Trends in outcomes after percutaneous coronary intervention for chronic total occlusions: a 25-year experience from the mayo clinic. *Journal of the American College of Cardiology*, 49(15):1611–1618, 2007.

[58] Donald S Baim, Greg Braden, Richard Heuser, Jeffrey J Popma, Donald E Cutlip, Joseph M Massaro, Sachin Marulkar, Linda J Arvay, and Richard E Kuntz. Utility of the safe-cross–guided radiofrequency total occlusion crossing system in chronic coronary total occlusions (results from the guided radio frequency energy ablation of total occlusions registry study). *The American journal of cardiology*, 94(7):853–858, 2004.

[59] Mauro Carlino, Azeem Latib, Cosmo Godino, John Cosgrave, and Antonio Colombo. Cto recanalization by intraocclusion injection of contrast: the microchannel technique. *Catheterization and Cardiovascular Interventions*, 71(1):20–26, 2008.

[60] Aytekin Oto, Ila Sethi, Gregory Karczmar, Roger McNichols, Marko K Ivancevic, Walter M Stadler, Sydeaka Watson, and Scott Eggener. Mr imaging–guided focal laser ablation for prostate cancer: phase i trial. *Radiology*, 267(3):932–940, 2013.

[61] Marites P Melancon, Wei Lu, Meng Zhong, Min Zhou, Gan Liang, Andrew M Elliott, John D Hazle, Jeffrey N Myers, Chun Li, and R Jason Stafford. Targeted multifunctional gold-based nanoshells for magnetic resonance-guided laser ablation of head and neck cancer. *Biomaterials*, 32(30):7600–7608, 2011.

[62] Jing Li, Alaric Taylor, Ioannis Papakonstantinou, Edward Zhang, and Paul Beard. Highly sensitive optical microresonator sensors for photoacoustic imaging. In *Photons Plus Ultrasound: Imaging and Sensing 2014*, volume 8943, page 89430C. International Society for Optics and Photonics, 2014.

[63] Herbert B Callen and Theodore A Welton. Irreversibility and generalized noise. *Physical Review*, 83(1):34, 1951.

[64] M. A. Tadayon, M. Baylor, and S. Ashkenazi. Polymer waveguide fabry-perot resonator for high-frequency ultrasound detection. *IEEE Transactions on Ultrasonics, Ferroelectrics, and Frequency Control*, 61(12):2132–2138, Dec 2014.

[65] Supriya V Thathachary and Shai Ashkenazi. Performance improvement of an all-optical fabry perot ultrasound detector. In *Optical Fibers and Sensors for Medical Diagnostics and Treatment Applications XVII*, volume 10058, page 100580M. International Society for Optics and Photonics, 2017.

[66] Supriya V Thathachary and Shai Ashkenazi. Toward a highly sensitive polymer waveguide fiber Fabry–Pérot ultrasound detector. *Journal of Biomedical Optics*, 23(10):1 – 12, 2018.

[67] Theodor Tamir and Shuzhang Zhang. Modal transmission-line theory of multilayered grating structures. *Journal of lightwave technology*, 14(5):914–927, 1996.

[68] Barry R. Masters and Lihong V. Wang. Photoacoustic Imaging and Spectroscopy. *Journal of Biomedical Optics*, 15(5):1 – 2, 2010.

[69] Edward Z. Zhang and Paul C. Beard. A miniature all-optical photoacoustic imaging probe. In Alexander A. Oraevsky and Lihong V. Wang, editors, *Photons Plus Ultrasound: Imaging and Sensing 2011*, volume 7899, pages 291 – 296. International Society for Optics and Photonics, SPIE, 2011.

[70] Liang-Yin Chen, Wan-Shao Tsai, Wen-Hao Hsu, Kuan-Yu Chen, and Way-Seen Wang. Fabrication and characterization of benzocyclobutene optical waveguides by uv pulsed-laser illumination. *Quantum Electronics, IEEE Journal of*, 43:303 – 310, 05 2007.

[71] T Buma, M Spisar, and M O'donnell. High-frequency ultrasound array element using thermoelastic expansion in an elastomeric film. *Applied Physics Letters*, 79(4):548–550, 2001.

[72] Takashi Buma, Monica Spisar, and Matthew O'Donnell. A high-frequency, 2-d array element using thermoelastic expansion in pdms. *IEEE transactions on ultrasonics, ferroelectrics, and frequency control*, 50(9):1161–1176, 2003.

[73] Yang Hou, Jin-Sung Kim, Shai Ashkenazi, Matthew O'Donnell, and L Jay Guo. Optical generation of high frequency ultrasound using two-dimensional gold nanostructure. *Applied physics letters*, 89(9):093901, 2006.

[74] Richard M White. Generation of elastic waves by transient surface heating. *Journal of Applied Physics*, 34(12):3559–3567, 1963.

[75] AM Aindow, RJ Dewhurst, DA Hutchins, and SB Palmer. Laser-generated ultrasonic pulses at free metal surfaces. *The Journal of the Acoustical Society of America*, 69(2):449–455, 1981.

[76] X Wang and X Xu. Thermoelastic wave induced by pulsed laser heating. *Applied Physics A*, 73(1):107–114, 2001.

[77] Hyoung Won Baac, Jong G Ok, Hui Joon Park, Tao Ling, Sung-Liang Chen, A John Hart, and L Jay Guo. Carbon nanotube composite optoacoustic transmitters for strong and high frequency ultrasound generation. *Applied physics letters*, 97(23):234104, 2010.

[78] Teng-Yuan Liu Shu-Wei Huang and Huihua Kenny Chiang. Synthetic aperture photoacoustic imaging on small vessel phantom study. *Journal of Medical and Biological Engineering*, 25(4):179–183, 2005.

[79] Gerhard Mitic, Jochen Kölzer, Johann Otto, Erich Plies, Gerald Sölkner, and Wolfgang Zinth. Time-gated transillumination of biological tissues and tissuelike phantoms. *Applied optics*, 33(28):6699–6710, 1994.

[80] Suhyun Park, Andrei B Karpiouk, Salavat R Aglyamov, and Stanislav Y Emelianov. Adaptive beamforming for photoacoustic imaging. *Optics letters*, 33(12):1291–1293, 2008.

[81] Paul Fefer, Normand Robert, Beiping Qiang, Garry Liu, Nigel Munce, Kevan Anderson, Azriel B Osherov, Michelle Ladouceur-Wodzak, Xiuling Qi, Alexander Dick, et al. Characterisation of a novel porcine coronary artery cto model. *EuroIntervention: journal of EuroPCR in collaboration with the Working Group on Interventional Cardiology of the European Society of Cardiology*, 7(12):1444–1452, 2012.

[82] Michael Frie, Michael Jorgenson, Mark E Smith, and Michael Conforti. A reproducible model of a chronic partial occlusion: A cylindrical bone marrow allograft implanted in the porcine coronary and peripheral vasculature. *Journal of Medical Devices*, 9(2):020909, 2015.

[83] Usaid K Allahwala, James Weaver, and Ravinay Bhindi. Animal chronic total occlusion models: A review of the current literature and future goals. *Thrombosis research*, 177:83–90, 2019.